IMPROVEMENT OF THE PERFORMANCE FOR PEROVSKITE SOLAR CELL

LI YUN

PhD

The Hong Kong Polytechnic University

2020

The Hong Kong Polytechnic University

Department of Mechanical Engineering

Improvement of the Performance for Perovskite Solar Cell

LI YUN

A Thesis Submitted in Partial Fulfillment of the Requirements
for the Degree of Doctor of Philosophy

June 2019

CERTIFICATE OF ORIGINALITY

I hereby declare that this thesis is my own work and that, to the best of my knowledge and belief, it reproduces no material previously published or written, nor material that has been accepted for the award of any other degree or diploma, except where due acknowledgement has been made in the text.

________________(signature)

___Li Yun________(Name of student)

Abstract

Being a low-cost and high-performance photovoltaic device, the hybrid organic–inorganic halide perovskite solar cell (PSC) has attracted extensive attention in the past few years. Significant research progress on PSC is mainly attributed to the properties of the perovskite material, including long-range carrier diffusion length (>1 μm), broad-wavelength light absorption (up to a wavelength of 800 nm), high charge carrier mobility (25 cm2V-1s-1) and adjustable band gap. There are two different fabricated device architectures, planar heterojunction and mesostructured PSC. Optimizing the quality of the perovskite film and the device configuration is important to improve the PSC performance. Improving film surface coverage and grain size in the film is a cost-effective way for energy harvesting and should be of prime importance. On the other hand, enhancing the charge transport property of the PSC is also a vital aspect that allows the photogenerated electrons to be transported efficiently before recombining with the separated holes.

In this study, the methods of developing PSC, characterizing the properties of the developed PSC, and various novel means for achieving high-performance PSC have been investigated. First, an efficient and simple approach has been investigated for using a combination of Dimethyl Sulphoxide (DMSO) to increase crystal size and hydrochloric acid (HCl) to further retard crystallization rate. The combined effect is to improve uniformity and crystallinity of the perovskite film. With this synergistic approach, superior quality perovskite film free from pinholes and with large uniform perovskite crystals over one micron has been obtained. The fabricated device has reached power conversion efficiency (PCE) of 17.8%, providing a 10%-11% improvement in PCE for both the best as well as the average performance. In addition,

the incorporation of chloride using HCl formulation has demonstrated to have better stability against degradation from moisture, strong solar irradiation, and high temperature, which is an important finding as stability is one of the key limitations for PSC.

Second, to further improve the quality of the perovskite layer and the charge transport property, home-made, well-controlled, pristine graphene nanofibers were introduced into the perovskite layer of PSC. The introduction of graphene nanofibers into the perovskite layer led to a dramatic increase in the grain size of the perovskite layer to over 2 m, due to improved nucleation and crystallization on the nanofiber surface, which led to much higher FF and Jsc values. Also, the significant increases in Jsc and Voc are attributed to the improved charge-transport properties of the graphene nanofibers with superb charge conductivity introduced into the perovskite layer. This is confirmed independently by the charge transport time using Intensity Modulated Photocurrent Spectroscopy. Under optimized conditions, the device PCE increased from 17.51% without graphene to 19.83% with graphene nanofibers, representing a 13% increase.

Third, a method for engineering large, uniform perovskite crystals has been studied. A thin structured electrospun TiO2 nanofiber scaffold has been applied to the dense TiO2 layer. The structured scaffold facilitates nucleation of the perovskite crystals from the nanofibers, especially at the intersections of nanofibers. By orienting the fibers forming polyhedrons and controlling the fiber packing density with uniform pore openings, large uniform crystals with high crystallinity that has good light absorption can be obtained. Further, graphene sheets in roll-up form, to eliminate adverse edge effect, were inserted in the TiO2 nanofibers in a convenient, simple way to enhance charge conductivity of the semiconductor nanofibers. Photogenerated electrons once generated in the perovskite crystals can travel to the TiO2 nanofibers and get injected into the graphene core. Subsequently, they are being transported to the electrode reducing electron-hole recombination thereby improving the current density of the PSC. Crystallizing perovskite in the TiO2 scaffold also eliminates unreacted PbI2 in a two-step crystallization process as compared to the PSC without the scaffold. The optimized PSC device exhibited PCE of 19.30%, which is 11% higher than the device without the nanofiber scaffold with PCE of 17.46%.

Fourth, we have developed an efficient and simple method by insertion of an ultrathin graphene nanofibers layer between the TiO2 dense layer and the perovskite layer to reduce the interfacial resistance. The concentration of graphene and the thickness of the graphene nanofiber layer has been optimized. As a result of the improvement of the electron transport at the perovskite-dense layer interface, both the best and average solar cells fabricated reveal 5%-8% increase in PCE as compared to the PSC without the interface layer. The best PCE of the fabricated heterojunction solar cell has reached 18.62%.

The results from the four different thrust areas in the present study highlight the significance of improving crystallinity, size and uniformity of crystals in the perovskite film. This was achieved by DMSO intercalating with the organic component, methylammonium iodide (MAI), in a two-step procedure in forming the perovskite, and nucleation and crystallization with the graphene nanofibers and the engineered TiO2 scaffold. The results also highlight the importance of efficient transport of photogenerated electrons reducing recombination by traps at crystal boundaries. Finally, the results also highlight the reduction of interfacial resistance to charge transport and the dense layer/perovskite layer was chosen as a demonstration.

Publications Arising from the Thesis

Journals

1. Yun Li, Kin Shing Kenneth Lo, Wallace Woon-Fong Leung. Conditioning lead iodide with dimethylsulfoxide and hydrochloric acid to control crystal growth improving performance of perovskite solar cell. *Solar Energy*, 157 (2017) 328-334.
2. Yun Li and Wallace Woon-Fong Leung. Introduction of Graphene Nanofibers into the Perovskite Layer of Perovskite Solar Cells. *ChemSusChem*, 11 (2018) 2921-2929.

Acknowledgements

Firstly, I would like to express my sincere gratitude to my supervisor, Prof. Wallace Woon-Fong Leung, for his active encouragement and academic support throughout my Ph.D. student study period. His critical instructions and invaluable guidance facilitated my success in my Ph.D. research. None of these would have been possible without his guidance.

I would also like to thank my colleagues, including Mr. Kin Shing Kenneth Lo, Mr. Qiangqiang Sun, Ms. Eva Mak, Dr. Chun Pei, Dr. Kanjwal, Muzafar Ahmad for their useful advice, kind assistance, moral encouragements throughout my research study, especially during difficult time.

Besides, I would like to thank the technicians in the Mechanical Engineering Laboratory, EIE laboratory belongs to Prof. Li Gang' team, especially Dr. Ren Zhiwei and Dr. Annie Ng in their team has supported and assisted me a lot during the past few years.

Last but not the least, I also have to show my special appreciation to my dear parents and elder sister, for their endless love and support. They always support me unconditionally no matter what choices I have made.

Table of Contents

LIST OF FIGURES

LIST OF TABLES

Chapter 1

Introduction

Increasing energy demands and concerns about global warming drive the exploration/development of clean, inexpensive and renewable energy sources (such as solar energy, geothermal energy, wind energy, biomass energy, tidal energy), especially for the past 10 years. Solar energy is a good choice for clean energy as the resource is sufficient for our use. Solar cells or photovoltaics can convert directly solar energy into electricity. This has attracted a great deal of attention in the past decades. However, compared with conventional power generation, the cost of the well commercialized silicon-based solar cells is too high. Organic photovoltaic cells (OPVs), dye sensitized solar cells (DSSCs)and quantum dot solar cells (QDSCs), have attracted significant attention as low-cost alternatives to conventional silicon-based solar cells. Recently, hybrid organometal halide perovskites, which were initially employed in DSSCs as light absorbers, have gradually become one of the most important active materials for all-solid-state solar cells (which can be named as perovskite solar cells) [1]. Being a low-cost and high-performance photovoltaic device, the hybrid organic–inorganic halide perovskite solar cell has attracted extensive attention [2-5]. To-date the highest efficiency for PSC has already reached 23.3% [6]. Although magnificent progress has been made for PSC, there are still many issues and barriers have not been fully and well investigated which can affect the improvement of the performance of the PSC. Therefore, improving the techniques for fabricating the PSC to enhance the performance of the devices is imperative. The introduction of the background and a review of the relevant literatures will be provided in this chapter.

1.1 Solar energy

The Earth receives 174 petawatts (PW) of incoming solar radiation (insolation) at the upper atmosphere. Approximately 30% is reflected back to space while the rest is absorbed by clouds, oceans and land masses, this can be shown in Figure 1.1. The spectrum of solar light at the Earth's surface is mostly spread across the visible and near-infrared ranges with a small part in the near-ultraviolet.

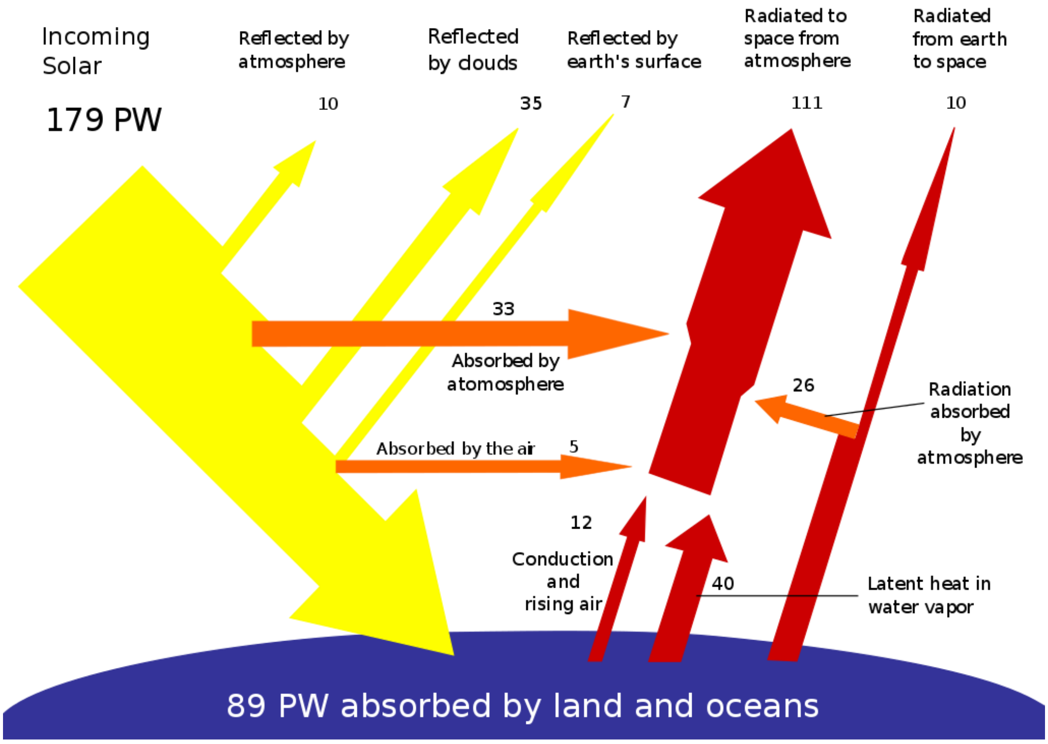

Figure 1.1. Illustration of the breakdown of incoming solar energy.

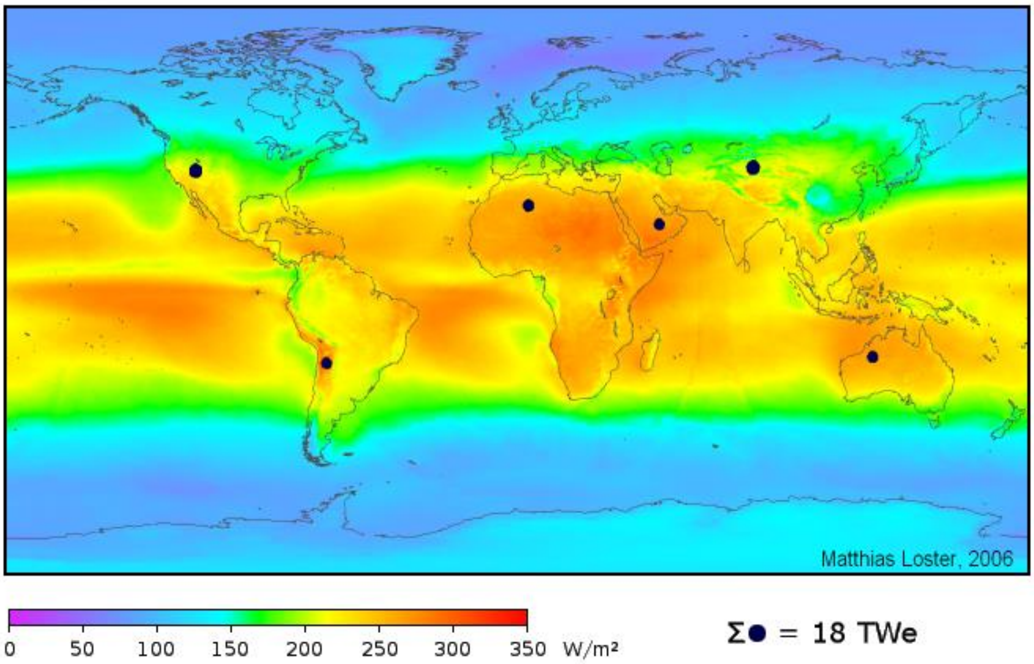

Frigure 1.2.   Illustration of solar land area.

From Figure 1.2 we can see that geography affects solar energy potential because areas that are closer to the equator have a greater amount of solar radiation. However, the use of photovoltaics that can follow the position of the sun can significantly increase the solar energy potential in areas that are farther from the equator. Earth's average solar power is 120,000TW, while the current average global power consumption is only approximately 18TW. As a result, solar radiation is a viable energy source to cover most of the global energy demand.

1.2 Solar Cell

1.2.1 Background

A solar cell, or photovoltaic cell, is an electrical device that converts the energy of light directly into electricity by the photovoltaic effect. In 1839, Alexandre-Edmond Becquerel first observed the photovoltaic (PV) effect [7]. Earlier solar cells are mainly thin silicon wafers. With the development of the solar cell, the modern photovoltaic technology is based on the principle of electron hole creation in each cell composed of two different layers (p-type and n-type materials) of a semiconductor material [8]. Various types of materials are applied to fabricate the solar cells, on the basis of these materials, the solar cells can be categorized into different classes as shown in Figure 1.3. Figure 1.4 shows the gradual development of solar cells fabricated from different materials and their best efficiencies.

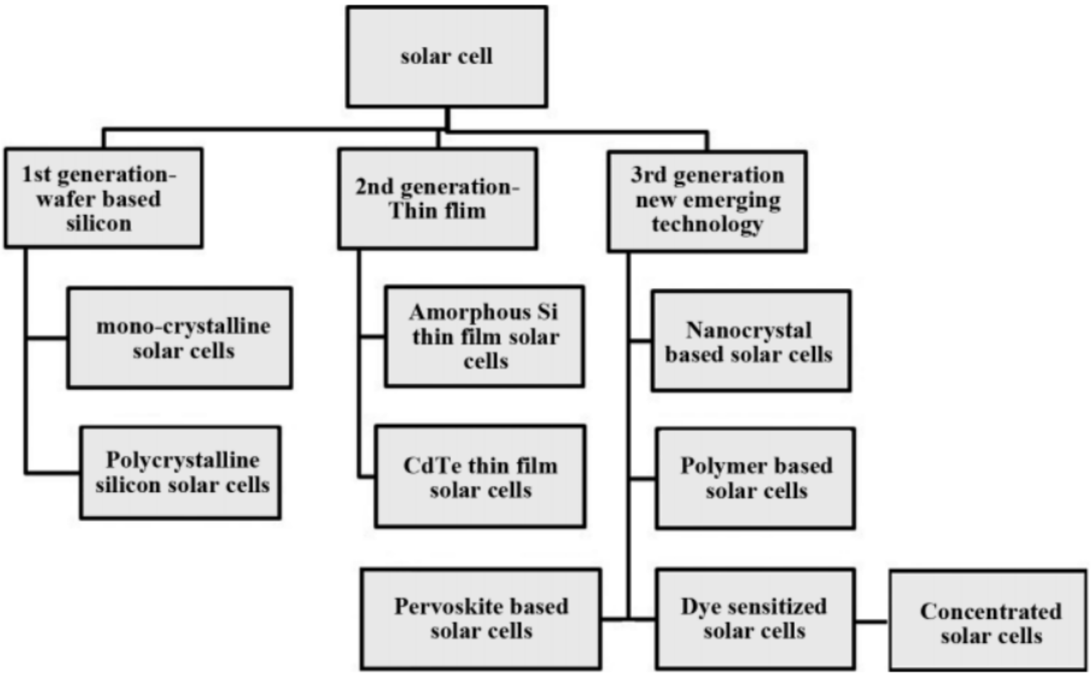

Figure 1.3. The classification of the solar cells [9-10].

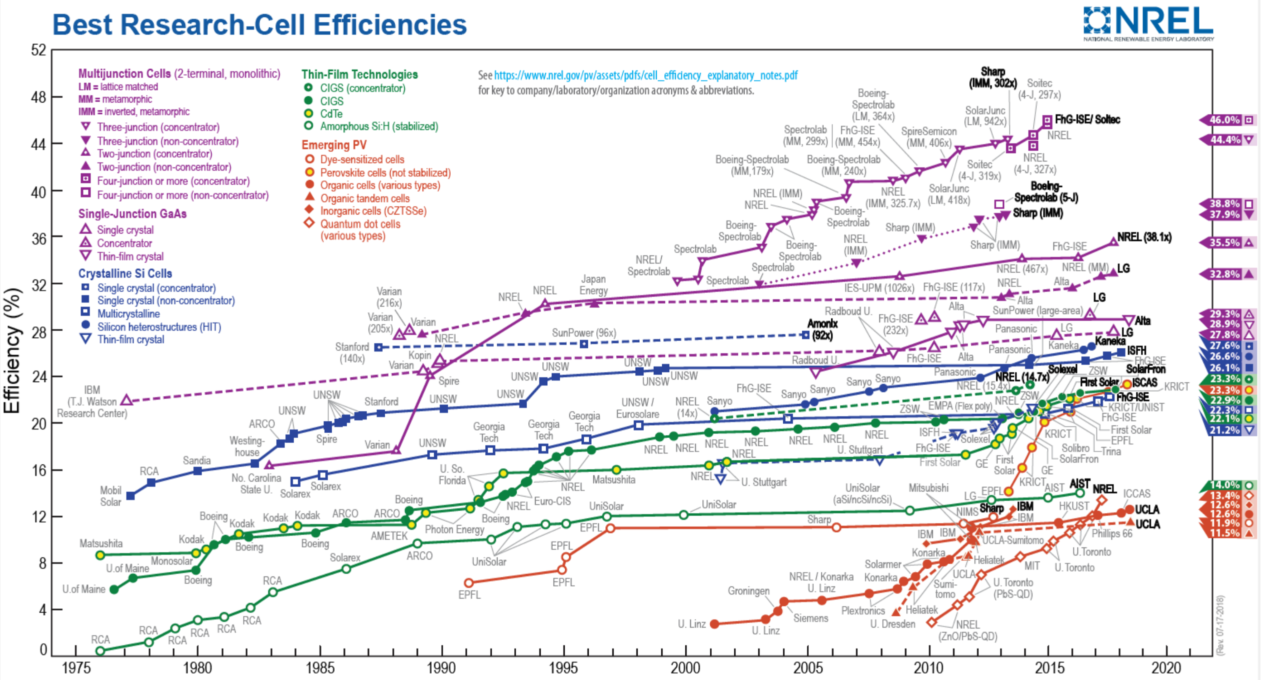

Figure 1.4. Best cell efficiency for different materials of solar cell [11].

1.2.2 Working principles of solar cells

A solar cell is basically a p-n junction diode. It utilizes photovoltaic effect to convert light energy into electrical energy. When a configuration consisting of both n-type and p-type semiconductors, the charge separation can be occurred due to bending of the bands in the depletion layer, the schematic diagram is shown in Figure 1.5. When light reaches the p-n junction, as shown in Figure 1.5, the light photons can easily enter in the junction, through very thin p-type layer. The light energy, in the form of photons, supplies sufficient energy to the junction to create a number of electron-hole pairs. The incident light breaks the thermal equilibrium condition of the junction. The free electrons in the depletion region can quickly come to the n-type side of the junction. Similarly, the holes in the depletion can quickly come to the p-type side of the junction. Once, the newly created free electrons come to the n-type side, cannot further cross the junction because of barrier potential of the junction.

Similarly, the newly created holes once come to the p-type side cannot further cross the junction became of same barrier potential of the junction. As the concentration of electrons becomes higher in one side, i.e. n-type side of the junction and concentration of holes becomes more in another side, i.e. the p-type side of the junction, the p-n junction will behave like a small battery cell. A voltage is set up which is known as photo voltage. If we connect a small load across the junction, there will be a tiny current flowing through it.

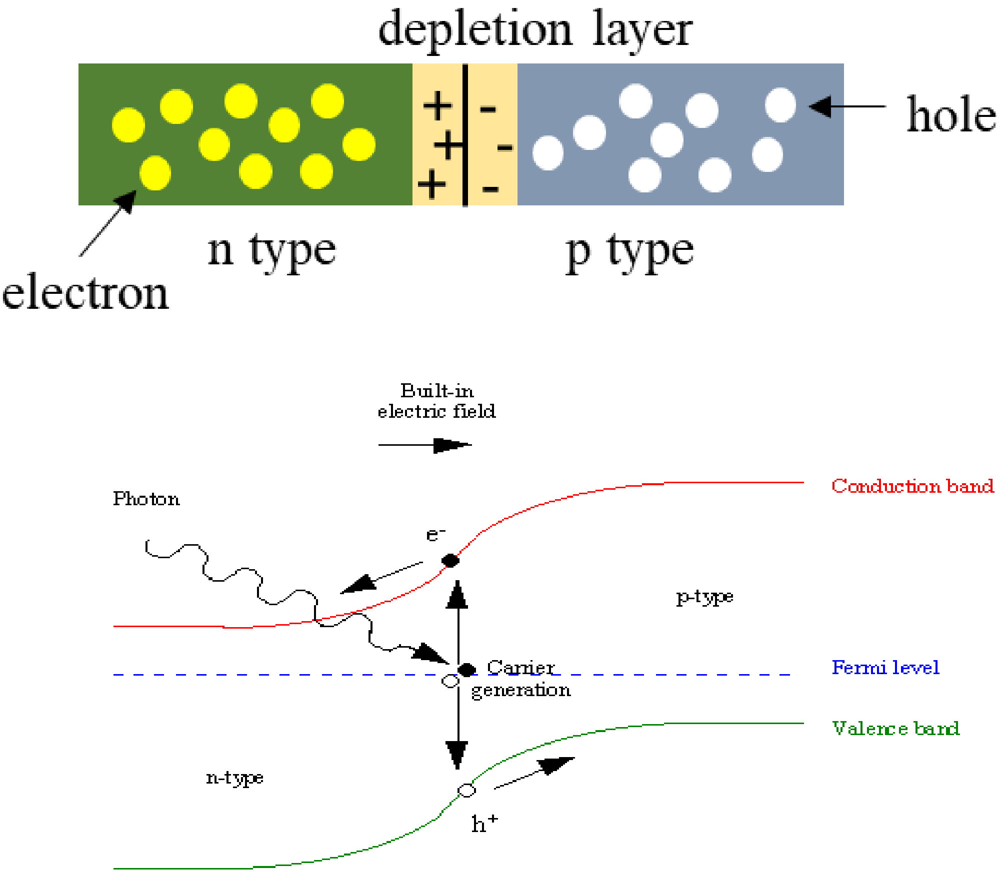

Figure 1.5. Schematic diagram p-n junction solar cell.

1.3 Silicon-based solar cells

The silicon-based solar cell can be divided into three types: monocrystalline silicon (c-Si), polycrystalline silicon (poly-Si) and amorphous silicon (a-Si). Crystalline silicon solar cells are the dominate type in the solar-cell market, with up to 93% market share [12]. The theoretical PCE limit is 28% for monocrystalline solar cells, the realized best efficiencies of research have reached 26.6%. However, these large single crystal productions require precise processing which is expensive and multi process. Polycrystalline silicon is generally composed of a number of different crystals, coupled to one another in a single cell, the best PCE is 22.9%. The processing of polycrystalline Si solar cells is more economical compared with monocrystalline solar cells, but the efficiency is lower than that of monocrystalline solar cells. Amorphous silicon is the non-crystalline form of silicon. It has a high absorption capacity and can therefore be used in solar cells with very small layer thicknesses (usually about a factor of 100 smaller than in crystalline silicon), saving on material costs. The structure of a-Si solar cell is shown in Figure 1.6. However, this PCE of this type of solar cell (the best PCE is 14%) is still lower than that of monocrystalline solar cells. The low efficiency rate is partly due to the Staebler-Wronski effect, which manifests itself in the first hours when the panels are exposed to sunlight, and results in a decrease in the energy. Despite its lower performance as compared to c-Si solar cells, amorphous silicon solar cells can be deposited at very low temperatures and on various structures, not only on glass but also plastic. Due to their simplified and lower cost production, a-Si solar cells have mostly been used for electronic devices with very little power requirements such as watches and pocket calculators.

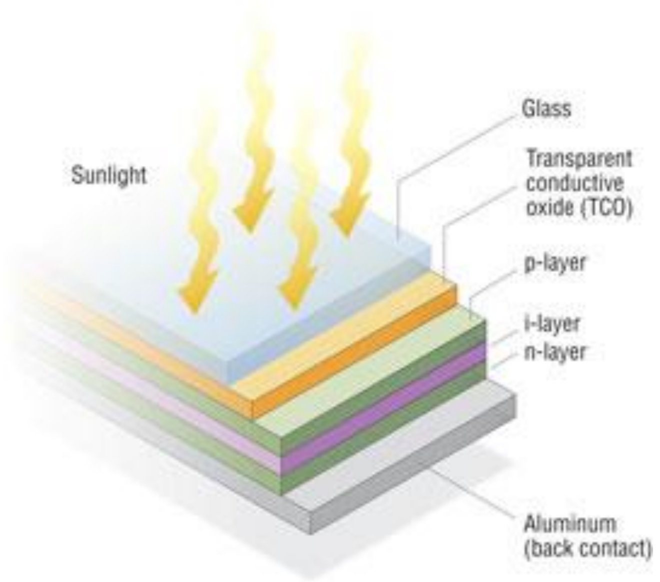

Figure 1.6. Schematic structure for a-Si solar cells [13].

1.4 Cadmium Telluride (CdTe) and Copper Indium Gallium Di-Selenide (CIGS) Thin Film Solar Cells

1.4.1 CdTe solar cells

Due to the near-ideal bandgap of ∼1.5 eV and high optical absorption coefficients, CdTe was recognized as a promising thin-film solar cell material back in 1950s [14]. As shown in Figure 1.7, CdTe solar cells can be fabricated in superstrate or substrate configurations. Cadmium sulfide (CdS) is usually used to combine with CdTe to produce a sandwiched p-n junction solar cell. Fabrication of efficient cells required certain postdeposition process steps that had to be applied to the already deposited CdS/CdTe film stacks [15]. The best efficiency of this type of solar cell is 21.5%.

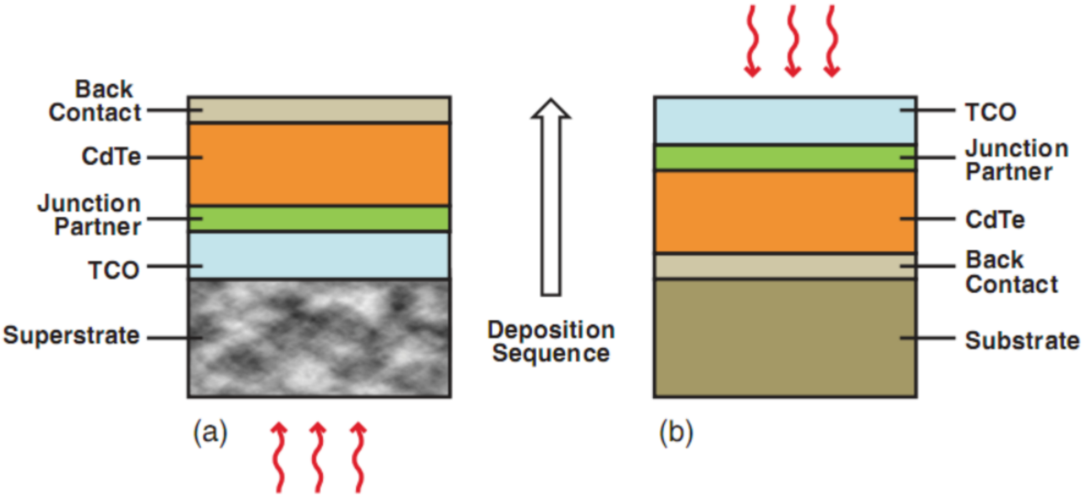

Figure 1.7. CdTe solar cell configurations: (a) superstrate and (b) substrate [16].

1.4.2 CIGS solar cells

CIGS is a tetrahedrally bonded semiconductor with a chalcopyrite crystal structure. Through adjust the Se/S and In/Ga ratios, the bandgap of CIGS can be tuned between 1.04 eV and 2.4 eV. A schematic diagram of a CIGS based solar cell having a structure of substrate/Mo/p-CIGS/n-CdS/intrinsic ZnO/ZnO:Al/ARC/metal-grid is shown in Figure 1.8 [17]. For high efficiency solar cells, the sputtering technique is used for depositing molybdenum (Mo) and ZnO. Vacuum and non-vacuum (chemical bath deposition, CBD) process methods are used for the deposition of the CIGS absorber layer and CdS window layer respectively. The best performance of such kind of solar cell is 22.9%.

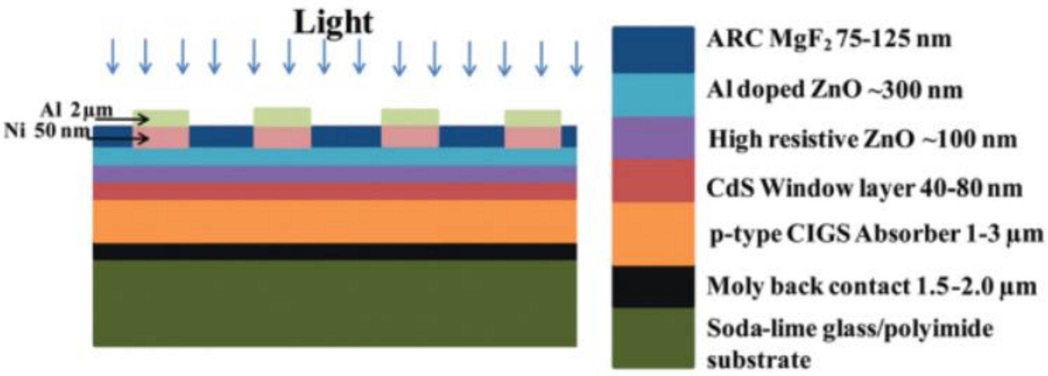

Figure 1.8. Schematic cross-section of CIGS based thin-film solar cells.

1.5 Dye-sensitized solar cells (DSSC)

The basic structure of a typical DSSC is composed of a sensitized mesoporous wide band-gap semiconductor, i.e., the sensitized photoanode, a counter electrode and an electrolyte [18-20]. The photoanode is the key component in DSSC, which captures the photons and transport them to the substrate. There are many different wide band-gap semiconductors can be used in the photoanode system, such as TiO_2, ZnO, and SnO_2. Among these, TiO_2 still shows the highest performance [21-23]. The best performance of this type of solar cells is 11.9%. Figure 1.9 shows the schematic structure of DSSC.

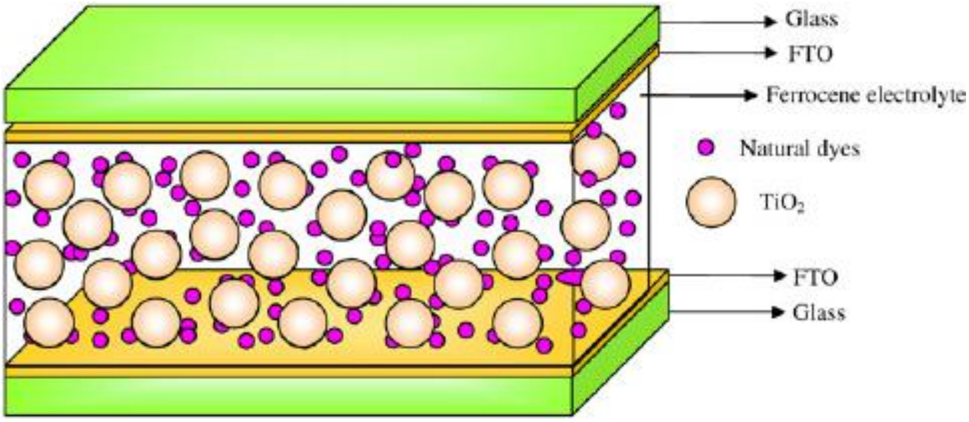

Figure 1.9. Schematic structure of DSSC [24].

1.6 Organic solar cell (OSC)

Based on thin film polymers, small molecules, or both, organic photovoltaic cells usually are fabricated by very simple and cost-efficient techniques, such as spin coating, spray deposition, and printing. OSVs are usually divided into small-molecule solar cells and polymer solar cells. The best performance of this type of solar cell is 12.6%. The organic solar cell structure is shown in Figure 1.10 [25].

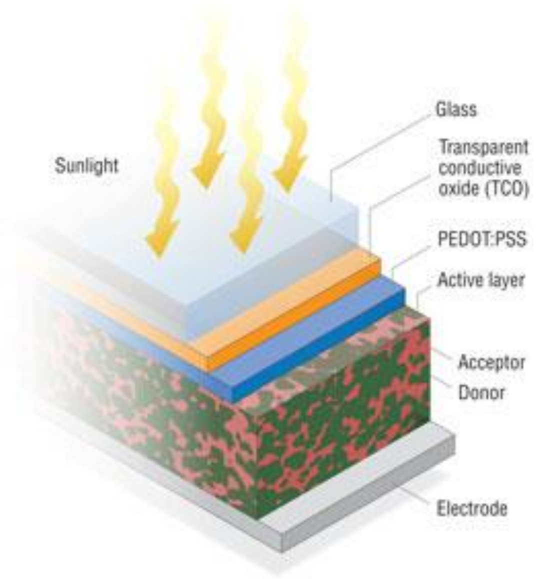

Figure 1.10. Structure of the organic solar cell.

1.7 Overview of The Inorganic-organic Hybrid Perovskite Solar Cells

With the rapid increase of efficiency up to 23.3% during the past few years, being a low-cost and high-performance photovoltaic device, the hybrid organic–inorganic halide perovskite solar cell has attracted extensive attention [2-4, 26]. The unique properties of these absorber layers provide a number of advantages in optoelectronic applications that in many ways originate from the nature of the perovskite lattice [27-29]. The perovskite light absorption layer has a general formula of ABX_3, where A is an organic cation or inorganic cation (e.g., methyl-ammonium MA^+, formamidinium FA^+, Cesium [Cs^+], rubidium Rb^+), B is a metal cation (e.g., Pb^{2+}, Sn^{2+}) and X stands for the halide anion (e.g., I^-, Br^-, Cl^-,). The crystal lattice of the methylammonium lead halide (CH_3NH_3-PbX_3) perovskite structure is shown in Figure 1.11 [30]. Methyl-ammonium-lead-iodide (MAPbI3) is the most widely used perovskite light absorber. Additionally, several organic cations ($NH_2CH{=}NH_2^+$), inorganic cations (Cs^{2+} and Sn^{2+}) and halide anions (Br^-, Cl^-) have been used to improve the efficiency and stability [31, 32].

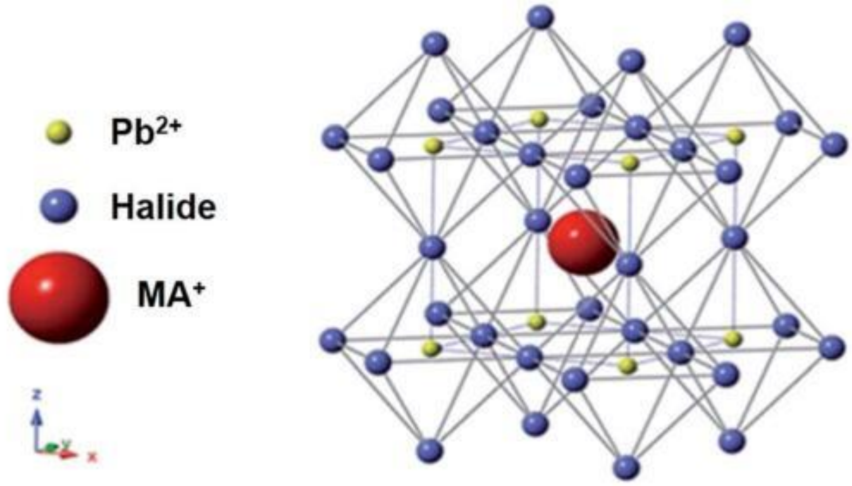

Fig. 1.11. Crystal lattice of the methylammonium lead halide (CH_3NH_3-PbX_3) perovskite structure.

The first record of perovskite-based solar cell which based on a DSSC structure was reported by Miyasaka et al., the efficiency is only 3.8% [33]. The boost of the efficiency was started from the application of solid-state HTM onto the highly-crystallized perovskite layer. Lee et al. [34] reported a breakthrough device efficiency of 10.9% in 2012. A remarkable efficiency of 20.1% was achieved due to the application of another perovskite material, formamidinium iodide ($HC(NH_2)_2PbI_3$, FAI) together with poly-triarylamine (PTAA) as a new HTM in 2015 [2]. The current record efficiency of PSCs was 23.3 which is shown in Figure 1.4.

1.7.1 Techniques for preparing the perovskite film

As the core part of perovskite solar cells, the morphology and crystal structure of perovskite absorbers are vital for achieving high-performance devices. Various thin-film deposition techniques have been studied for the fabrication of high performance devices, such as the solution processing technique, vapor-assisted solution technique, thermal evaporation, spray deposition and doctor blading. The basic chemical process for the synthesis of the perovskite layer involves the reaction between the organic precursors, such as MAI and FAI, and the inorganic precursors, such as PbI_2, $PbCl_2$ and $PbBr_2$.

1.7.1.1 Solution deposition process

One-step spin coating. Due to the easy operation and low cost, one step deposition was widely used in PSC fabrication. In this approach, a mixture of metal halide and organohalide of certain ratio is dissolved in a common solvent and spin-coated on a substrate [35]. This approache had a great starting point of a 10.9% efficiency reported by Lee et al [36], where the MAI and $PbCl_2$ were dissolved in DMF in a molar ratio of 3:1. However, due to poor film formation (incomplete surface coverage with pinholes) induced by extensive crystallization caused by solvent evaporation and strong ionic interaction between the metal cations and the halides [37,38], efficiencies of planar devices prepared using this method are usually limited. The solvent engineering approach demonstrated by Jeon et al. is an attractive approach to aviod the limitations of the one-step spin-coating process, which tends to yield an inhomogeneous perovskite film hampering its reproducibility [39]. The perovskite film is deposited from a precursor solution dissolved in a mixture of dimethylsulfoxide (DMSO) and g-butyrolactone (GBL) (DSMO : GBL = 3 : 7 v/v), immediately followed by a toluene drip while the substrate is spinning, the schematic image of this procedure for perovskite film preparation is shown in Figure 1.12. Owing to the miscibility with both DMSO and GBL, toluene was chosen in this process, so that it does not dissolve the precursor materials. Therefore, the toluene drip removes excess DMSO solvent and encourages supersaturation in the cast film and hence fast nucleation.

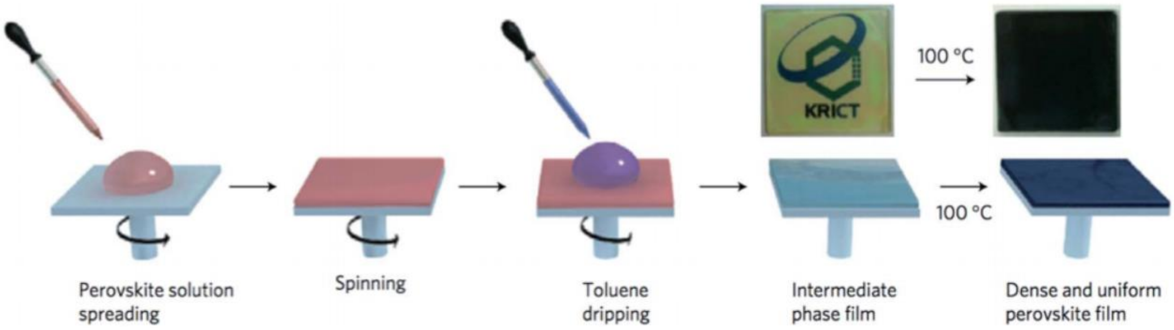

Figure 1.12. Schematic image of solvent engineering procedure for perovskite film preparation [40].

Two-step spin coating. The perovskite deposition by two steps separates the coating of PbX_2 (X=Cl, Br or I) and MAI/FAI layers. First, a PbX_2 seed layer would be spin-coated on a substrate. Next, the MAI/FAI incorporation would be done by either dipping the PbX_2-covered substrate into MAI/FAI solution [41] or spin-coating of MAI/FAI [42] solution. This approach offers the possibility of a more controlled crystallization of perovskite [43,44]. The schematic image of two-step deposition approach is shown in Figure 1.13 [3]. By using this approach, Grätzel group for the first time successfully fabricated perovskite cell that had 15% efficiency [45]. Similar as one-step method, proper solution engineering including solvent mixing and use of additives could be also applicable to two-step fabricated PSCs. Li et al. [3] reported a method by mixing DMSO with DMF, the resulted PCE was 17.16%. The better coordination of DMSO with PbI_2 and an extra intermolecular exchange between DMSO and MAI can assist the decomposition of intermediate state and the formation of perovskite. Another work used two-step method achieved a PCE of 20.2% by introducing PTAA and taking advantage of intramolecular exchange with DMSO catalysis [46].

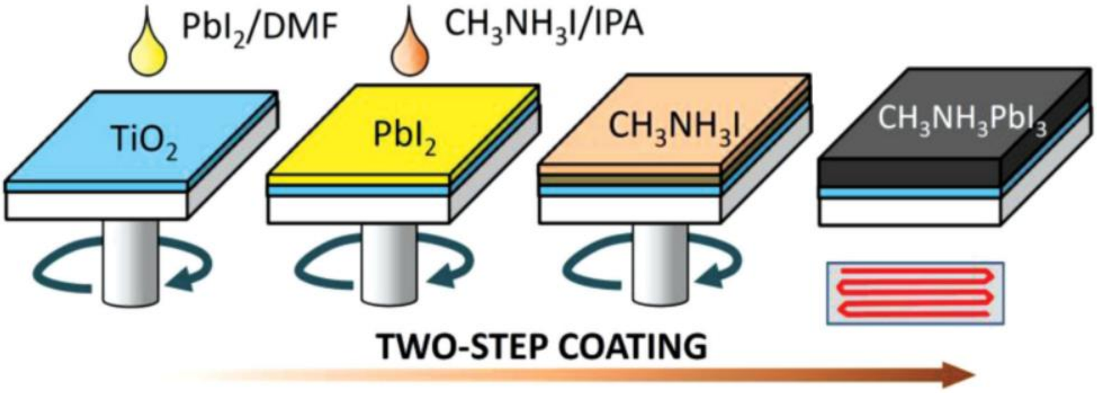

Figure 1.13. Schematic image of two-step deposition approach.

1.7.1.2 Vapor-assisted solution process

Vapor-assisted solution method could be considered as a modified two-step method. During the second step, vaporized MAI/FAI reacted with PbI_2 to form perovskite phase after further film annealing. Chen et al. [47] used as-synthesized MAI vapor (very small particles) applied on spin-coated PbI_2 precursor under a 150 °C baking. The whole perovskite fabrication was done in glove box. This approach was later modified by transferring a two-step as-deposited $MAPbCl_{3-x}I_x$ on ITO/PEDOT:PSS substrate into a closed petri dish container and heated together with MACl powder starting from 100 °C, which resulted a PCE improvement of 15.1% with a 60-day stability [48]. Figure 1.14 shows a detail description about this process. Recently, a device with a planar structure of was fabricated by heating FTO/c-TiO_2/C_{60}/PbI_2 with uniformly-spread FAI and MAI powders in low vacuum under 170 °C for 30 min. By adjusting the powder ratio, they finally achieved a PCE of 16.48% [49].

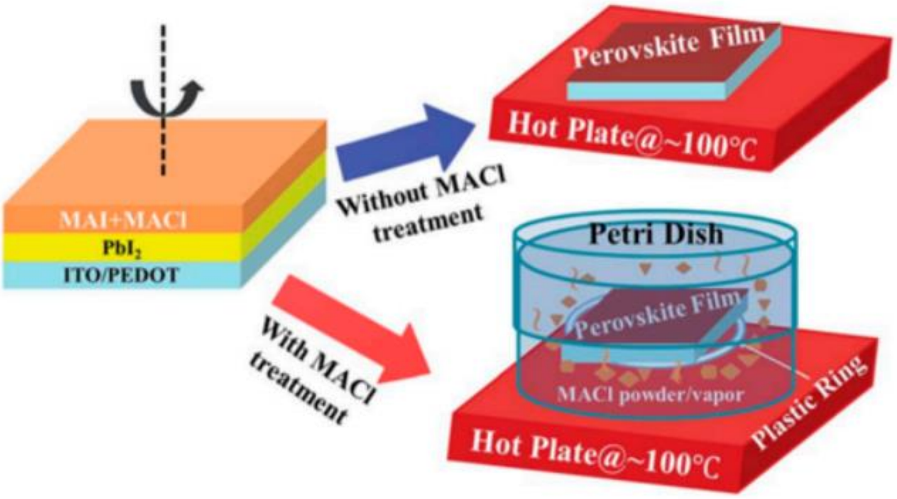

Figure 1.14. Schematic image of vapor-assisted perovskite deposition process [48].

1.7.1.3 Hybrid chemical vapor deposition

Hybrid chemical vapor deposition is a modified method of Vapor-assisted solution process in which the MAI powder and as-deposited PbX_2 film are heated at different temperatures. Matthew R. Leyden et al. [50] first applied this method by loading the pre-deposited $PbCl_2$ film and MAI powder into a furnace at two different temperature zones of 130° C and 185° C, respectively, under a pressure of 100 Pa. The schematic diagram of the HCVD method is shown in Figure 1.15. The resulted efficiency is 11.8%. In Jun Yin's work [51], they used a hot air flow to heat the MAI powder and PbI_2 film. The hot air flow can simultaneously carry the MAI vapor downstream to the PbI_2 film to facilitate the growing of perovskite films with large grain sizes. The highest PCE is 18%.

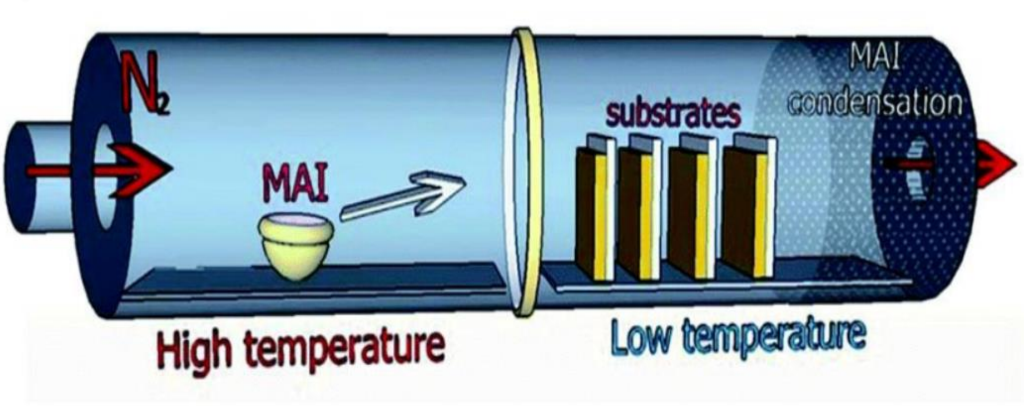

Figure 1.15. The schematic diagram of the HCVD method.

1.7.1.4 Thermal evaporation deposition

Liu et al. [52] applied a dual-source co-evaporation with sources of MAI and $PbCl_2/PbI_2$ on rotated substrate under a high vacuum and they fabricated a planar structure PSC of 15.4%. Figure 1.16 showed the evaporation system. Olga Malinkiewicz et al. [53] deposited a uniform $MAPbI_3$ film by heating two ceramic crucibles filled with MAI and PbI_2 to 70 °C and 250 °C, respectively. A PCE of 12.04% was achieved.

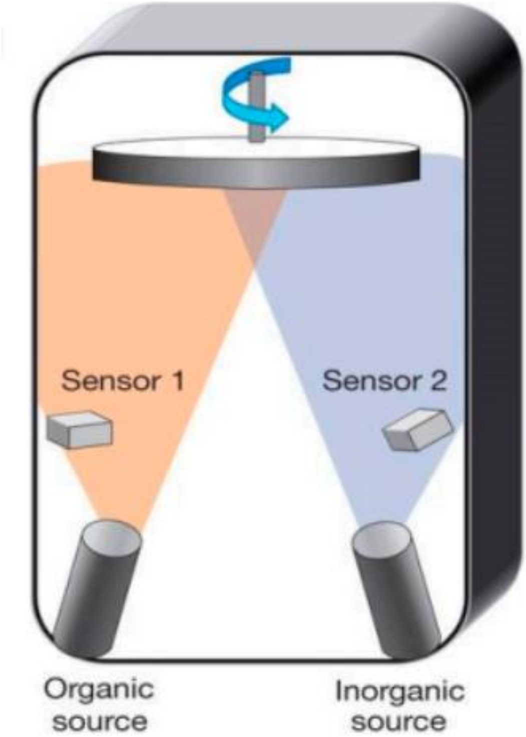

Figure 1.16. Schematic draw of dual-source thermal evaporation system.

1.7.1.4 Spray deposition

Ultrasonic spray-coating was demonstrated by Barrow et al. [54], they fabricated planar perovskite solar cells by using this method under ambient conditions. Figure 1.17. shows the schematic image of spray deposition system. The perovskite films were deposited onto the compact TiO_2 substrate under ambient conditions by using a

Prism ultrasonic spray-coating system. During perovskite precursor spray-coating, the compact TiO_2 substrates were heated at 75℃. After that, the substrates are transferred onto the hotplate for thermal annealing.

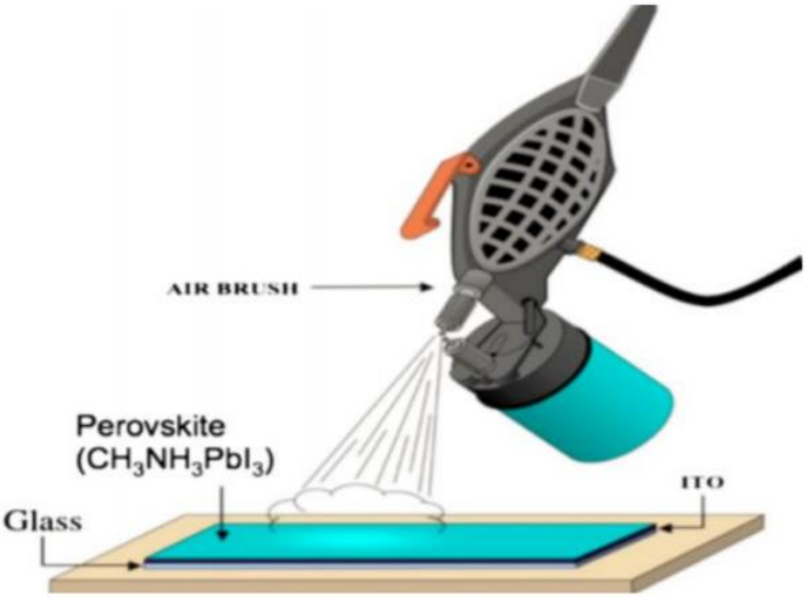

Figure 1.17. Schematic image of spray deposition method system.

1.7.1.4 Doctor blading techniques

Deng et al. used a scalable doctor-blade coating to fabricate $MA_{0.6}FA_{0.4}PbI_3$ PSCs, obtaining a high efficiency of 18.3% [55]. Figure 1.18 shows the schematic of doctor-blading fabrication methods. The thickness of the perovskite film was controlled by adjusting the concentration of the precursor solution and the blade-coating speed. A perovskite module with 11.09 cm^2 active area has a PCE of 14.06% which was fabricated by blade-coating. It is confirmed that by using blade-coating technique the high quality of the perovskite films can be produced over a large substrate area.

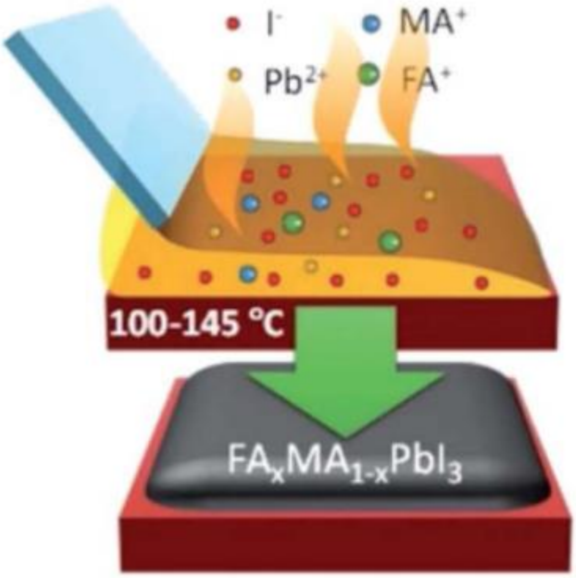

Figure 1.18. Schematic of doctor-blading fabrication methods.

1.7.2 Structures of perovskite solar cell

The architecture is an important item that can affect the device performance of perovskite solar cells. It can dictate the choice of materials, the deposition techniques for the material and the compatibility between the different components in the device. Two common architectures of perovskite solar cells have been developed, they are mesoscopic and planar structures. Figure 1.19 shows schematic image of the device structures and energetics.

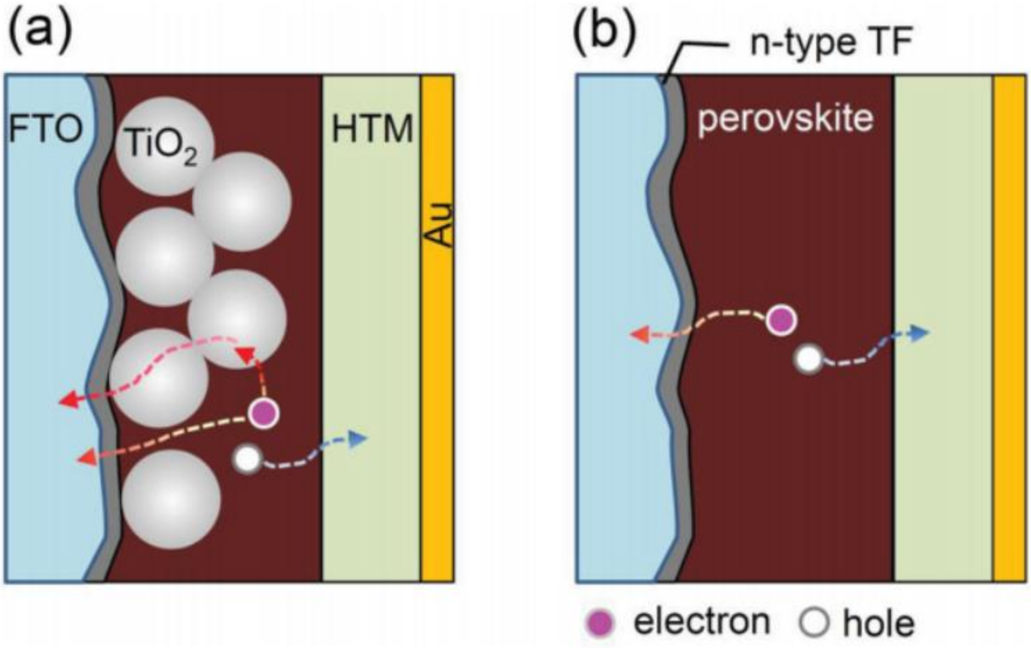

Figure 1.19. (a) Mesoscopic perovskite solar cell with mesoporous TiO_2 layer and (b) planar structure without a mesoporous TiO_2 layer [56].

1.7.2.1 Mesoscopic architecture of perovskite solar cell

So far, TiO_2 nanoparticles have been the most commonly employed materials as the scaffold for mesoscopic perovskite solar cells. This porous TiO_2 film not only extracts photoexcited electrons generated in the absorber layer [57] but also increases the perovskite crystal transformation when the perovskite layer is fabricated by using solution deposition process [58]. Many publications suggest that the efficiency of mesoscopic perovskite solar cells is strongly dependent to the thickness of the TiO_2 scaffold layer. Unlike DSSCs which required a thick TiO_2 scaffold (~ 3 μm) to achieve sufficient absorption, perovskite solar cells only need a submicron thick mesoporous TiO_2 layer to achieve good performance [59]. At present, tremendous attention has been paid on the optimization of this mesoporous TiO_2-based device, including the modification of the TiO_2 nanostructure, perovskite layer and HTM.

It should be noted that besides TiO_2 nanoparticles, TiO_2 nanocrystals in other forms (e.g., nanorods, nanowires, nanofibers, nanotubes and nanocones) and similar n-type materials such as ZnO and Al_2O_3 have been applied to make the scaffold for mesoscopic perovskite solar cells, which can also act as an efficient electron collector [60-65]. Nanostructured ZnO is a viable n-type alternative scaffold to mesoporous TiO_2 for perovskite solar cells due to its comparable energy levels as well as relatively higher electron mobility [66,67]. Park et al. [68] used ZnO nanorods arrays as the scaffold to fabricate the PSCs, the final the PCE to 11.13%. Figure 1.20 shows the fabrication procedure of the perovskite solar cell based on the ZnO nanorod scaffold. Snaith and coworkers used insulating mesoporous Al_2O_3 to replace mesoporous TiO_2 [69]. No photoexcited electrons were injected into Al_2O_3 but directly transported throughout the perovskite layer and were collected at the compact TiO_2-coated FTO electrode, this can be seen in Figure 1.21. Unlike the mesoporous n-type TiO_2-based perovskite solar cells, Al_2O_3 acts only as a “scaffold” and the perovskite layer functions both as an intrinsic absorber and electron transporter.

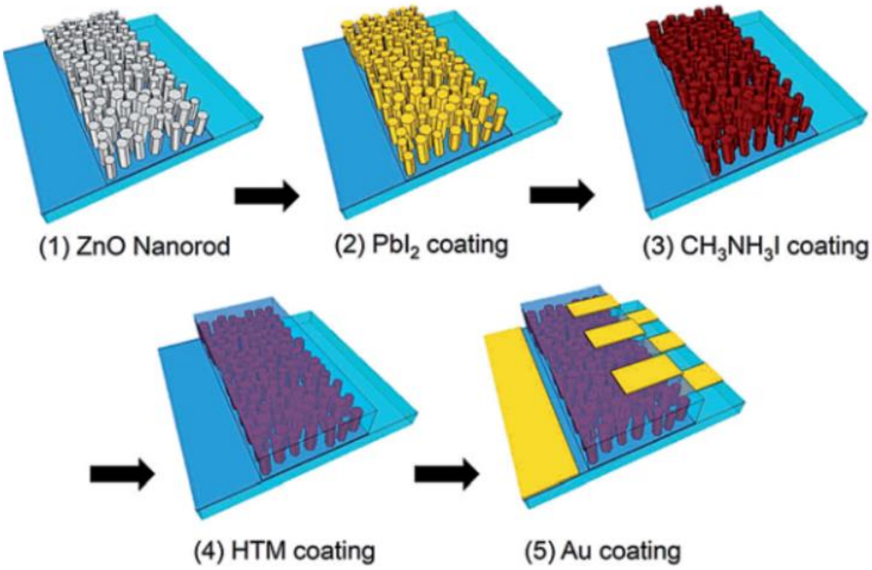

Figure 1.20. Fabrication procedure of the perovskite solar cell based on the ZnO nanorod scaffold.

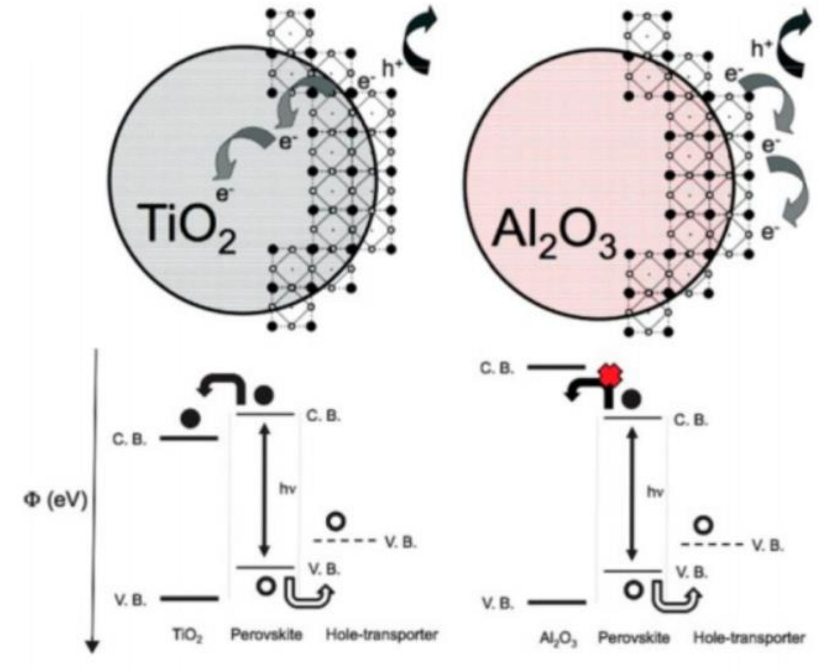

Figure 1.21. The schematic of perovskite-coated TiO2 and Al2O3, illustrating electron and hole transfer.

The interface engineering of mesoscopic materials is one good way to optimize charge transport and recombination. Recently, an ultrathin MgO nanolayer was applied to retard charge recombination between the electrons injected into TiO_2 nanoparticles and the holes in perovskite materials [2].

1.7.2.2 Planar architecture of perovskite solar cell

There are two different types of device structure for the planar architecture of perovskite solar cells. One is "n-i-p" planar architecture (FTO/ETL/perovskite/HTL/Au), and another is the "p-i-n" planar inverted structure (FTO/HTL/perovskite/ETL/Ag).

"n–i–p" planar perovskite solar cells. The critical factor which can determine the resulting device performance is the morphology of the absorber layer. In 2013, Snaith et al. fabricated the PSCs in the planar structure with a high $MAPbI_{3-x}Cl_x$ perovskite coverage, the final PCE is 11.4% [70]. Later, Han and coworkers optimized the solution deposition process, using a strongly coordinative solvent (DMSO) instead of the commonly used DMF to dissolve PbI_2 and fabricate PbI_2 films, the obtained

$MAPbI_3$ perovskite film with relatively uniform distributions of crystal sizes [47]. Planar structure device demonstrated good reproducibility and yielded the highest PCE of 13.5%. Spiccia and coworker reported a planar structure PSC by using one-step, solvent-induced, fast crystallization method to control the dynamics of nucleation and grain growth of $MAPbI_3$. The resulted maximum PCE is 16.2% [71]. Kelly and coworkers reported the application of a thin ZnO nanoparticle film as an electron-transport layer in a planar structure solar cell (ITO/bl-ZnO/MAPbI3/spiro-OMeTAD/Ag) [72]. The higher electron mobility of ZnO than that of TiO_2 [73] and the large crystallite size resulted in a higher J_{sc} (20.4 mA cm^{-2}) with a PCE of 15.7%.

Besides the modification of the perovskite layer and ETL, other types of p–i–n junctions with different p-type HTMs such as organic P3HT [72], PTB7-Th [74] and inorganic CuSCN [75] were also reported with favorable performance achieved.

Additionally, in the planar structure, the interface engineering also impacts on the charge transport and recombination. Yang's group applied polyethyleneimine ethoxylate (PEIE) to modify the ITO layer with reduced the work function and by doping yttrium into the TiO_2 compact layer to increase the carrier density. As a result, the electron transport channel in the planar structure perovskite solar cell can be improved [76].

Inverted "p–i–n" planar perovskite solar cells. Guo and coworkers firstly reported a inverted devices based on a planar junction of $MAPbI_3$ perovskite/fullerene-derivative structure, in which $MAPbI_3$ acted as a "donor" material while C60, PC60BM or an indene–C60 bisad-duct (IC60BA) acted as the "acceptor" material (consisting of glass/ITO/PEDOT:PSS as the positive electrode, a thin bathocuproine (BCP) film as the hole-blocking layer, and an Al negative electrode) [4]. In order to modify the interface work function and then reduce the potential energy loss, Lee et al. applied a new self-organized hole extraction layer, which was composed of PEDOT:PSS and a perfluorinated ionomer (PFI), and the resulted PCE is 11.7% [42]. Later, Huang et al used interdiffusion of spin-coated stacking layers of PbI_2 and MAI to form a high quality film [77]. Device based on an ITO/PEDOT:PSS/MAPbI3/PC60BM/C60/BCP/Al structure obtained a PCE of 15.3%.

1.7.3 Stability of perovskite solar cells

A long device lifetime of PPSCs is the ultimate goal. This requires proper means to avoid the water, air and high energy photons getting into the device and destroying the perovskite, and to prevent the degradation of the electrode. Figure 1.22 shows the products of the decomposition process cause the degradation of a perovskite solar cell in several pathways. This process was observed by Yu Han et al. through applying the cross-sectional FIB-SEM technique [78]. Seok's group [21] observed that at a humidity of 55 RH% the PCE of a $MAPbI_3$-based solar cell suffers a faster decrease than that at 35 RH%, which confirmed the influence of water on the stability of perovskite solar cells. Temperature is another vital factor that can affect the decomposition of a perovskite film. As known the solar-illumination-induced temperature is higher than 50 °C, so this problem should not be overlooked. Yi-Bing Cheng and co-workers [79] observed that even at very low humidity (<10%), the devices have a more serious PCE decay at higher temperatures (55-85 °C) than that at lower temperatures (-20-10 °C). A mesoporous TiO_2 layer in the PSCs was used to transport photo-generated electrons. However, TiO_2 is an important semiconductor for photocatalysis [79] and is sensitive to ultraviolet (UV) light. As shown in Figure 1.23 oxygen molecules in air tend to be adsorbed on the oxygen vacancies on the TiO_2 surface. It was hypothesized that under UV light excitation, at the TiO_2 surface, the photogenerated holes in the valence band could recombine with the electrons at oxygen vacancies. As a result, free electrons are left in the conduction band and unfilled oxygen vacancy sites are formed. These deep electronic sites could further trap the photogenerated electrons, and these may act as the sites for the recombination, which results in the instability of the UV-aged perovskite solar cells.

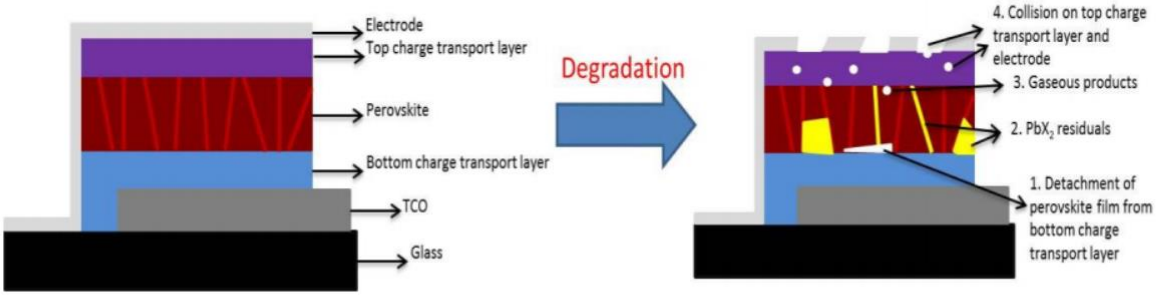

Figure 1.22. Scheme of the degradation of a perovskite solar cell.

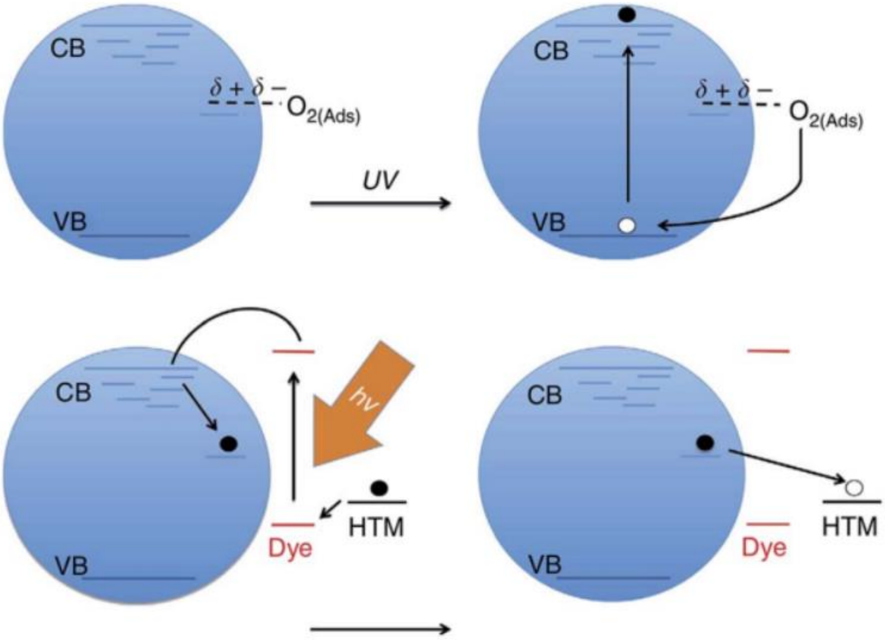

Figure 1.23. Schematics of the proposed mechanism of UV-induced degradation in a TiO2-based solar cell [80].

Many research works have done to optimize the stability of the devices, such as improve the encapsulation techniques, application of barrier layers directly onto perovskites and devices, investigate more stable electrodes and optimize the techniques for growing of perovskite films with larger grain to improve the moisture stability.

1.8 Objectives

This thesis will focus on investigating the influences of growth techniques and structure optimization on the solar cell efficiency and stability. Chapter 2 will introduce the methodology that have been used in the study and the basic characterization techniques. Chapter 3 will focus on investigating the mechanism of use both DMSO and HCl as the additive in the formation of perovskite layer. The charge transport property and stability will also be studied. Chapter 4 will introduce a method for applying the pristine graphene nanofibers into the perovskite layer to facilitate the surface coverage and crystallization of the perovskite layer and also improve the charge transport property. Additionally, the stability of the devices has been studied. Chapter 5 will present a thin structured TiO_2 embedded with graphene nanofibers scaffold. The effect of such scaffold on the formation of perovskite layer and the charge transport property will be investigated. Meanwhile, the stability also has been studied. Chapter 6 will introduce a method to fabricate an ultrathin graphene nanofibers interlayer between the ETL and perovskite layer to reduce the interfacial resistance. Chapter 7 will provide the conclusions of this study.

References

1. Shi. S. W., Li, Y. F., Li. X. Y., Wang, H. Q. *Advancements in all solid-state hybrid solar cells based on organometal halide perovskites.* Mater. Horiz., 2015. **2**: p. 378.
2. Lee. M. M., Teuscher, J., Miyasaka, T., Murakami, T. N. Snaith, H. J. *Efficient Hybrid Solar Cells Based on Meso-Superstructured Organometal Halide Perovskites.* Science*,* 2012. **338**: p. 643.
3. Burschka, J., Pellet, N., Moon, S. J., Humphry-Baker, R. H., Gao, P., Nazeeruddin, M. K. and Gratzel, M. *Sequential Deposition as a Route to High-Performance Perovskite-Sensitized Solar Cells.* Nature, 2013. **499**: p. 316.
4. Zhou, H. P., Chen, Q., Li, G., Luo, S., Song, T., Duan, H., Hong, Z. R., You, J. B., Liu, Y. S., Yang Y., *Photovoltaics. Interface engineering of highly efficient perovskite solar cells.* Science, 2014. **345**: p. 542.
5. Bi, D. et al. *Efficient luminescent solar cells based on tailored mixed-cation perovskites.* Sci. Adv., 2016. **2**: p. 1501170.
6. National Renewable Energy Laboratory (NREL), http://www.nrel.gov
7. Yadav, A. and Kumar, P. *Enhancement in Efficiency of PV Cell through P&O Algorithm.* International Journal for Technological Research in Engineering, 2015. 2: p. 2642.
8. Materials Sciences and Applications, 2015, 6, 1145-1155.
9. Choubey, P. C., Oudhia, A. and Dewangan, R. *A Review: Solar Cell Current Scenario and Future Trends.* Recent Research in Science and Technology, 2012. **4**: p. 99.
10. Srinivas, B., Balaji, S., Nagendra Babu, M. and Reddy, Y. S. (2015) *Review on Present and Advance Materials for Solar Cells.* International Journal of Engineering Research-Online, 2015. **3**: p. 178.
11. Best cell research efficiency. Available from: https://www.nrel.gov/pv/assets/images/efficiency-chart.png.
12. International Technology Roadmap for Photovoltaic: 2016 Results 5th edn

(ITRPV, 2017).

13. Structure of a-Si solar cells. Available from: https://understandsolar.com/thin-film-solar-panels/.
14. Loferski, *J. J. Theoretical considerations governing the choice of the optimum semiconductor for photovoltaic solar energy conversion.* J. Appl. Phys. 1956. **27**: p. 777.
15. Basol, B. M. *Processing high efficiency CdTe solar cells*. Int. J. Solar Energy, 1992. **12**: p. 25.
16. Başol, B. M., McCandless, B. Brief review of cadmium telluride-based photovoltaic
17. Technologies. Journal of Photonics for Energy, 2014. **4**: p. 040996-1.
18. Ramanujam, J., Singh, U. P. *Copper indium gallium selenide based solar cells - a review*. Energy Environ. Sci. 2017. **10**: p. 1306.
19. M. Gratzel, *Photoelectrochemical cells.* Nature, 2001. **414**: p. 338.
20. M. Gratzel, *Solar Energy Conversion by Dye-Sensitized Photo-Voltaic Cells.* Inorganic Chemistry, 2005. **44**: p. 6841.
21. M. Grätzel, *Dye-sensitized solar cells.* Journal of Photochemistry and Photobiology C: Photochemistry Reviews, 2003. **4**: p. 145.
22. Yu, X. L. Song, J. G. Fu, Y. S. Xie, Y. Song, J., Sun, X., Du, X. W. *ZnS/ZnO Heteronanostructure as Photoanode to Enhance the Conversion Efficiency of Dye-Sensitized Solar Cells.* The Journal of Physical Chemistry C, 2011. **114**: p. 2380.
23. Qian, J., Liu, P., Xiao, Y., Jiang, Y., Cao, Y., Ai, X., Yang, H. *TiO2‐Coated Multilayered SnO2 Hollow Microspheres for Dye‐Sensitized Solar Cells.* Advanced Materials, 2009. **21**: p. 3663.
24. Gubbala, S., Chakrapani, V., Kumar, V., Sunkara, M. K., *Band‐Edge Engineered Hybrid Structures for Dye‐Sensitized Solar Cells Based on SnO2 Nanowires*. Advanced Functional Materials, 2008. **18**: p. 2411.
25. Sönmezoğlu, S., Akyürek, C., Akin, S. *High-efficiency dye-sensitized solar cells using ferrocene-based electrolytes and natural photosensitizers*. Journal of

Physics D Applied Physics, 2012. **45**: p. 425101.

26. Structure of organic solar cells. Available from: https://www.energy.gov/eere/solar/organic-photovoltaics-research.
27. Bi, D. et al. *Improving efficiency and stability of perovskite solar cells with photocurable fluoropolymers.* Sci. Adv. 2016. **2**: p. 1501170.
28. Sun, S., Salim, T., Mathews, N., Duchamp, M., Boothroyd, C., Xing, G., Sum, T. C., Lam, Y. M. *The origin of high efficiency in low-temperature solution-processable bilayer organometal halide hybrid solar cells.* Energy Environ. Sci., 2014. **7**: p. 399.
29. Wehrenfennig, C., Liu, M., Snaith, H. J., Johnston, M. B., Herz, L. M. U*ltrafast terahertz probe of photoexcited free charge carriers in organometal CH3NH3PbI3 perovskite thin film*. J. Phys. Chem. Lett., 2014. **5**: p. 1300.
30. Xing, G., Mathews, N., Sun, S., Lim, S. S., Lam, Y. M., Gratzel, M., Mhaisalkar, S., Sum, T. C. *High efficiency solution processed perovskite solar cells with millimeter scaled gain.* Science, 2013. **342**: p. 344.
31. Ku, Z., Rong, Y., Xu, M., Liu, T., Han, H. *Full printable processed mesoscopic CH3NH3PbI3/TiO2 heterojunction solar cells with carbon counter electrode.* Sci. Rep., 2013. **3**: p. 3132.
32. Conings, B., Baeten, L., De Dobbelaere, C., D'Haen, J., Manca, J., Boyen, H. *Perovskite-based hybrid solar cells exceeding 10% efficiency with high reproducibility using a thin film sandwich approach.* Adv. Mater. 2014. **26**: p. 2041.
33. Tan, K.W., Moore, D.T., Saliba, M., Sai, H., Estroff, L.A., Hanrath, T., Snaith, H.J., Wiesner, U. *Thermally induced structural evolution and performance of mesoporous block copolymer-directed alumina PSCs.* ACS Nano 2014. **8**: p. 4730.
34. Kojima, A., Teshima, K., Shirai, Y., Miyasaka, T. *Organometal halide perovskites as visible-light sensitizers for photovoltaic cells.* J. Am. Chem. Soc. 2009. **131**: p. 6050.
35. Yang, W. S., Noh, J. H., Jeon, N. J., Kim, Y. C., Ryu, S., Seo, J., Seok, S. I. *High-performance photovoltaic perovskite layers fabricated through*

intramolecular exchange. Science, 2015. **348**: p. 1234.

36. Kim, H. S., Lee, C. R., Im, J. H., Lee, K. B., Moehl, T., Marchioro, A., Moon, S. J., Humphry-Baker, R., Yum, J. H., Moser, J. E., Gratzel, M., Park, N. G. *Lead iodide perovskite sensitized all-solid-state submicron thin film mesoscopic solar cell with efficiency exceeding 9%.* Sci. Rep., 2012. **2**: p. DOI: 591.
37. Lee, M. M., Teuscher, J., Miyasaka, T., Murakami, T. N., Snaith, H. J. *Efficient hybrid solar cells based on meso-superstructured organometal halide perovskites.* Science, 2012. **338**, 643.
38. Jeng, J. Y., Chiang, Y. F., Lee, M. H., Peng, S. R., Guo, T. F., Chen, P., Wen, T. C. *High-performance planar heterojunction perovskite solar cells: Preserving long charge carrier diffusion lengths and interfacial engineering.* Adv. Mater., 2013. **25**: p. 3727.
39. Chiang, Y. F., Jeng, J. Y., Lee, M. H., Peng, S. R., Chen, P., Guo, T. F., Wen, T. C., Hsu, Y. J., Hsu, C. M. *Perovskite thin-film solar cell: excitation in photovoltaic science.* Phys. Chem. Chem. Phys., 2014. **16**: p. 6033.
40. Jeon, N. J., Noh, J. H., Kim, Y. C., Yang, W. S., Ryu, S., Seok, S. I. *Solvent engineering for high-performance inorganic–organic hybrid perovskite solar cells.* Nat. Mater., 2014. **13**: p. 897.
41. Bi, D., El-Zohry, A. M., Hagfeldt, A., Boschloo, G. *Improved morphology control using a modified two-step method for efficient PSCs.* ACS Appl. Mater. Interfaces 2014. **6**: p. 18751.
42. Xiao, M., Huang, F., Huang, W., Dkhissi, Y., Zhu, Y., Etheridge, J., Gray-Weale, A., Bach, U., Cheng, Y.B., Spiccia, L. *A fast deposition-crystallization procedure for highly efficient lead iodide perovskite thin-film solar cells.* Angew. Chem. 2014. **126**: p. 10056.
43. Eperon, G. E., Burlakov, V. M., Docampo, P., Goriely, A., Snaith, H. J. *Morphological Control for High Performance, Solution-Processed Planar Heterojunction Perovskite Solar Cell.* Adv. Funct. Mater., 2014. **24**: p. 151.
44. Im, J. H., et al., *Growth of CH3NH3PbI3 cuboids with controlled size for high-efficiency perovskite solar cells.* Nature nanotechnology, 2014. **9**: p. 927.

45. Li, W., Fan, J., Li, J., Mai, Y., Wang, L. *Controllable grainmorphology of perovskite absorber filmbymolecular self-assembly toward efficient solar cell exceeding 17%.* J. Am. Chem. Soc. 2015. **137**: p. 10399.
46. Yang, W. S., Noh, J. H., Jeon, N. J., Kim, Y. C., Ryu, S., Seo, J., Seok, S. I. *High-performance photovoltaic perovskite layers fabricated through intramolecular exchange.* Science, 2015. **348**, 1234.
47. Chen, S., Lei, L., Yang, S., Liu, Y, Wang, Z. S. *Characterization of perovskite obtained from two-step deposition on mesoporous titania.* ACS Appl. Mater. Interfaces, 2015. **7**: p. 25770.
48. Khadka, D. B. Shirai, Y., Yanagida, M., Masuda, T., Miyano, K. *Enhancement in efficiency and optoelectronic quality of perovskite thin films annealed in MACl vapor.* Sustain. Energy Fuels, 2017. **1**: p. 755.
49. Chen, J., Xu, J., Xiao, L., Zhang, B., Dai, S., Yao, J. *Mixed-organic-cation (FA)x(MA)1−xPbI3 planar PSCs with 16.48% efficiency via a low-pressure vapor-assisted solution process.* ACS Appl. Mater. Interfaces, 2017. **9**: p. 2449.
50. Leyden, M. R., et al. *High performance perovskite solar cells by hybrid chemical vapor deposition.* J. Mater. Chem. A, 2014. **2**: p. 18742.
51. Yin, J., et al. *Vapor-assisted crystallization control toward high performance perovskite photovoltaics with over 18% efficiency in the ambient atmosphere.* J. Mater. Chem. A, 2016. **4**: p. 13203.
52. Liu, M., Johnston, M. B., Snaith, H. J. *Efficient planar heterojunction PSCs by vapor deposition.* Nature 2013. **501**: p. 395.
53. Malinkiewicz, O., et al. *Perovskite solar cells employing organic charge-transport layers.* Nature Photonics, 2013. **8**: p. 128.
54. Barrows, A.T., et al. *Efficient planar heterojunction mixed-halide perovskite solar cells deposited via spray-deposition.* Energy & Environmental Science, 2014. **7**: p. 2944.
55. Deng, Y., Dong, Q., Bi, C., Yuan, Y., Huang, J. *Air‐Stable, Efficient Mixed‐Cation Perovskite Solar Cells with Cu Electrode by Scalable Fabrication of Active Layer*. Adv. Energy Mater., 2016. **6**: p. 1600372.

56. Jung, H. S., Park, N. G. *Perovskite Solar Cells: From Materials to Devices*. Small, 2015. **11**, 1: p. 10.
57. Bai, Y., Mora-Sero, I., De Angelis, F., Bisquert, J., Wang, P. T*itanium Dioxide Nanomaterials for Photovoltaic Applications*. Chem. Rev., 2014. **114**: p. 10095.
58. Murugadoss, G., Mizuta, G., Tanaka, S., Nishino, H., Umeyama, T., Imahori, H., Ito, S. *Remnant PbI2, an unforeseen necessity in high-efficiency hybrid perovskite-based solar cells.* APL Mater. 2014. **2**: p. 081511.
59. Kim, H. S., Lee, C. R., Im, J. H., Lee, K. B., Moehl, T., Marchioro, A., Moon, S. J., Humphry-Baker, R., Yum, J. H., Moser, J. E., Gratzel, M., Park, N. G. *Migration: Flooding and the scale of migration.* Sci. Rep. 2012. **2**: p. 401.
60. Bi, D., Boschloo, G., Schwarzmuller, S., Yang, L., Johansson, E. M. J., Hagfeldt, A. *Efficient and stable CH3NH3PbI3-sensitized ZnO nanorod array solid-state solar cells.* Nanoscale, 2013. **5**: p. 11686.
61. Son, D. Y., Im, J. H., Kim, H. S., Park, N. G. *11% Efficient Perovskite Solar Cell Based on ZnO Nanorods: An Effective Charge Collection System.* J. Phys. Chem. C, 2014. **118**: p. 16567.
62. Gao, X., Li, J., Baker, J., Hou, Y., Guan, D., Chen, J., Yuan, C. *Electrochemical Infilling of CuInSe2 within TiO2 Nanotube Layers and Subsequent Photoelectrochemical Studies.* Chem. Commun., 2014. **50**: p. 6368.
63. Qiu, J., Qiu, Y., Yan, K., Zhong, M., Mu, C., Yan, H., Yang, S. *All-solid-state hybrid solar cells based on a new organometal halide perovskite sensitizer and one-dimensional TiO2 nanowire arrays.* Nanoscale, 2013. **5**: p. 3245.
64. Manseki, K., Ikeya, T., Tamura, A., Ban, T., Sugiura, T., Yoshida, T. *Mg-doped TiO2 nanorods improving open-circuit voltages of ammonium lead halide perovskite solar cells.* RSC Adv., 2014. **4**: p. 9652.
65. Zhong, D., Cai, B., Wang, X., Yang, Z., Xing, Y., Miao, S., Zhang, W. H., Li, C. *Synthesis of oriented TiO2 nanocones with fast charge transfer for perovskite solar cells.* Nano Energy, 2015. **11**: p. 409.
66. Zhang, Q., Dandeneau, C. S., Zhou, X., Cao, G. *Zno nanostructures for dye-strongsensitizedstrong solar cells.* Adv. Mater., 2009. **21**: p. 4087.

67. Anta, J. A., Guille ́n, E., Tena-Zaera, R. *ZnO-Based Dye-Sensitized Solar Cells.* J. Phys. Chem. C, 2012. **116**: p. 11413.
68. Son, D. Y., Im, J. H., Kim, H. S., Park, N. G. *11% Efficient Perovskite Solar Cell Based on ZnO Nanorods: An Effective Charge Collection System.* J. Phys. Chem. C, 2014, 118, 16567.
69. Han, G. S., Chung, H. S., Kim, B. J., Kim, D. H., Lee, J. W., Swain, B. S., Mahmood, K., Yu, J. S., Park, N.-G., Lee, J. H., Jung, H. S. *Air-stable high-efficiency solar cells with dry-transferred single-walled carbon nanotube films.* J. Mater. Chem. A, 2014. **2**: p. 11311.
70. Wu, Y., Islam, A., Yang, X., Qin, C., Liu, J., Zhang, K., Peng, W., Han, L. *Retarding the crystallization of PbI2 for highly reproducible planar-structured perovskite solar cells via sequential deposition.* Energy Environ. Sci., 2014. **7**: p. 2934.
71. Xiao, M., Huang, F., Huang, W., Dkhissi, Y., Zhu, Y., Etheridge, J., Gray-Weale, A., Bach, U., Cheng, Y. B., Spiccia, L. *A Fast Deposition‐Crystallization Procedure for Highly Efficient Lead Iodide Perovskite Thin‐Film Solar Cells.* Angew. Chem., Int. Ed., 2014. **53**: p. 9898.
72. Liu, D., Kelly, T. L. *Perovskite solar cells with a planar heterojunction structure prepared using room-temperature solution processing techniques.* Nat. Photonics, 2013. **8**: p. 133.
73. Conings, B., Baeten, L., Jacobs, T., Dera, R., D'Haen, J., Manca, J., Boyen, H. G. *An easy-to-fabricate low-temperature TiO2 electron collection layer for high efficiency planar heterojunction perovskite solar cells.* APL Mater., 2014. **2**: p. 081505.
74. Kim, J., Kim, G., Kim, T. K., Kwon, S., Back, H., Lee, J., Lee, S. H., Kang, H., Lee, K. *Efficient planar-heterojunction perovskite solar cells achieved via interfacial modification of a sol–gel ZnO electron collection layer.* J. Mater. Chem. A, 2014. **2**: p. 17291.
75. Chavhan, S., Miguel, O., Grande, H. J., Gonzalez-Pedro, V., Sanchez, R. S., Barea, E. M., Mora-Sero, I., Tena-Zaera, R. *Organo-metal halide perovskite-based solar*

cells with CuSCN as the inorganic hole selective contact. J. Mater. Chem. A, 2014. **2**: p. 12754.

76. Lim, K. G., Kim, H. B., Jeong, J., Kim, H., Kim, J. Y., Lee, T.-W. *Boosting the Power Conversion Efficiency of Perovskite Solar Cells Using Self‐Organized Polymeric Hole Extraction Layers with High Work Function.* Adv. Mater., 2014. **26**: p. 6461.
77. Xiao, Z., Bi, C., Shao, Y., Dong, Q., Wang, Q., Yuan, Y., Wang, C., Gao, Y., Huang, J. *Efficient, high yield perovskite photovoltaic devices grown by interdiffusion of solution-processed precursor stacking layers.* Energy Environ. Sci., 2014. **7**: p. 2619.
78. Han, Y., et al. *Degradation observations of encapsulated planar CH3NH3PbI3perovskite solar cells at high temperatures and humidity.* J. Mater. Chem. A, 2015. 3: p. 8139.
79. Mills, A., Hunte. S. L. *An overview of semiconductor photocatalysis. J. Photochem*. Photobiol. A Chem. 1997. 108: p. 1.
80. Leijtens, T., Eperon, G. E., Pathak, S., Abate, A., Lee, M. M., Snaith, H. J. *Overcoming ultraviolet light instability of sensitized TiO2 with meso-superstructured organometal tri-halide perovskite solar cells.* Nat. Commun., 2013. **4**: p. 2885.

Chapter 2

Methodology

2.1 Introduction

This chapter describes the methodology for the fabrication of graphene suspension and the nanofibers. The characterization methods of the devices and the target compounds can be found in this chapter. The generation of the intermediates are also explicated in detail.

2.2 Materials and Reagents

Table 2. 1 Experimental chemicals.

Material Name	**Manufactory**	**Purity**
Titanium isopropoxide (TIP)	Sigma Aldrich	97%
Polyvinyl pyrrolidone (PVP) (MW = 1,300,000)	Sigma Aldrich	NA
Acetic acid (HAc)	Sigma Aldrich	≥99.7%
Ethanol	Advanced	95%
Graphite powder	Sigma Aldrich	NA
Titanium tetrachloride	International Laboratory USA	≥99%
Dimethyl sulfoxide（DMSO）	DUKSAN	99%

N,N-Dimethylformamide (DMF)	Sigma Aldrich	99.8%
Lead(II) iodide (PbI_2)	Sigma Aldrich	99%
Toluene	DUKSAN	99.9%
Methylammonium iodide (MAI)	Dyesol	NA
Isopropanol (IPA)	AQA	99.5%
Hydrochloric acid (HCl)	Sigma Aldrich	37%
4-tert-butylpyridine (TBP)	Sigma Aldrich	96%
Lithium bis(trifluoromethane)sulfonimide	Sigma Aldrich	NA
Acetonitrile	DUKSAN	99.9%
Chorobenzene	DUKSAN	99.8%
Molybdenum trioxide (MoO_3)	Sigma Aldrich	99.97%
Spiro-MeOTAD	Luminescence Technology Corp	NA
Gold	Kurt J. Lesker	99.99%

2.3 Fabrication of nanofibers

2.3.1 Preparation of graphene solution

Graphene can be obtained by using a demonstrated method [1] for shear exfoliation of graphite, shear exfoliation can produce large quantities of defect-free, unoxidized graphene. In our study, 5% PVP was dissolved in ethanol and was assisted by ultrasonic stirring. 5 wt.% graphite powder was added to the solution and blended with a Philips HR2096 blender at 21,000 rpm. The turbulence induced shearing causing the graphitic planes to slip relative to each other until full exfoliation was achieved, resulting in free floating graphene. The graphene was subsequently bound to the PVP in the solution, preventing re-aggregation of graphene into graphite. The solution was typically blended for 20 min until a suspension of graphene and graphite was formed. The suspension was subsequently centrifuged at 9993g (1g = 9.81 m/s^2) for 3–60 min for removal of denser residual and larger size graphene sheets to obtain pure graphene suspension with smaller graphene sheets. Subsequently, the graphene suspension was used for electrospinning. The flow chart for preparing graphene suspension is shown in Figure 2.1.

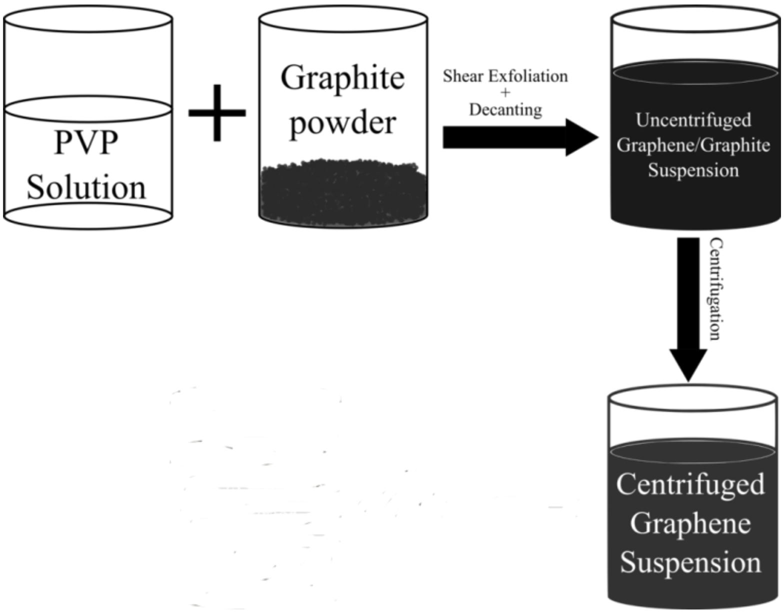

Figure 2.1. Flow chart for preparing graphene suspension.

2.3.2 Fabrication of graphene nanofibers

Electrospinning is a widely used and one of the simplest techniques to produce the one-dimensional nanofibers with diameters in the range of several nanometers to the micrometer regime. By using electrospinning technique, nanofibers can be successfully produced from organic polymers, semiconductors and their composites.

The nozzle-less electrospinning device is applied to fabricate graphene nanofibers. The schematic setup for nozzle-less electrospinning is shown in Figure 2.2a, b. The rotating electrode half submerged in a trough of feed solution, and the solution was carried in form of a thin layer or film. The film is exposed to a high intense electric field formed between the positive rotary electrode and the ground collector and numerous unstable "Taylor cones" can be generated over the electrode surface. As the jets carrying the fiber leaves the rotating electrode, the neighboring positive charges deposited on the fiber repel against each other thereby stretching the thread further to a thinner diameter fiber. This process continues until the nanofibers reach the ground collector. The applied energy is 70 KV, the distance between the electrode and the ground collector is adjusted to 19 cm and the electrode rotating speed set to 30 Hz. Using the prepared graphene suspension for electrospinning. The resulting electrospun fibers were treated for 2 h at 450 °C to obtain the pure graphene nanofibers, in which the PVP has been burned off.

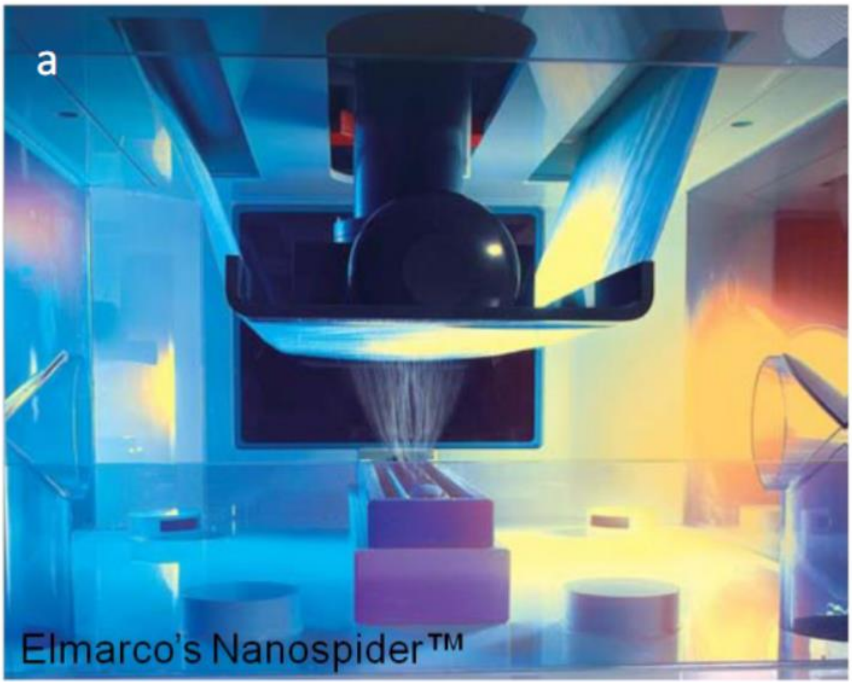

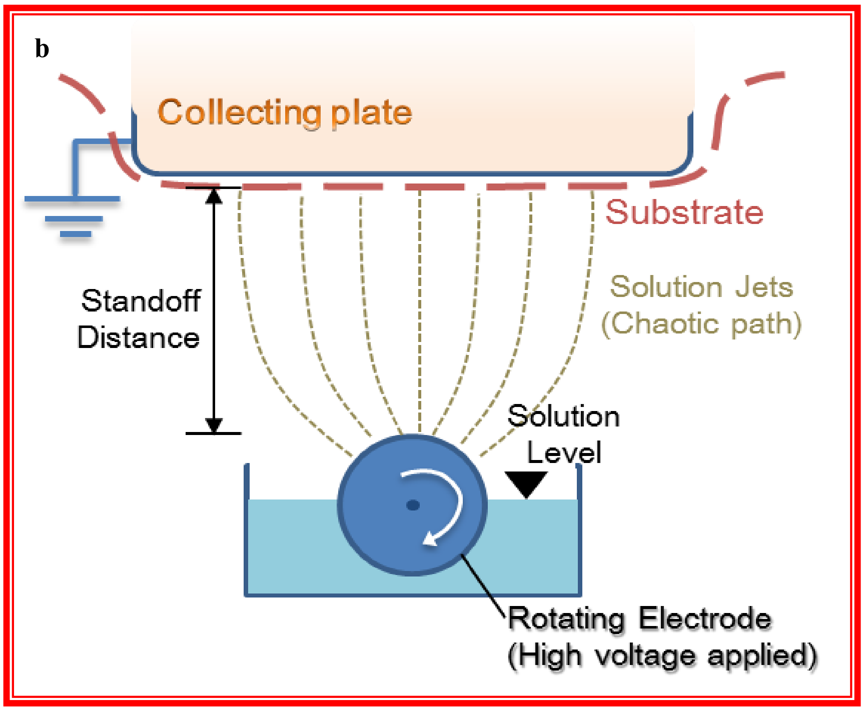

Figure 2.2. Schematic setup for nozzle-less electrospinning setup.

2.3.3 Fabrication of TiO_2 nanofibers with embedded graphene

In this part another technique needle electrospinning was used to fabricate the aligned TiO_2 nanofibers with embedded graphene (TG nanofibers). The schematic of the electrospinning set-up is shown in Figure 2.3. The solution is loaded into a syringe and fed through a flow meter pump. A high electric potential is applied to the solution, at a threshold voltage 14 KV, the repulsive force generated in the electro-active solution is greater than its surface tension and a Taylor cone is formed at tip of syringe. Due to the electrostatic forces, this droplet is further elongated. As a result, the solvent is evaporated, and the solidified nanofibers can be formed. The two discs served as parallel electrodes and a bridging effect can be realized between the two discs spaced only 7 cm apart. The orientation of the two parallel discs keep changing from horizontal to vertical position, and from vertical back to horizontal position to produce theoretically a rectangular shaped scaffold. In this case, a significant portion of nanofibers were collected across the small gap forming a structured polygon-shaped scaffold layer with uniform, pores. The precursor solution for electrospinning was prepared by mixing 4% titanium isopropoxide and 4% acetic acid with a certain amount pure graphene suspension. The resulting electrospun nanofibers on the FTO glass were treated for 2 h at 450 °C to obtain the TiO_2/graphene nanofibers scaffold.

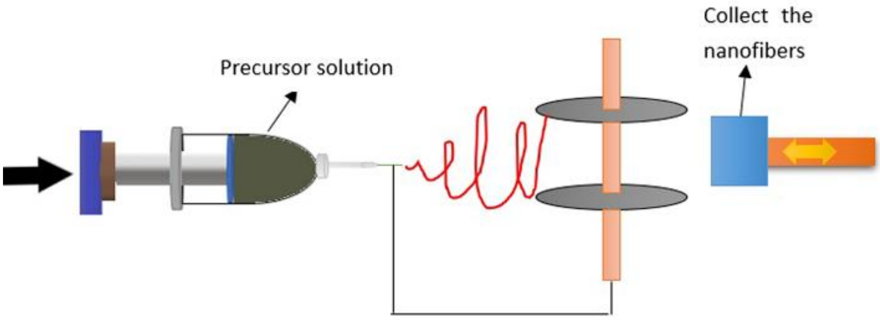

Figure 2.3. Schematic representation of the synthesis of TG nanofibers technique set-up.

2.4 Morphology and crystal structure characterization

2.4.1 Morphology characterization

The morphology of nanostructure was characterized by scanning electron microscopy (SEM). SEM uses a focused beam of high-energy electrons to generate a variety of signals at the surface of solid specimens. The signals that derive from electron-sample interactions reveal information about the sample including external morphology (texture), chemical composition, and crystalline structure and orientation of materials making up the sample. The schematic diagram of the SEM working principle is shown in Figure 2.4 [2].

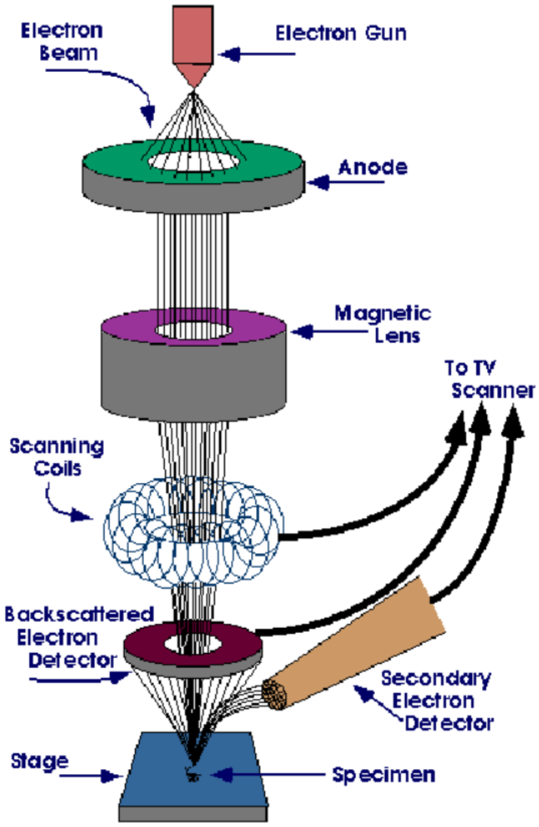

Figure 2.4. The schematic diagram of the SEM working principle [2].

A Field Emission Scanning Electron Microscope (FESEM) is microscope that works with electrons (particles with a negative charge) instead of light. These electrons are liberated by a field emission source. The object is scanned by electrons according to a zig-zag pattern. Figure 2.5 shows a schematic diagram of FESEM [2].

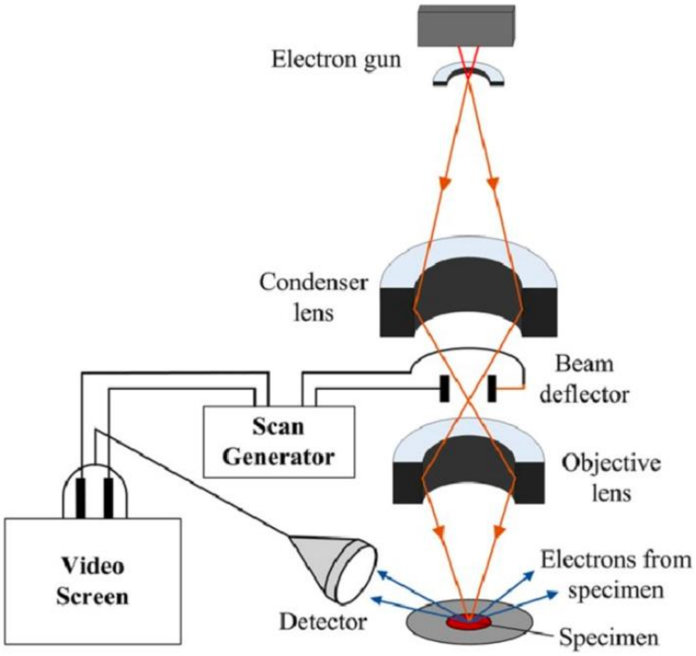

Figure 2.5. Schematic diagram of FESEM.

In this study, SEM and FESEM were performed using JEOL Model JSM-6490 and Tescan MAIA, respectively.

2.4.2 Crystal structure characterization

XRD analysis is based on constructive interference of monochromatic X-rays and a crystalline sample: The X-rays are generated by a cathode ray tube, filtered to produce monochromatic radiation, collimated to concentrate, and directed toward the sample. The interaction of the incident rays with the sample produces constructive interference (and a diffracted ray) when conditions satisfy Bragg’s Law ($n\lambda=2d \sin \theta$). This law relates the wavelength of electromagnetic radiation to the diffraction angle and the lattice spacing in a crystalline sample.

The characteristic x-ray diffraction pattern generated in a typical XRD analysis provides a unique “fingerprint” of the crystals present in the sample. When properly interpreted, by comparison with standard reference patterns and measurements, this fingerprint allows identification of the crystalline form.

The crystal forms of the PbI_2 layers and perovskite layers under different conditions were investigated by X-Ray diffraction (XRD). In this work, the XRD was performed by Rigaku 9KW Smartlab using Cu ká (λ=0.1540nm) radiation.

2.5 Spectroscopic Measurement

2.5.1 UV-visible absorption

Ultraviolet and visible (UV-Vis) absorption spectroscopy is the measurement attenuation of a beam of light after it passes through a sample or after reflection from a sample surface. Absorption can be at a single wavelength or over an extended spectral range.

In this work the absorption spectrum was measured by an Agilent Varian Cary 4000UV/VIS/NIR spectrophotometer.

2.5.2 Photoluminescence (PL) spectrum

Photoluminescence spectroscopy is a contactless, versatile, nondestructive, powerful optical method of probing the electronic structure of materials. Light is directed onto a sample, where it is absorbed and imparts excess energy into the material in a process called photo−excitation. One way this excess energy can be dissipated by the sample is through the emission of light, or luminescence. In the case of photo−excitation, this luminescence is called photoluminescence. Thus, photoluminescence is the spontaneous emission of light from a material under optical excitation. The intensity and spectral content of this photoluminescence is a direct measure of various important material properties.

Photo excitation causes electrons within the material to move into permissible excited states. When these electrons return to their equilibrium states, the excess energy is released and may include the emission of light (a radiative process) or may not (a nonradiative process). The principle of PL is shown in Figure 2.6.

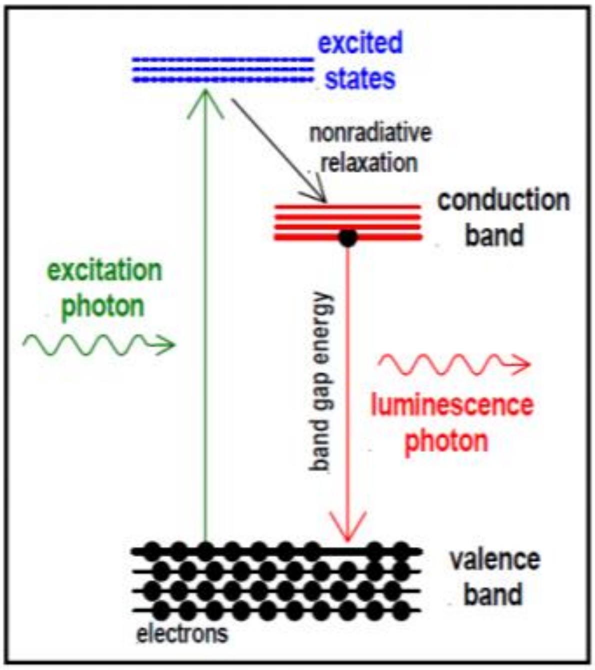

Figure 2.6. Principle of PL.

In this study, the steady-state PL measurement was carried out by using FLS920 system with a computer controlled spectrofluorimeter in the UV–NIR spectral range with single photon counting sensitivity. The PL was excited under 600 nm xenon lamp and the samples were prepared on the quartz substrate.

2.5.3 Time-Resolved Photoluminescence (TRPL) Spectroscopy

TRPL is an experimental technique that provides the spectral and temporal evolution of the emission of a sample following its illumination by a short pulse of light. More precisely, the short pulse of light generates electron-hole pairs that decay to lower energy levels of the sample. These electron-hole pairs can subsequently recombine and emit light. The emitted light is composed of a set of wavelengths corresponding to transition energies of the sample and, as a result, the measurement of the optical spectrum as a function of time provides a means to measure the transition energies and their lifetimes. Most experiments excite the sample with a pulsed laser source and detect the PL with a photodiode, streak camera, or photomultiplier tube (PMT) set up for up-conversion or single-photon counting.

In this work, TRPL decay profile were obtained using an Edinburgh time-correlated single-photon-counting system. The TRPL signal in photoexcited state was measured by using a 337-nm laser. The samples were prepared on quartz substrate.

2.5.4 Raman spectrum

Raman spectroscopy is a scattering technique. In Raman spectroscopy, sample is illuminated with a monochromatic laser beam which interacts with the molecules of sample and originates a scattered light. The scattered light having a frequency different from that of incident light (inelastic scattering) is used to construct a Raman spectrum. Raman spectra arise due to inelastic collision between incident monochromatic radiation and molecules of sample. When a monochromatic radiation strikes at sample, it scatters in all directions after its interaction with sample molecules. Much of this scattered radiation has a frequency which is equal to frequency of incident radiation and constitutes Rayleigh scattering. Only a small fraction of scattered radiation has a frequency different from frequency of incident radiation and constitutes Raman scattering. When the frequency of incident radiation is higher than frequency of scattered radiation, Stokes lines appear in Raman spectrum. But when the frequency of incident radiation is lower than frequency of scattered radiation, anti-Stokes lines appear in Raman spectrum. Scattered radiation is usually measured at right angle to incident radiation [3].

In this study, LabRAM HR 800 Raman Spectrometer was used to analyze the pure graphene nanofibers and TG nanofibers.

2.6 Thermal behavior

Thermal gravimetric analysis (TGA) is a method of thermal analysis in which changes in physical and chemical properties of materials are measured as a function of increasing temperature (with constant heating rate), or as a function of time (with constant temperature and/or constant mass loss).

Changes in the mass of a sample due to various thermal events (desorption, absorption, sublimation, vaporization, oxidation, reduction and decomposition) are studied while the sample is subjected to a program of change in temperature. Therefore, it is used in the analysis of volatile products, gaseous products lost during the reaction in thermoplastics, thermosets, elastomers, composites, films, fibers, coatings, paints, etc.

The thermal decomposition behavior of TG nanofibers in this work was examined using a thermo gravimetric analyzer and differential scanning calorimeter (TGA–DSC) (Mettler Toledo) under ambient pressure in the temperature range between 30 and 1000 °C at a controlled heating rate of 20 °C min^{-1}.

2.7 Photovoltaic characterization and analysis

2.7.1 The solar radiation and air mass

Solar radiation closely matches a black body radiator at about 5,250 °C. As it passes through the atmosphere, sunlight is attenuated by scattering and absorption; the more atmosphere through which it passes, the greater the attenuation. The attenuation is described by the “Air Mass” factor since the absorption increases with the mass of air through which the radiation passes. l_0 is the thickness of the atmosphere, the path length l through the atmosphere for radiation at an incident angle α relative to the normal to the earth’s surface is described by

$$l = \frac{l_0}{\cos \alpha} \tag{2.1}$$

The ratio of l/l0 is the Air Mass factor. The spectrums outside the atmosphere and on the surface of the earth for perpendicular are expressed as AM0 and AM1, respectively. AM1.5 is the standard spectrum for moderate weather which means a solar incident angle of 48° corresponds to the surface normal and gives an average irradiance of 1,000 W m-2. Figure 2.7 shows the comparison for the spectrum of 5,250 °C blackbody spectrum, sunlight at top of the atmosphere (AM0) and radiation at sea level (AM1.5).

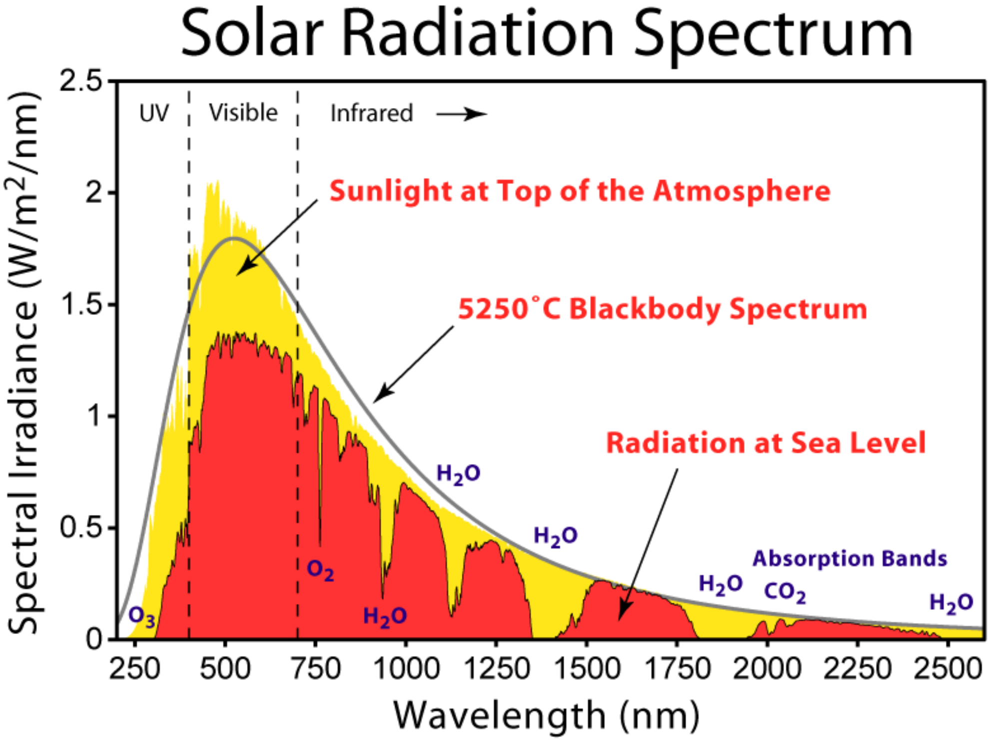

Figure 2.7. Comparison for the spectrum of 5,250 °C blackbody spectrum, sunlight at top of the atmosphere and radiation at sea level [4].

2.7.2 Photovoltaic Current-Voltage Characterization

Standard current-voltage (I-V) measurement determines the current voltage response of the device for the PSC. In the dark condition, under applied voltage, a current flow in the opposite direction to that of the photocurrent can be generated in the device. This reverse current is regarded as the dark current. For an ideal diode, the dark current, I_{dark}, can be expressed by Eq. 2.2.

$$I_{dark} = I_s \left(e^{qv/K_BT} - 1\right) \tag{2.2}$$

Where I_s is the saturation current of the diode (typically 10^{-7}-10^{-9} A), V is the voltage applied on the terminals of the device and q is the electronic charge.

Under illumination condition, the I-V characteristics can be shown as following:

$$I = I_{ph} - I_{dark} = I_{ph} - I_s\left(e^{qv/K_BT} - 1\right) = I_{ph} - I_s(e^{V/V_T} - 1) \qquad (2.3)$$

Where I_{ph} is the photocurrent which depends on the light intensity and V_T is referred to as the thermal voltage that equals k_BT/q. For non-ideal devices, the weak dependence of dark current on voltage can be modified by an ideality factor m.

$$I = I_{ph} - I_s(e^{V/mV_T} - 1) \qquad (2.4)$$

The typical I-V curve is shown in Figure. 2.8.

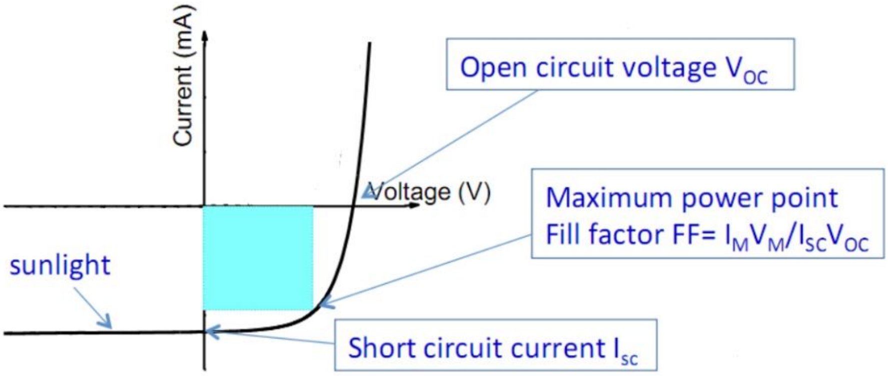

Figure 2.8. Typical I-V curve.

In this study, photocurrent–voltage measurements were measured using a Keithley 2400 digital source meter with a scan rate of 0.22 V·s^{-1} under illumination of AM1.5G 100 mW·cm^{-2} from a solar simulator ABET SUN 2000. The comparison between the solar simulator (ABET SUN 2000) spectrum and the standard AM1.5G is shown in Figure 2.9.

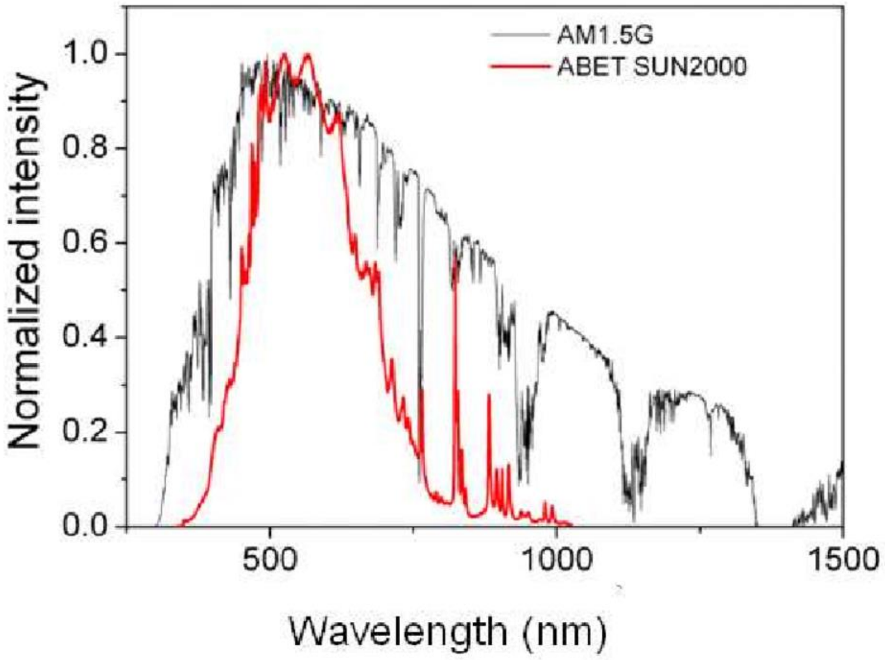

Figure 2.9. Comparison of the solar simulator (ABET SUN 2000) spectrum and the standard AM1.5G.

2.7.2.1 Short-circuit current (I_{sc})

I_{sc} is measured when the applied voltage equals zero.

$$I_{sc} = I_{ph} \tag{2.5}$$

Eq. 2.5 reveals that I_{sc} depends on the photocurrent and the light intensity.

2.7.2.2 Open-circuit voltage (V_{oc})

V_{oc} is measured under the open circuit condition, there is no external current flow between the two terminals of the device. V_{oc} depends on the temperature and light intensity.

2.7.2.3 Fill Factor (FF)

The power can be expressed by the area of the rectangle with width V and height I in Figure 2.8. Along the I-V curve in Figure 2.8, the maximum area can be determined corresponding to the maximum power point. At this point, the device generates the highest power output with the voltage (V_m) and current (I_m). FF is defined as the ratio

$$\mathrm{FF} = \frac{V_m I_m}{V_{oc} I_{sc}} \tag{2.6}$$

2.7.2.4 Power conversion efficiency (PCE)

PCE of the device is one of the most important parameters to represent the performance of the device. It is defined as the ratio of the maximum power output (P_{max}) to the power of the incident sunlight (P_{in}).

$$\mathrm{PCE} = \frac{V_m I_m}{P_{in}} = \frac{V_{oc} I_{sc} FF}{P_{in}} \tag{2.7}$$

2.7.3 External Quantum Efficiency (EQE)

EQE is the ratio of the number of charge carriers collected by the solar cell to the number of photons of a given energy irradiated on the solar cell (incident photons).

$$\mathrm{EQE} = \frac{electrons}{photons} \tag{2.8}$$

EQE depends on both the absorption of photons and collection of charge carriers, it can be used to characterize the charge collection efficiency of photovoltaic devices.

In this work, EQE was tested with an EQE system equipped with a xenon lamp (Oriel66902, 300W), a monochromator (Newport66902), a Si detector (Oriel 76175_71580), and a dual-channel power meter (Newport2931_C).

2.7.4 Intensity-modulated photocurrent spectroscopies (IMPS)

IMPS is determined in the frequency domain by means of a light source, which is modulated in intensity over a broad frequency range. It measures the modulated photocurrent response to the modulation of illumination light intensity at short-circuit condition. The principle is shown in Figure 2.10. Modulation of the light P as force, illuminating an electrochemical cell C. The quotient of one electric magnitude (current potentiostatic, or voltage galvanostatic or at OCP) with the dynamic light intensity P* leads to the IMPS spectrum H*.

The remaining magnitudes (for instance voltage or current) has to be kept, until the transfer function record is completed. After that, they may be swept.

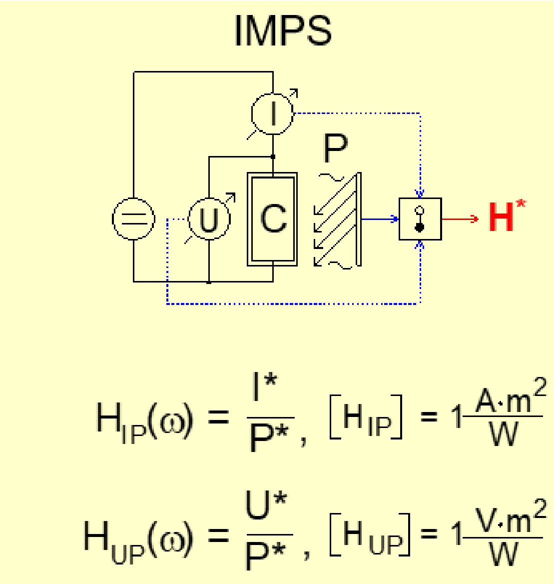

Figure 2.10. Principle of IMPS.

In this study, IMPS was carried out using Zahner CIMPS photo-electrochemical workstation. The illumination for the frequency response techniques was provided by a white light LED over a wide range of dc light intensities. The amplitude of the sinusoidal modulation for IMPS measurements was checked to obtain a linear response.

References

1. Paton, K. R., et al. *Scalable production of large quantities of defect-free few-layer graphene by shear exfoliation in liquids.* Nat. Mater. 2014. **13**: p. 624.

2. Liu. J. L., et al. *Self-assembly od nano/micro-structured Fe3O4 microspheres among 3D rGO/CNTs hierarchical networks with superior lithium storage performance.* Nanotechnology, 2014. **25**: p. 185705.

3. Bumbrah, G. S., Sharma, R. M. Raman spectroscopy – Basic principle, instrumentation and selected applications for the characterization of drugs of abuse. Egyptian Journal of Forensic Sciences,Egyptian Journal of Forensic Sciences. 2016. **6**: p. 209.

4. Solar energy. 2015; Available from http://www.newlifepost.com/archives/71759.html.

Chapter 3

Conditioning lead iodide with DMSO and HCl to control crystal growth improving performance of perovskite solar cell

3.1 Introduction

Improving film surface coverage and grain size is an efficient and cost-effective way to improve the performance of the planar structured perovskite solar cell. Employing additives, such as HCl or HI acid [1-3] and Dimethyl Sulfoxide (DMSO) or N-methyl-2-pyrrolidone (NMP) [4-10], have been used to retard perovskite crystallization and improve surface coverage. Yang et al. applied direct intramolecular exchange of DMSO molecules intercalated in PbI_2 with Formamidinium Iodide (FAI) to improve the $FAPbI_3$ crystallization, the PCE of the solar cell is over 20% [4]. Yang et al. incorporated HCl into PbI_2 precursor solution and the solar cell exhibited cell efficiency around 15.2% [1]. Jeon et al. used a one-step method to deposit the $MAPb(I_{1-x}Br_x)_3$ perovskite layer by using gamma-butyrolactone (GBL) and DMSO as effective solvents which enabled a perovskite solar cell with a power conversion efficiency of 16.2% [8]. Despite of these efforts, the $MAPbI_3$ crystallization by the direct intra-molecular exchange of DMSO molecules intercalated in PbI_2 with MAI to achieve larger crystals, in combination with using hydrochloric acid to slow-down crystal growth to yield more uniform crystals have not yet been investigated. Some interesting unanswered questions remain. First, would the use of both HCl and DMSO directly impact negatively on the formation of the perovskite layer? Second, when both additives are indeed working synergistically, what are the tangible benefits in terms of characteristics (including morphology) and device performance? Third, does the chloride addition improve the stability of the device against moisture and strong solar irradiation? This chapter will address these three aspects.

In this chapter, a systematic investigation on the effect of individual DMSO addition, and combined HCl and DMSO addition on perovskite morphology and device performance of the solar cell has been carried out. A novel simple two-step method of incorporating HCl into $PbI_2(DMSO)_x$ precursor solution with capacities for molecular exchange with MAI during the spinning process is used, with objective of improving crystal size, crystallinity, and uniform coverage of the perovskite thin film on the dense TiO_2 layer. This also prevents the negative effects on direct chemical reaction between Cl and DMSO. Using this approach highly efficient $MAPbI_3$ based PSCs have been fabricated with PCEs reaching 17.8% under AM1.5G standard solar simulation with excellent device stability under room temperature. Here, the stability of the devices has also been investigated. We find that the addition of HCl in the $PbI_2(DMSO)_x$ precursor solution to form the perovskite layer can also improve the stability of the devices.

3.2 Experimental Details

3.2.1 Preparation of the substrate and compact layer

Patterned FTO on glass substrates were cleaned sequentially by ultra-sonication in soap water, deionized water, acetone and isopropanol, and subsequently exposed to UV-ozone for 15 min prior to the spin-coating step. A compact TiO_2 layer was spin-coated on the substrates by using a 0.15 M titanium iso-propoxide (TIP) ethanol solution at a speed of 3000 rpm for 30 s. The samples were subsequently calcinated at 450 °C for 2 h. Subsequently, the samples were immersed in 60 mM of $TiCl_4$ solution for 30 min at 70 °C.

3.2.2 Synthesis of $PbI_2(DMSO)_x$ complex

To synthesize the PbI_2-$(DMSO)_x$ complex, first 0.5 M PbI_2 was dissolved in 15 mL

DMSO at 60 ℃ and subsequently 35 mL toluene was slowly added into the PbI_2 solution. Subsequently, the produced white precipitation was filtered and dried for 1 h at room temperature. The $PbI_2(DMSO)_x$ complex was obtained by annealing for at least 24 h in vacuum oven at 60 °C.

3.2.3 The fabrication of perovskite layer, hole transport layer and electrodes

1.2 M $PbI_2(DMSO)_x$ complex was introduced to DMF solution with 2.5 vol% HCl additive. The resultant solution was deposited on the TiO_2 dense layer coated substrate at 3000 rpm for 30 s. Subsequently, 400mM CH_3NH_3I in isopropanol was spin-coated at 5000 rpm for 30 s. Next, a rinsing step with 2-propanol was carried out to remove the excess organic fraction. Finally, the resulting sample was annealed at 150 °C for 20 min. In a control experiment or comparison, 1.2 M $PbI_2(DMSO)_x$ complex was introduced to DMF solution without HCl additive and subsequently deposited on the TiO_2 dense layer. The remaining procedures were similar as with the one with HCl additive.

A precursor solution was prepared by dissolving 79 mg of spiro-MeOTAD, 28.8 μL of 4-tert-butylpyridine, 17.5 μL of 520 mg • mL^{-1} lithium bis(trifluoromethylsulfonyl)imide in acetonitrile in 0.99 mL of chorobenzene. The solution was spin-coated at 4000 rpm for 30 s on the perovskite layer to form a hole transport layer (HTL). Finally, the electrodes (MoO_3 (15 nm)/Al (120 nm)) were deposited by thermal evaporation through a shadow mask with effective area approximately 0.1 cm^2. The final device structure is depicted in Figure 3.1.

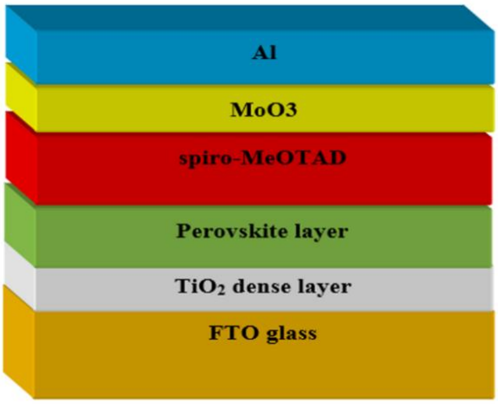

Figure 3.1. Device configuration.

3.3 Results and Discussion

3.3.1 Investigation of the morphology and crystal structure of perovskite layer

Figure 3.2 shows the SEM images of the perovskite layer formed by different methods. The morphology of the perovskite layers formed by using both DMSO and HCl and using only DMSO is shown in Figure 3.2(a) and (b), respectively. Comparing the two images we can see that using both DMSO and HCl can help to form more uniform and larger crystals with less interfaces and boundaries. During the conversion from PbI_2-DMSO-MAI to $MAPbI_3$, the DMSO molecules intercalated in PbI_2 can be easily replaced with MAI, leaving a homogeneous, flat layer with large sized perovskite crystals of over one micron. The role of DMSO in the MAI–PbI_2–DMSO phase is to retard the rapid reaction between PbI_2 and MAI during the evaporation of solvent in the spin-coating process to allow formation of larger crystals with less interfaces and boundaries [4]. Additionally, by using the HCl additive, the crystal growth rate can be further slowed down to achieve more uniform crystals. Meanwhile, after adding HCl into the precursor solution, the ratio of DMSO may be reduced, as excess DMSO may give rise to an inhomogeneous film with pinholes [11]. The Cl^- icons can be immediately removed from the $HCl\cdot PbI_2(DMSO)_x$ film and the precursor film is then converted into $MAPbI_3$ perovskite and PbI_2 [12], as such, the Cl composition cannot be detected by EDS. This is ideal for providing homogeneous coverage on the dense layer without pinholes that provides short-circuiting and recombination sites. With application of DMSO, it can be noted that after adding HCl to the PbI$_2$(DMSO)$_x$ and MAI, the perovskite film in the present approach as shown in Figure 3.2(a) does not have any pinholes while in the conventional approach, Figure 3.2(b), the film has many pinholes. On the other hand, it can also be seen from Figure 3.2(b) that due to the application of DMSO, the crystal size increased dramatically as compared with Figure 3.2(c) which is the perovskite film generated by PbI$_2$ solution with HCl additive reacted with MAI.

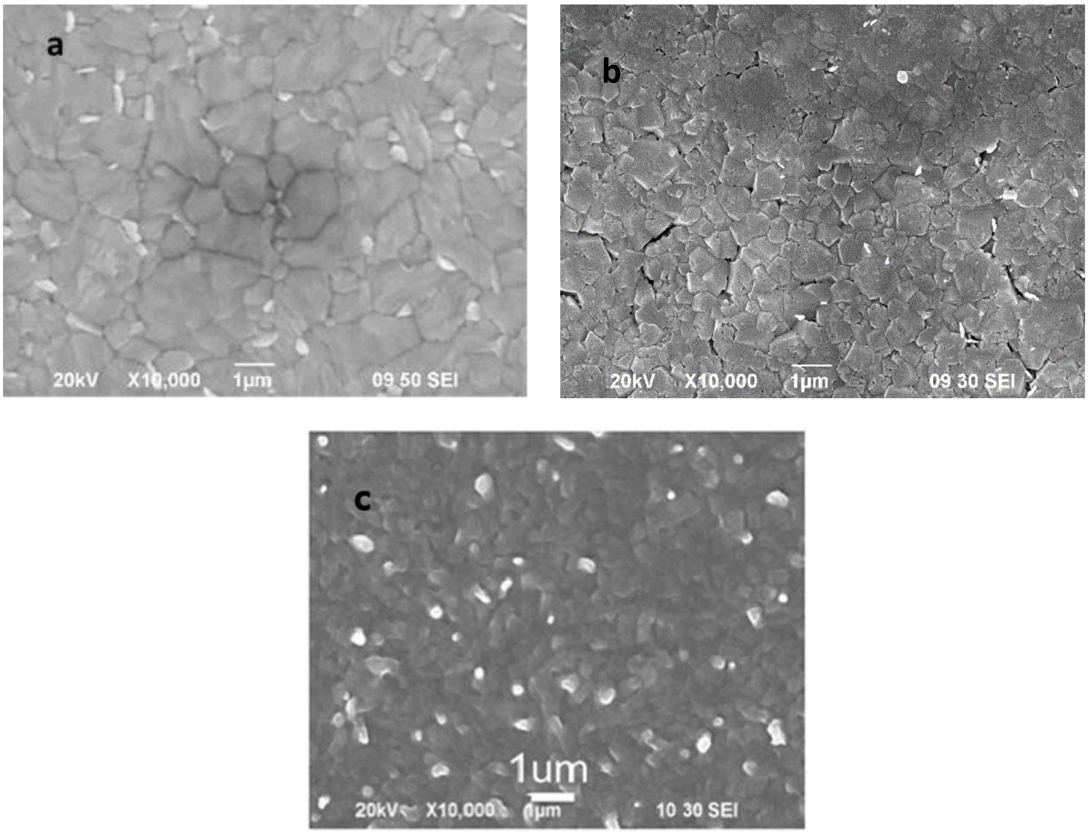

Figure 3.2. (a) perovskite layer formed by PbI2(DMSO)x solution with HCl additive and MAI; (b) perovskite layer formed by PbI2(DMSO)x solution and MAI; (c) perovskite layer formed by PbI2 solution with HCl additive and MAI.

In fact, PbI$_2$(DMSO)$_x$ in DMF solution with HCl additive can effectively retard the crystallization rate which facilitates enhanced homogeneous nucleation and uniform crystal growth of the PbI$_2$ thin film. The little amount of Cl in precursor solution can further enhance crystallinity of the resulting perovskite films with preferred {110} orientation, despite the amount of Cl is negligible.[13] The XRD patterns of $PbI_2(DMSO)x$ thin film with and without HCl additives, and PbI_2 thin film with and without HCl additives are shown in Figure 3.3(a), respectively. The XRD patterns are exactly consistent with PbI_2 peaks at 12.6°, and by using DMSO, the $PbI_2(DMSO)$ complex peak can be observed in Fig. 3a at around 9.7° and 25.7°. The use of DMSO caused the intensities of PbI_2 diffraction peaks to be quenched. Through the XRD pattern of $PbI_2(DMSO)_x$ with HCl, it can be noted that the area of PbI_2 peak (139792) is higher when compared with that of $PbI_2(DMSO)_x$ (95685), this may be due to the decrease of DMSO ratio in the precursor solution, but from Figure 3.2(a)-(b) it can be assured that this ratio is the best for the morphology of the perovskite layer. Figure 3.3(b) compares the solution-processed perovskite thin films, including (i) pristine perovskite (base case), (ii) the perovskite with HCl added, (iii) the perovskite formed by $PbI_2(DMSO)_x$ and MAI, and (iv) our presently investigated configuration – the perovskite formed by $PbI_2(DMSO)_x$ with HCl and MAI. The areas of the main peak (110) of $CH_3NH_3PbI_3$ in Figure 3.3(b) (i)-(iv) are 7438, 8846, 14909 and 18065 respectively, there is a remarkable increase after introducing HCl into the $PbI_2(DMSO)_x$ solution. Therefore, the use of HCl certainly improves the crystallinity of the perovskite layer. Table 3.1(a) shows the full width at half maximum (FWHM) of the (110) peak corresponding to the different perovskite layers. It can be seen that the perovskite layer formed by $PbI_2(DMSO)_x$ with HCl and MAI has the smallest FWHM(0.09°), which further confirms the results of Figure 3.3(b) that the perovskite layer has the largest grain size.

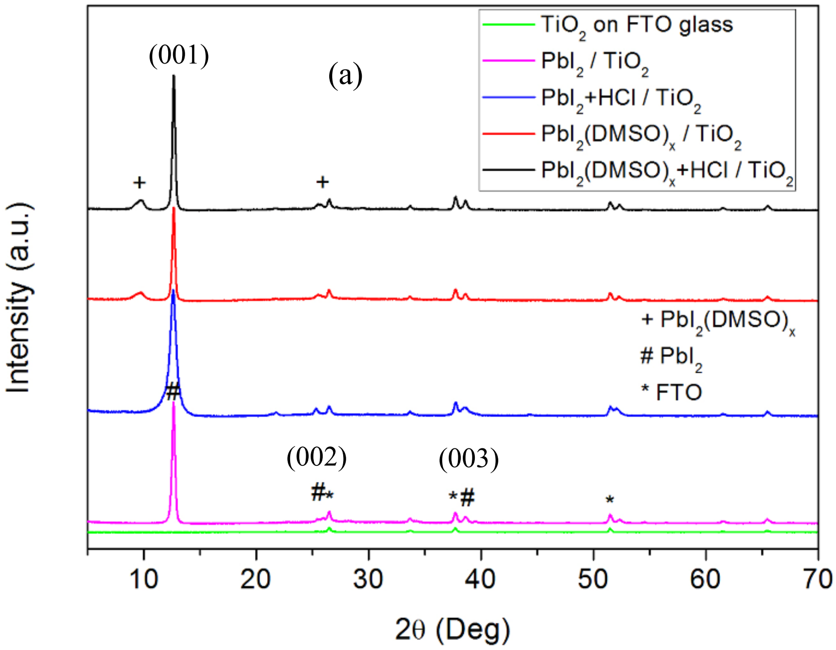

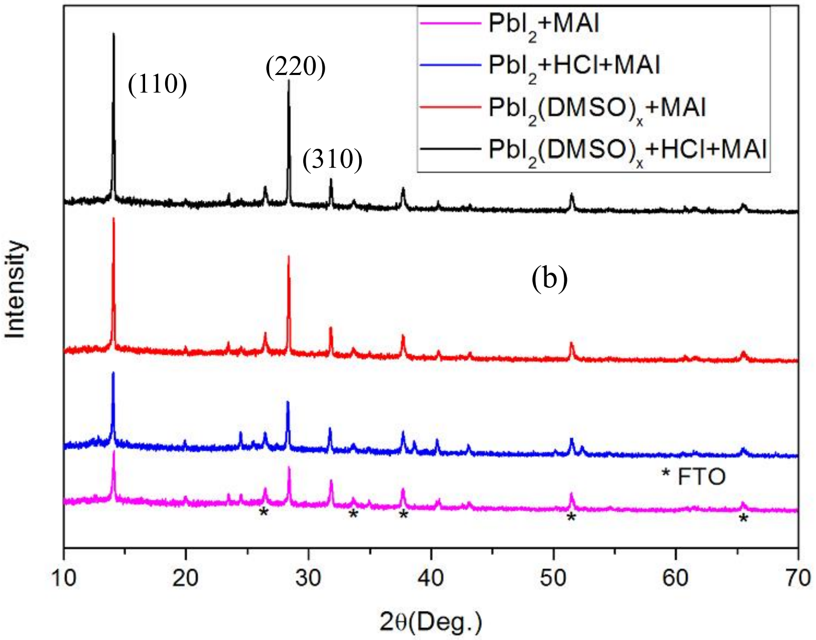

Figure 3.3. (a) XRD patterns of PbI_2 thin film, PbI_2 with HCl thin film, $PbI_2(DMSO)_x$ thin film and $PbI_2(DMSO)_x$ with HCl thin film on the TiO_2 dense layer coated on FTO glass; (b) XRD patterns of pristine perovskite, the perovskite with HCl added, the perovskite formed by $PbI_2(DMSO)_x$ and MAI, and the perovskite formed by

$PbI_2(DMSO)_x$ with HCl and MAI.

Table 3.1(a). The full width at half maximum of (110) peak of the perovskite layer

	PbI_2+MAI	PbI_2+HCl +MAI	$PbI_2(DMSO)_x$ +MAI	$PbI_2(DMSO)_x$ +HCl+MAI
FWHM	0.174°	0.142°	0.131°	0.124°

Table 3.1(b). The full width at half maximum of (001) peak of the PbI_2 layer

	PbI_2	PbI_2+HCl	$PbI_2(DMSO)_x$	$PbI_2(DMSO)_x$ +HCl
FWHM	0.312°	0.579°	0.288°	0.292°

3.3.2 Photovoltaic performance

The best performance on current density−voltage (i.e. J−V curves) characteristics of the aforementioned devices is shown in Figure 3.4(a). As can be seen, the J-V curve is highest for the device with adding both DMSO and HCl, followed by adding only DMSO, and lastly adding only HCl. The HCl perovskite cell provides higher V_{oc} and J_{sc} while the DMSO perovskite cell provides higher fill factor (FF). The combination as demonstrated in this study provides synergistic advantages in all three parameters - V_{oc}, J_{sc} and FF. To quantify the performance, the best and average performance parameters are listed in Table 3.2(a) and 3.2(b), respectively. The device prepared using both DMSO and HCl had the maximum efficiency of 17.8%, exhibiting J_{sc} of 23.24 $mA\cdot cm^{-2}$, V_{oc} of 1.05V, and FF of 73%. Interestingly, Jeon et al. [8] used GBL, DMSO and N-methyl-2-pyrrolidone as effective solvents to deposit the $MAPb(I_{1-x}Br_x)_3$ perovskite layer; the resultant device has achieved PCE of 16.2%. This result is indeed comparable to ours in using only DMSO to fabricate the perovskite solar cells for which the best performance of our device is 16.1%, see Table 3.2(a). This provides a good benchmark of our results with those in the literature. Further, two interesting conclusions can be drawn from the present study. For the device with DMSO, the additional treatment of using HCl provides a 10%-11% improvement in the PCE for either the best performance (Table 3.2(a)) as well as the average performance (Table 3.2(b)) when compared to the case without. Compared with the device with only HCl treatment, the use of DMSO and HCl in the device improved 17% for the best performance (Table 3.2(a)). The improved thin-film quality by using both DMSO and HCl generated a significant synergistic enhancement in performance, facilitating larger crystals, superior crystal quality (crystallinity), and uniform coverage on the TiO_2 dense layer. The J_{sc} obtained by EQE has been shown in Table 3.2(a). It can be seen that the J_{sc} acquired by the density−voltage (i.e. J−V curves) characteristics is different from that obtained by EQE test. This is mainly due to the error in the calibration of the equipment for the EQE test. The effect of different concentration HCl also has been studied. From Figure 3.4(b) we can see that 2.5 vol% HCl is best condition. If the concentration is too high this may cause inhomogeneous nucleation which do not benefit the performance of the devices. Under this optimal condition, energy harvesting is maximized while short-circuiting is minimized. Fig. 3.5 (a), (b) show the J-V curves in reverse and forward sweeps for the perovskite layers with and without TG nanofibers, respectively. It can be seen that the use of TG nanofibers scaffold for the device further facilitates reduction in the hysteresis, which is advantageous.

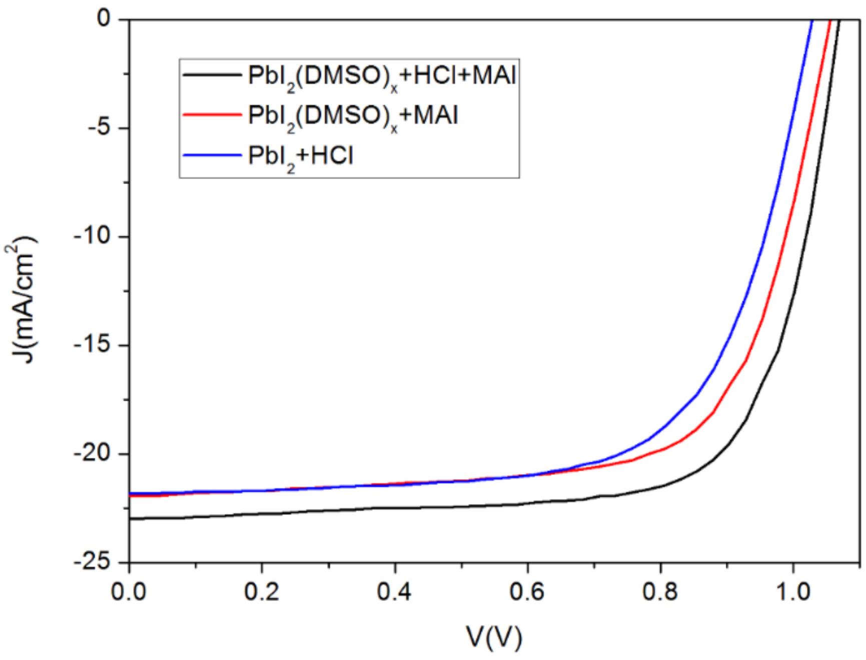

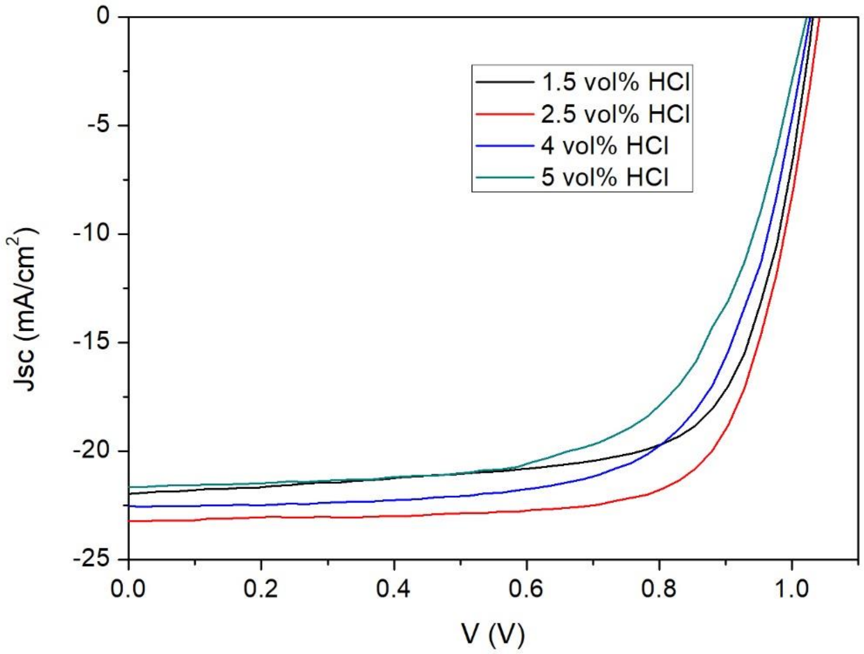

Figure 3.4. (a) J−V curves measured under 100 mW·cm$^{−2}$ AM1.5G illumination. (b) J-V curves of the devices fabricated by using different concentration of HCl.

Table 3.2(a). Best performance of the Perovskite Solar Cells under AM 1.5 G illumination

	V_{oc}/V	J_{sc}/mA•cm^{-2}	FF/%	PCE/%	Jsc/mA•cm^{-2} Obtained by EQE
$PbI_2(DMSO)_x$ +HCl +MAI	1.05	23.24	73	17.8	20.23
$PbI_2(DMSO)_x$ +MAI	1.03	21.50	73	16.1	19.09
PbI_2+HCl +MAI	1.05	22.71	64	15.2	17.78

Table 3.2(b). Average performance of the Perovskite Solar Cells

	V_{oc}/V	J_{sc}/mA•cm^{-2}	FF/%	PCE/%
MAI+$PbI_2(DMSO)_x$+HCl	1.05+/-0.2	22.8+/-0.4	70+/-1	16.6+/-0.4
MAI+ $PbI_2(DMSO)_x$	1.02+/-0.2	22.4+/-0.7	66+/-3	15.1+/-0.4
MAI+PbI_2+HCl	1.02+/-0.2	21.5+/-0.6	58+/-2	14+/-0.8

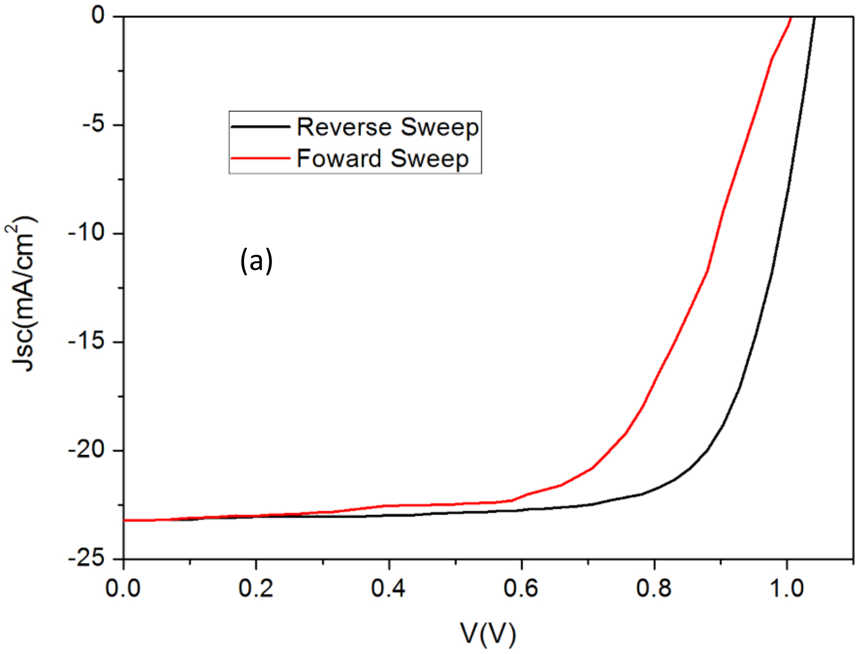

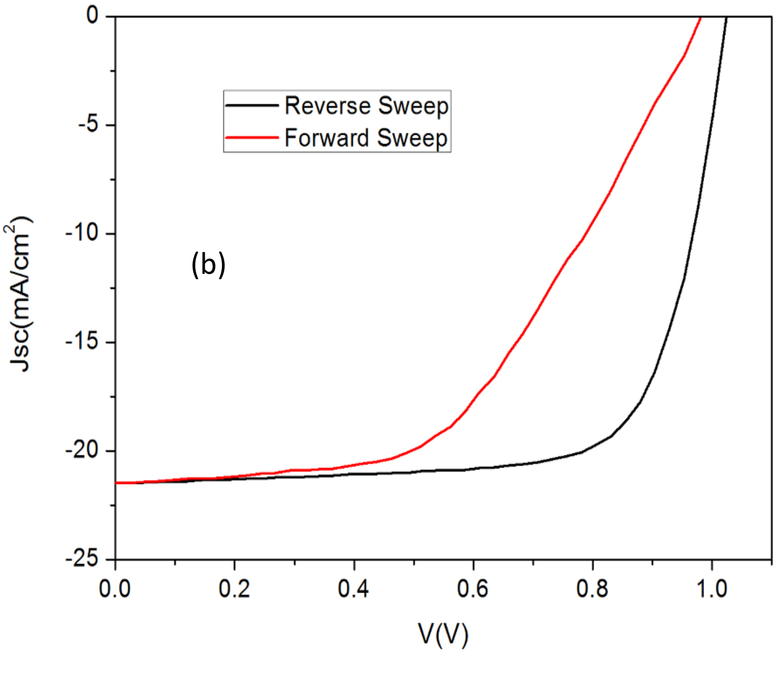

Figure 3.5. J-V curves in reverse and forward sweep. (a) perovskite layer formed by $PbI_2(DMSO)_x$ solution with HCl additive and MAI; (b) perovskite layer formed by $PbI_2(DMSO)_x$ and MAI.

Figure 3.6 shows the external quantum efficiency (EQE) of the three different types of solar cells. It can be seen that the use of DMSO and HCl further improve the performance of EQE especially at wavelengths less than 750nm. This is consistent with the increased absorbance as shown in Figure 3.7 in that improved crystallinity from slow crystallization using HCl can better harvest light in both visible and UV light ranges.

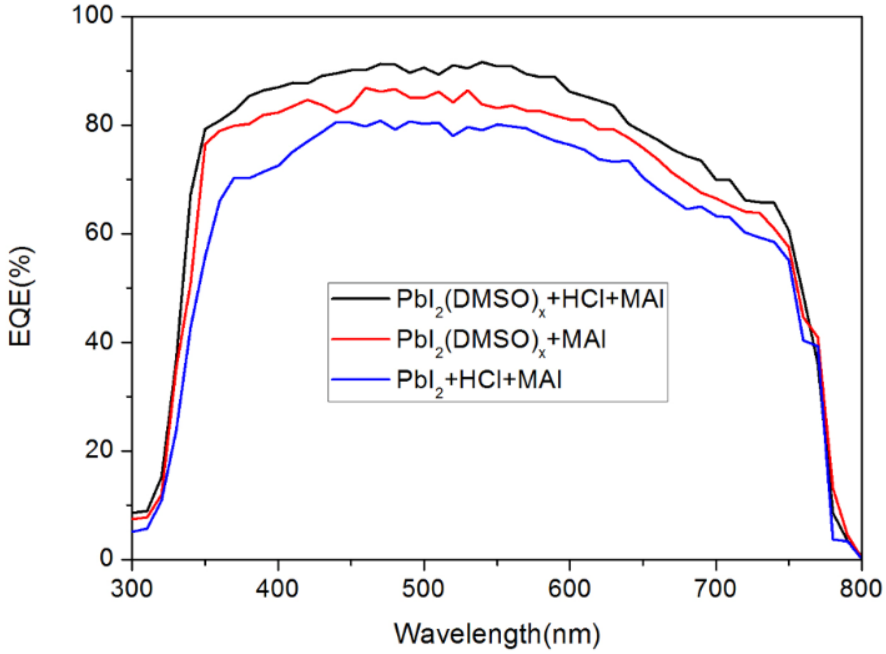

Figure 3.6. External quantum efficiency.

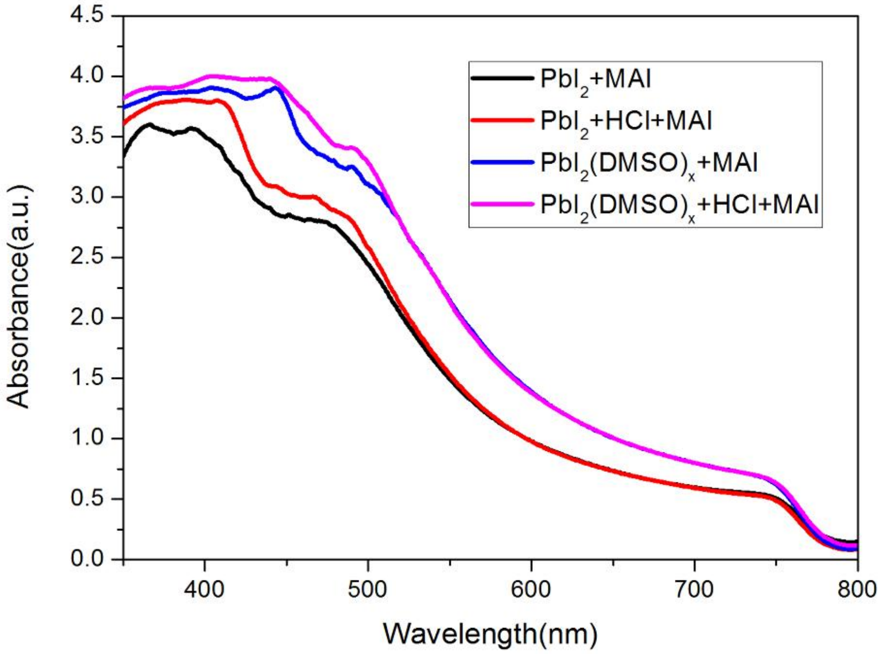

Figure 3.7. UV−vis Absorbance Spectra

The charge transport time in the solar cells was investigated by IMPS. Figure 3.8 shows the typical Nyquist plots of IMPS response curves for the solar cells with the perovskite layers formed by $PbI_2(DMSO)_x$ + HCl + MAI and $PbI_2(DMSO)_x$ + MAI, respectively. The charge transport time can be estimated from the expression: D = $1/2\pi f_{\text{min IMPS}}$ (Peter et al., 2000), where $f_{\text{min IMPS}}$ is the characteristic frequency at the minimum of the IMPS imaginary component curve. For the device with DMSO, a relatively faster charge transport time can be realized for the device that has the HCl additive. Due to the film thickness of the two types of devices being comparable, the faster charge transport time infers that the device should have a higher electron diffusion coefficient (determined to be 14% higher) as compared to the one without acid treatment (under 1000 Wm^{-2} light intensity), this can be revealed in Table 3.3. As a result, the addition of HCl in the device with DMSO with more uniform crystals further improves the charge transport property in the device. This is also supported by the higher average J_{sc} as shown in Table 3.2 (a), (b), and the reduced recombination (measured by higher FF) as shown in Figure 3.4.

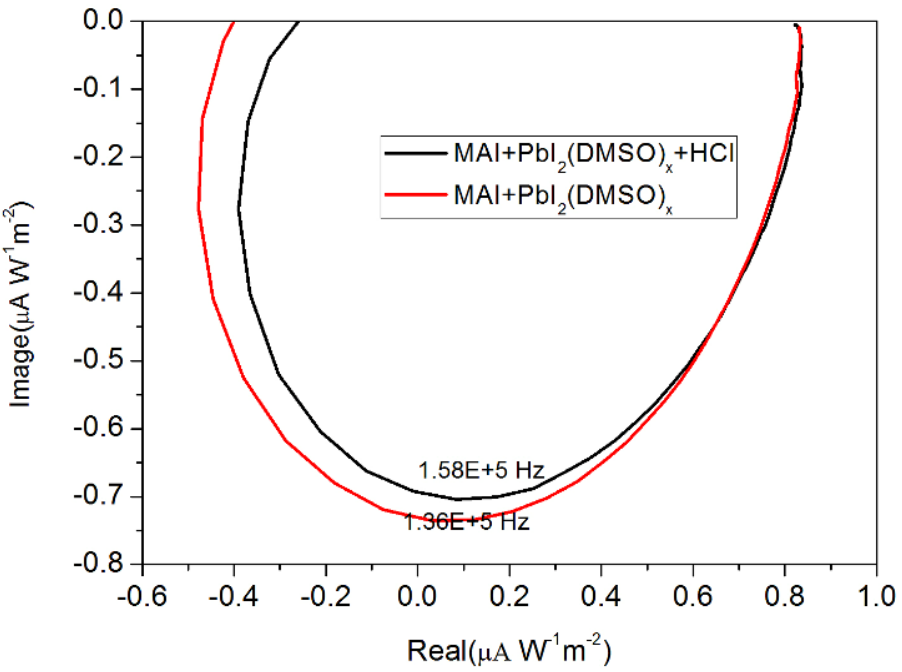

Figure 3.8. Typical IMPS response of different types of perovskite solar cell.

Table 3.3. The electron transport time with respect to the PCE of the devices

	charge transport time (μs)	PCE (%)
$PbI_2(DMSO)_x$+HCl+MAI	1.01	17.8
$PbI_2(DMSO)_x$ +MAI	1.17	16.1

3.3.3 Stability test

The introducing of HCl can help to improve the stability of $CH_3NH_3PbI_3$, this may be due to the larger electron negativity of chloride as compared to that of iodide, it strengthens the metal-halogen bond and keeps the material more stable [13,14]. The devices with encapsulation were tested in different humidity (55 RH% and 85 RH%). The time for the stability test is not irradiation time in the entire period but at three different times, initially, in middle and final time. So the time scale refers to the storage time and not irradiation time. For the first condition, under the relative humidity of 85 RH% and room temperature, the performance of the device, fabricated by using $PbI_2(DMSO)_x$ with HCl and MAI, decreases by 11% after 150 h and by 23% after 300 h. Whereas, the $PbI_2(DMSO)_x$ device without HCl added decreases by 20% and 49%, respectively, for the same period. For the second condition, under the intensity of white LED light similar as the intensity of sunlight at noon at 50 °C, the device for $PbI_2(DMSO)_x$ with HCl additive, decreases by 11% after 24 h and by 19% after 48 h, while the $PbI_2(DMSO)_x$ without HCl device decreases by 16% and 30%, respectively, for the same period. The trend of the performance changed with the time at 85%RH and under white LED light at 50 °C can be seen in Figure 3.9 (a) and (b), respectively. From the insert pictures in Figure 3.9 (a) and (b) we can see that the device for $PbI_2(DMSO)_x$ with HCl additive has a lower slope during the entire period of the stability testing as compared to the case of $PbI_2(DMSO)_x$ without HCl in both conditions. From discussion we can see that the devices with HCl have better stability under high humidity, strong solar irradiation, and elevated temperature. Table 3.4 shows the changes of the PCE in the stability test.

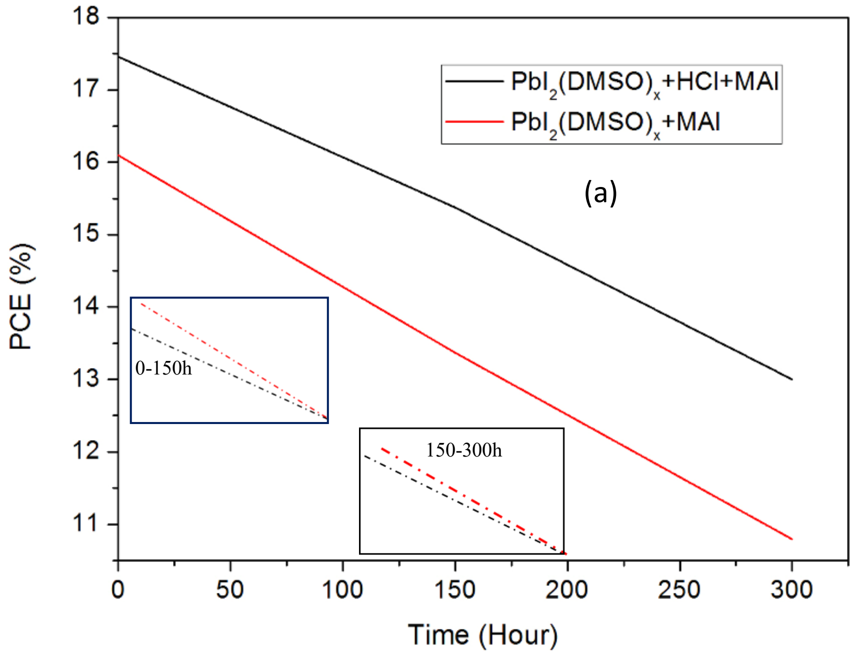

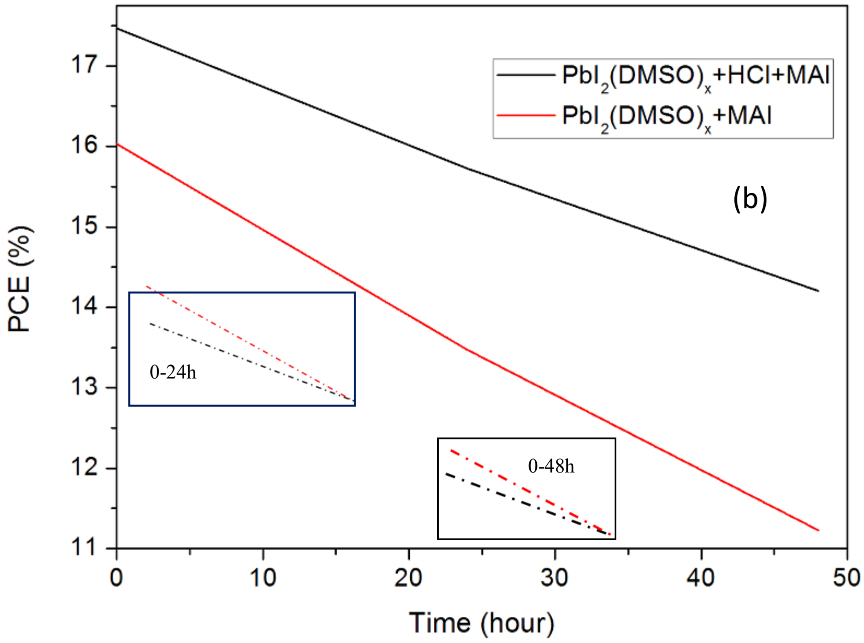

Figure 3.9. Stability on performance of the devices (a) under 85% humidity and at room temperature and (b) under white LED light and at 50 °C (The insert pictures in (a) and (b) are the comparison of the slops for with HCl (black line) and without HCl (red line), respectively).

Table 3.4. The degrade of the PCE for the devices in the stability test

Condition	Device	Time	Degraded of the PCE in percentage
Stability test under 85% humidity and at room temperature	$PbI_2(DMSO)_x$+HCl+MAI	300 h	23%
	$PbI_2(DMSO)_x$+MAI		49%
Stability test under white LED light and at 50℃	$PbI_2(DMSO)_x$+HCl+MAI	48 h	19%
	$PbI_2(DMSO)_x$+MAI		30%

3.4 Conclusions

An efficient, low-cost method to fabricate a uniform and dense perovskite layer with large crystal size has been demonstrated in this investigation by applying DMSO via an intercalation process to increase the crystal size and introducing HCl as an additive to slow-down the crystal growth rate to get more uniform crystals. Concurrently, the crystallinity of the perovskite layer and the charge transport property of the device can be also enhanced. A high efficiency of 17.8% has been achieved by the device with both the DMSO and HCl synergistic treatment. Furthermore, 11% and 17% improvements have been realized with combined DMSO and HCl treatments when compared with the devices with application of only DMSO and only HCl, respectively. Also, the stability of the device from high humidity, high solar irradiation, and high temperature due to HCl treatment has been improved compared with just DMSO treatment.

References

1. Yang, L. J., Wang, J. C., Leung, W. W. F. *Lead Iodide Thin Film Crystallization Control for High-Performance and Stable Solution-Processed Perovskite Solar Cells.* ACS Appl. Mater. Interfaces, 2015. **7**: p. 14614.

2. Li, G., Zhang, T., Zhao, Y. *Hydrochloric acid accelerated formation of planar CH3NH3PbI3 perovskite with high humidity tolerance.* J. Mater. Chem. A, 2015. **3**: p. 19674.

3. Li, G., Zhang, T. Y., Guo, N. J., Xu, F., Qian, X. F., Zhao, Y. X. *Ion‐Exchange‐Induced 2D–3D Conversion of HMA1−xFAxPbI3Cl Perovskite into a High‐Quality MA1−xFAxPbI3 Perovskite.* Angew. Chem. Int. Ed, 2016. **55**: p. 13460.

4. Yang,W. S., Noh, J. H., Jeon, N. J., Kim, Y. C., Ryu, S., Seo, J., Seok, S. I. *High-performance photovoltaic perovskite layers fabricated through intramolecular exchange.* Sci. Express, 2015. **348**: p. 1234.

5. Jo, Y., Oh, K. S., Kim, M. J., Kim, K. H., Lee, H., Lee, C. W., Kim, D. S. *High Performance of Planar Perovskite Solar Cells Produced from PbI2(DMSO) and PbI2(NMP) Complexes by Intramolecular Exchange.* Adv. Mater. Interf, 2016. **3**: p. 1500768.

6. Wu, Y. Z., Islam, A., Yang, X. D., Qin, C. J., Liu, J., Zhang, K., Peng, W. Q., Han, L. Y. *Retarding the crystallization of PbI2 for highly reproducible planar-structured perovskite solar cells via sequential deposition.* Energy Environ. Sci. 2014. **7**: p. 2934–2938.

7. Wu, Y. Z., Chen,W., Yue, Y. F., Liu, J., Bi, E. B., Yang, X. D., Islam, A., Han, L.Y. *Consecutive Morphology Controlling Operations for Highly Reproducible Mesostructured Perovskite Solar Cells.* Appl. Mater. Interf. 2015. **7**: p. 20707.

8. Jeon, N. J., Noh, J. H., Kim, Y. C., Yang, W. S., Ryu, S., Seok, S. I. *Solvent engineering for high-performance inorganic–organic hybrid perovskite solar cells.*

Nat. Mater. 2014. **13**: p. 897.

9. Chang, X. W., Li, W. P., Chen, H. N., Zhu, L. Q., Liu, H. C., Geng, H. F., Xiang, S. S., Liu, J. M., Zheng, X. L., Yang, Y. L., Yang, S. H. *Colloidal Precursor-Induced Growth of Ultra-Even CH3NH3PbI3 for High-Performance Paintable Carbon-Based Perovskite Solar Cells.* ACS Appl. Mater. Interf. 2016. **8**: p. 30184.

10. Chen, H. N., Zheng, X. L., Li, Q., Yang, Y. L., Xiao, S., Hu, C., Bai, Y., Zhang, T., Wong, K. S., Yang, S. H. *An amorphous precursor route to the conformable oriented crystallization of CH3NH3PbBr3 in mesoporous scaffolds: toward efficient and thermally stable carbon-based perovskite solar cells.* J. Mater. Chem. A, 2016. **4**: p. 12897.

11. Li, W. Z., Fan, J. D., Li, J. W., Mai, Y. H., Wang, L. D. *Controllable Grain Morphology of Perovskite Absorber Film by Molecular Self-Assembly toward Efficient Solar Cell Exceeding 17%.* J. Am. Chem. Soc. 2015. **137**: p. 10399.

12. Liu, M. Z., Johnston, M. B., Snaith, H. J. *Efficient planar heterojunction perovskite solar cells by vapour deposition.* Nature, 2013. **501**: p. 395.

13. Zhao, Y. X., Zhu, K. *CH3NH3Cl-Assisted One-Step Solution Growth of CH3NH3PbI3: Structure, Charge-Carrier Dynamics, and Photovoltaic Properties of Perovskite Solar Cells.* J. Phys. Chem. C, 2014. **118**: p. 9412.

14. Zhou, H., Chen, Q., Li, G., Luo, S., Song, T. B., Duan, H. S., Hong, Z., You, J., Liu, Y., Yang, Y. *Interface engineering of highly efficient perovskite solar cells.* Science, 2014. **345**: p. 542.

Chapter 4

Introduction of Graphene Nanofibers into the Perovskite Layer of Perovskite Solar Cells

4.1 Introduction

Recently, the application of graphene-derived nanomaterials in PSCs has been studied. In a typical perovskite solar cell, the perovskite layer is usually sandwiched between the electron- and hole-transporting layers (ETLs and HTLs) [1-8]. Both the electronic structures of the various interfaces and the morphology in PSCs can affect the charge carrier transport properties [9-13]. Reduced graphene oxide (RGO) [14-20], graphene quantum dots (GQDs) [21, 22], or fullerene [18], have been used as an interlayer between the ETL/HTL and the perovskite layer, or being incorporated within the ETL/HTL scaffold to improve the charge-transport efficiency for mesoporous PSCs. In another case, the graphene-derived nanomaterials have been used as top electrode for the PSC to provide efficient charge transfer [23, 24]. Despite these, it is still unclear as to the role of where and how such carbon materials should be introduced into the perovskite film to harness additional benefits. Hadadian et al. dispersed N-doped RGO (N-RGO) into the Pb-based perovskite precursor solution composed of mixed cations [formamidinium (FA), methylammonium (MA)] and halides (I, Br) [25]. They found that the basic (pH>7) sites on N-RGO can provide a different environment surrounding the FA hydrogen atoms, thereby slowing down the crystallization. This leads to larger grains in the perovskite layer and reduction in the charge carrier recombination rate. He et al. used an in-situ solution method for chemical decoration of $CH_3NH_3PbI_3$ (MAI) perovskites with reduced graphene oxides (rGOs) to improve photodetector performance [26].

RGO is known to have lower conductivity and more defects than pristine graphene. CNT also has been used in some researches, but its conductivity, length will get truncated during calcination, so this is not suitable for our research. In addition, although graphene-derived nanosheets and nanoparticles have been widely used in the aforementioned studies, there has been very limited studies on other forms of carbon morphology that might provide positive benefits in terms of device performance for PSCs and the effects of such materials on the performance of the device. These are some of the important issues that are addressed herein.

In this chapter, pristine graphene nanofibers were incorporated into the MAI perovskite layer of planar structure PSCs, which gives rise to two major benefits. First, inducing rapid nucleation is a promising way to obtain perovskite films of high optoelectronic quality [27-31]. Hence, the presence of graphene nanofibers in the perovskite layer is expected to increase the nucleation rate by triggering heterogeneous nucleation over the perovskite precursor film. The 1D graphene nanofibers provide sites for nucleation of perovskite crystals wrapping around the periphery of the graphene nanofibers to forming a multilayer tubular structure. These structures interact with each other and provide a 2D mat for further perovskite crystallization, resulting in large perovskite crystals growing laterally across the dense layer. As a result, there are fewer grain boundaries that provide sites for electron--hole recombination. This helps to improve the FF and J_{sc}. Second, the voltage and current can be further increased by the introduced graphene nanofibers in the perovskite layer to improve the charge carrier transport properties. With this approach, the resulting device exhibits the best PCE of 19.83% under AM 1.5G standard solar simulation as compared a PCE of 17.51% for the reference cell. The performance of the PSC device is thus improved by 13%.

4.2 Experimental Details

4.2.1 Synthesis of graphene nanofibers

Using the methods which are shown in Chapter 2 to prepare the graphene precursor solution and fabricate the graphene nanofibers.

4.2.2 Preparation of CH_3NH_3I Solution with graphene nanofibers

0.23 mg • mL^{-1} graphene nanofibers prepared with different centrifugation times were added into 400 mM CH_3NH_3I in isopropanol (Figure 4.1 (a)-(b)). Then, the solution under different conditions was sonicated until the graphene nanofibers were fully dispersed in the solution.

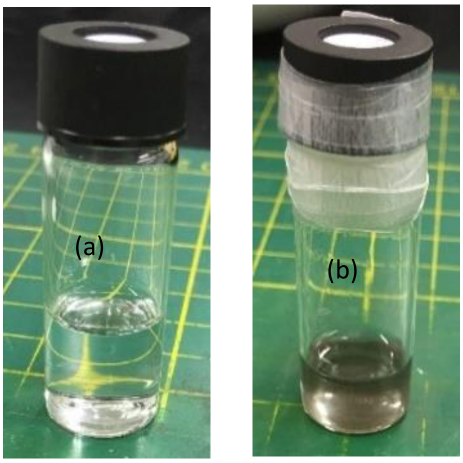

Figure 4.1. (a) Pristine MAI solution. (b) MAI with graphene nanofibers solution with slight tint of grey color.

The methods of preparation of substrate and ETL, synthesis of $PbI_2(DMSO)_x$ Complex, fabrication of perovskite layer and HTL preparation are same as that in Chapter 3. In this study, gold was used for the thermal evaporation.

4.3 Results and Discussion

4.3.1 Morphology and crystallization of perovskite layer

Figure 4.2 (a) and (b) show the SEM images of perovskite layers without graphene nanofibers before annealing and Figure 4.2 (c) and (d) show the SEM images of perovskite layers with graphene nanofibers before annealing (centrifugation time of the graphene solution is 20 min). We can distinctly see the differences of the morphology for the perovskite layer without and with added graphene nanofibers. From Figure 4.2 (c), it can be observed that the spicules in the perovskite layer are the graphene nanofibers with perovskite crystals nucleating partially on the periphery along the length of the graphene nanofibers. In contrast, Figure 4.2 (a) and (b), which show samples without graphene nanofibers (also before annealing), do not show such spicule structures. Figure 4.2 (d) shows a close-up view revealing the details of a spicule from Figure 4.2 (c). Deposited on the spicule are different phases of crystals. Figure 4.2 (d) reveals that, in the early period prior to annealing, nucleation took place with annular layers of as-formed small perovskite crystals wrapping around the periphery of the graphene nanofibers, and large perovskite crystals formed on the surface of the nanofibers. This resulted in a multilayer tubular bundle, which is much larger in diameter than the original graphene nanofiber (ca. 150 nm). The crystals in the annular one-dimensional bundle (darker color) are indeed very large. This may be due to the presence of graphene nanofibers in the "core" of the bundle, which initiate rapid nucleation resulting in large crystals deposited on the graphene nanofiber surface. These large crystals in turn serve as secondary nucleation [32] sites for the surrounding smaller crystals to reform into larger crystals.

Figure 4.3 is a schematic representation of the role of graphene nanofibers in the crystallization process. Smaller perovskite crystals are formed around and on the surface of the graphene nanofibers (Figure 4.3 (a)). These crystals start out as small crystals and subsequently reform into larger crystals. These large crystals form a bundle around the core with graphene nanofibers and they in turn serve as secondary nucleation sites for reformation of small crystals to larger size (Figure 4.3 (b)). Unlike the sample shown in Figure 4.2 (b), which contains many pinholes that lead to electron–hole recombination, the layer with graphene nanofibers shown in Figure 4.2 (d) does not have pinholes.

Figure 4.2 (e) and (f) show SEM images of perovskite layers without and with graphene nanofibers after annealing. From these images, by adding graphene nanofibers into the perovskite, the grain size is increased dramatically when compared to the case without graphene nanofibers. These larger crystals are ideal for providing homogeneous coverage of the perovskite layer on the dense layer eliminating the pinholes that lead to short-circuiting and recombination sites. Moreover, the graphene nanofibers provide the means of growing larger crystals in the lateral two-dimensional plane parallel to that of the substrate.

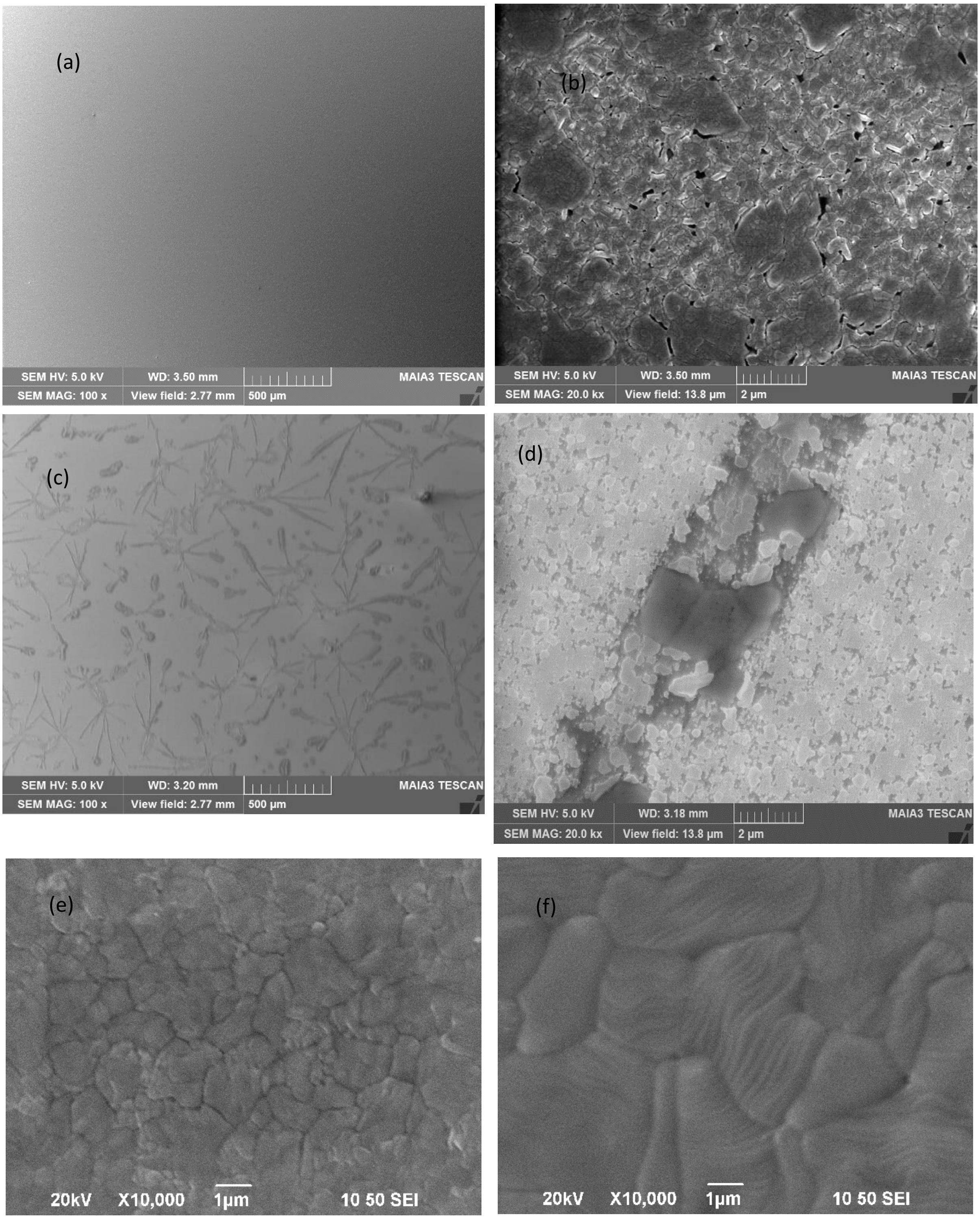

Figure 4.2. (a)-(b) Pristine perovskite layer before annealing. (c)-(d) Perovskite with graphene nanofibers before annealing. (e) Pristine perovskite layer after annealing. (f) Perovskite layer with graphene nanofibers after annealing.

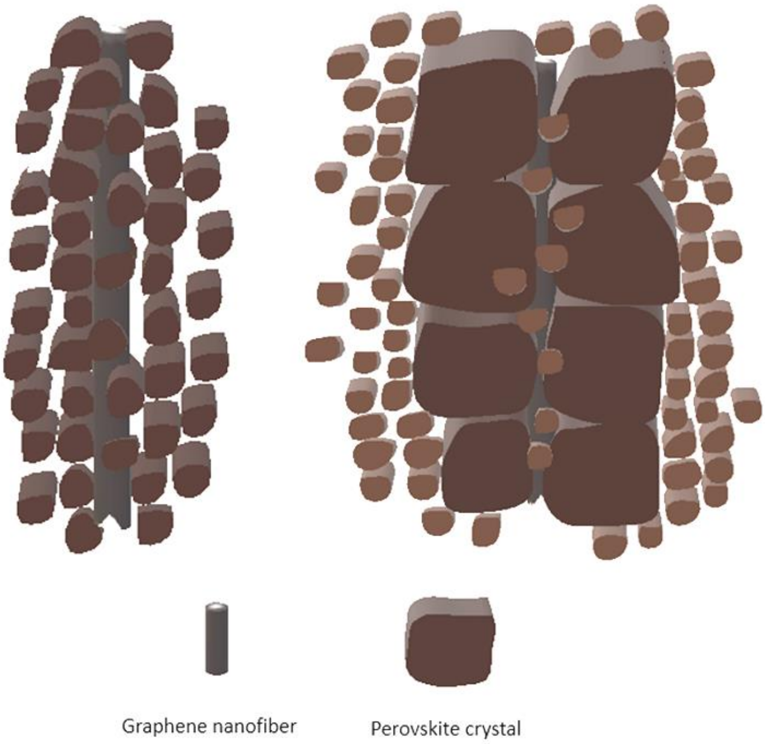

Figure 4.3. Schematic for role of graphene nanofibers in the crystallization of the perovskite.

The cross-section of the perovskite layers without and with graphene nanofibers are shown in Figure 4.4. The thicknesses of the perovskite layers with and without graphene nanofibers are comparable.

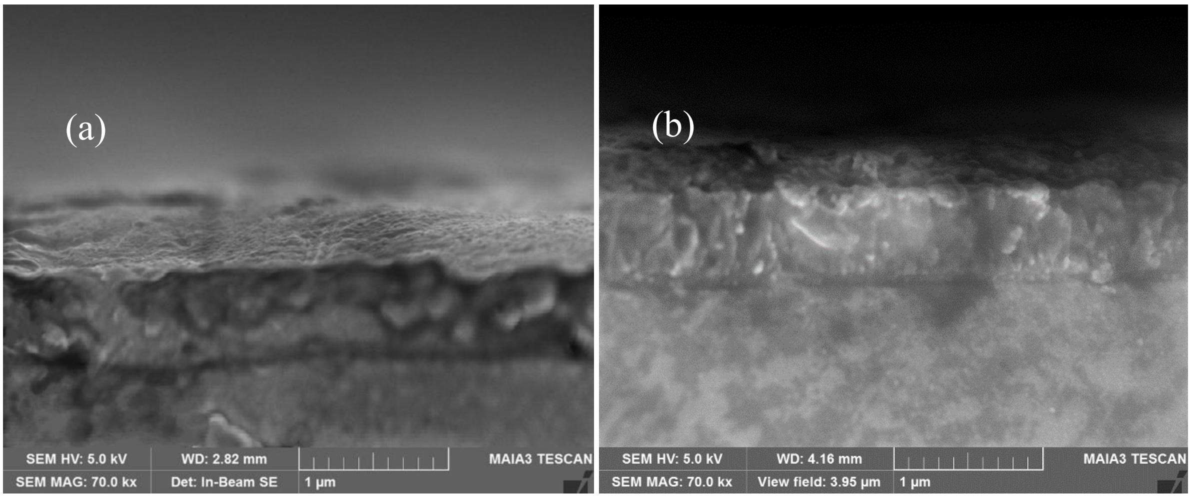

Figure 4.4. (a) cross-section of the pristine perovskite. (b) cross-section of perovskite

with graphene nanofibers.

Figure 4.5 shows the morphology of the graphene nanofibers that are added into the perovskite layer, under different centrifuge time (3 min, 20 min and 60 min). Figure 4.6 shows the SEM images of perovskite layers with graphene nanofibers with different centrifugation time (centrifugation times of 3 min and 60 min, respectively). The best condition is the 20 min centrifugation time, the average diameter of the nanofibers is about 150 nm. From Figure 4.5 and 4.6 we can see that when the centrifugation time of the graphene suspension is too short (e.g. 3 min), much of the graphene sheet remains in the supernatant. When the latter is being electrospun to produce nanofibers, the fibers have flakes. These graphite flakes among the nanofibers lead to high electron–hole recombination. In contrast, when the centrifugation time is too long (e.g. 60 min), many large graphene sheets are centrifuged out of the suspension into the residue and only a few small graphene sheets are left behind in the supernatant, leading to short graphene nanofibers that might not be beneficial for enlarging perovskite grain size and improving the electrical conductivity of the PSC device.

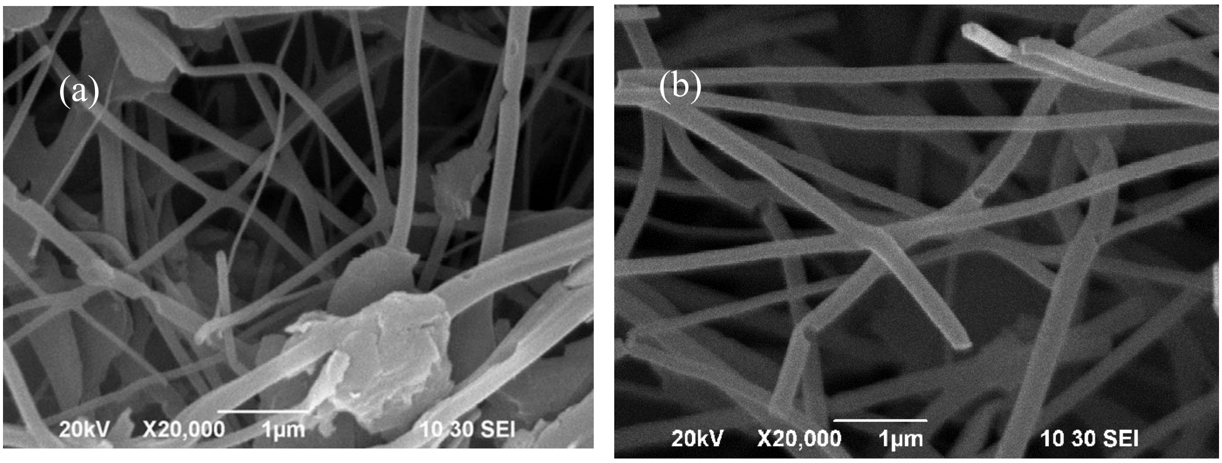

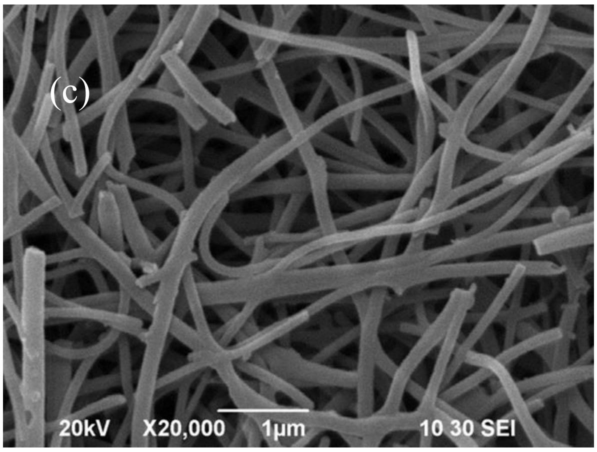

Figure 4.5. SEM images of (a) graphene nanofibers centrifuged 3 min showing graphite flakes; (b) graphene nanofibers centrifuged 20 min (best condition); (c) graphene nanofibers centrifuged 60 min.

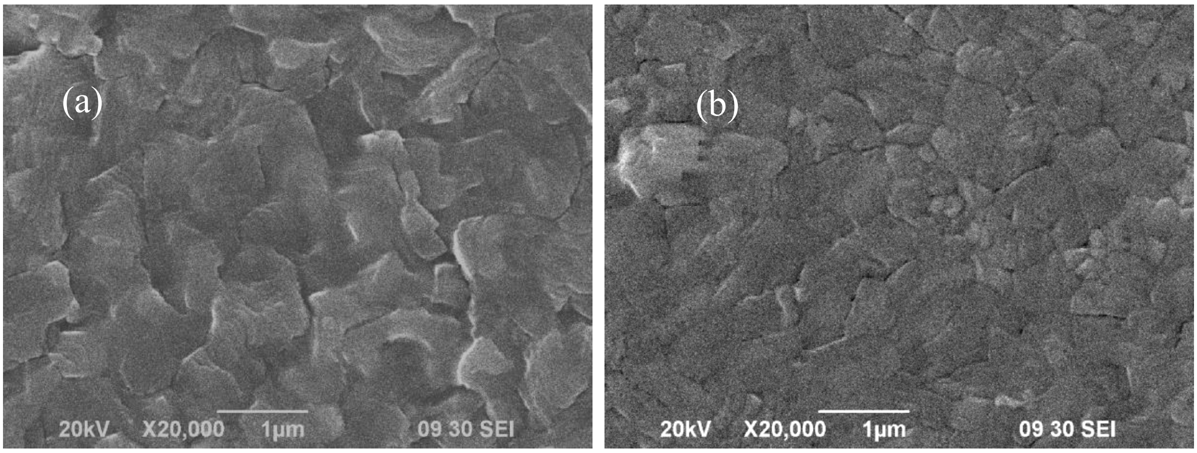

Figure 4.6. SEM images of (a) perovskite layer with graphene nanofibers (centrifuge time 3 min) (b) perovskite layer with graphene nanofibers (centrifuge time 60 min).

The XRD patterns of the perovskite layer with and without graphene nanofibers are shown in Figure 4.7. The crystal structure of the perovskite phase is unchanged with and without graphene nanofibers in the perovskite layers. Comparing the areas of the main peak (110) of $CH_3NH_3PbI_3$ in both cases, the area for the perovskite with graphene nanofibers is 11% larger than that for the pristine perovskite (no graphene nanofibers). This implies that the introduction of graphene nanofibers in the perovskite further improves the crystallinity with the larger crystals.

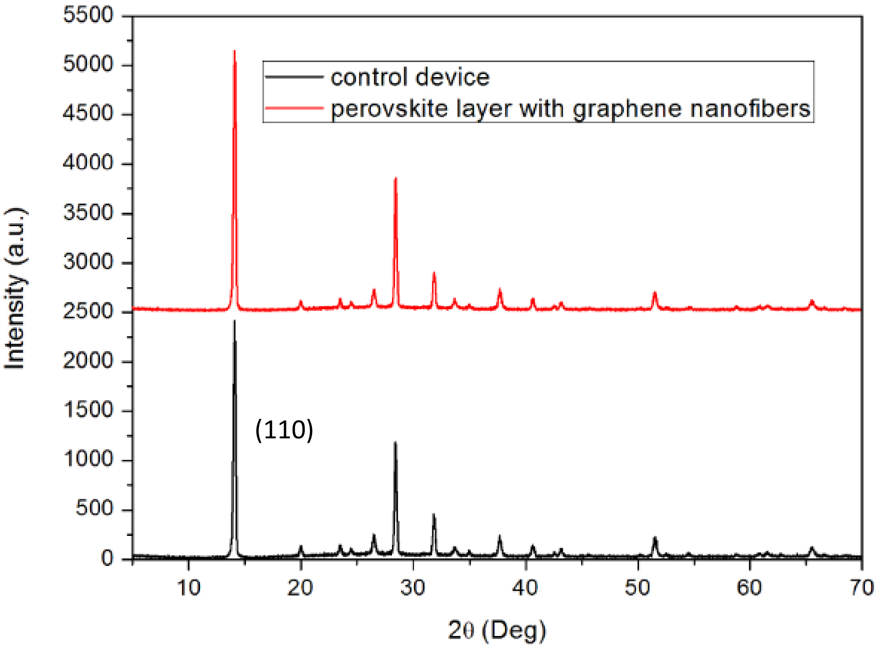

Figure 4.7. XRD patterns of perovskite layers with and without graphene nanofibers.

To further investigate whether the graphene nanofibers are indeed in the perovskite layer, Raman spectroscopy was carried out (Figure 4.8 (a)). The spectrum for $CH_3NH_3PbI_3$ with graphene nanofibers includes two bands at 1350 and 1566 cm^{-1} (Figure 4.8 (a), inset), corresponding to the D and G bands of graphene, respectively. This indeed confirms the presence of graphene nanofibers in the perovskite layer. The Raman spectrum of graphene nanofibers with 20 min centrifugation time is shown in Figure 4.8 (b). There are also two peaks at approximately 1349 and 1565 cm^{-1}, corresponding, respectively, to the D peak associated with edge defects and the G peak associated with the highly ordered graphite. The 2D peak is at approximately 2727 cm^{-1}. The morphology and thickness of the graphene sheet is reflected by the intensity and shape of this peak, which is quite symmetrical, revealing high quality graphene.

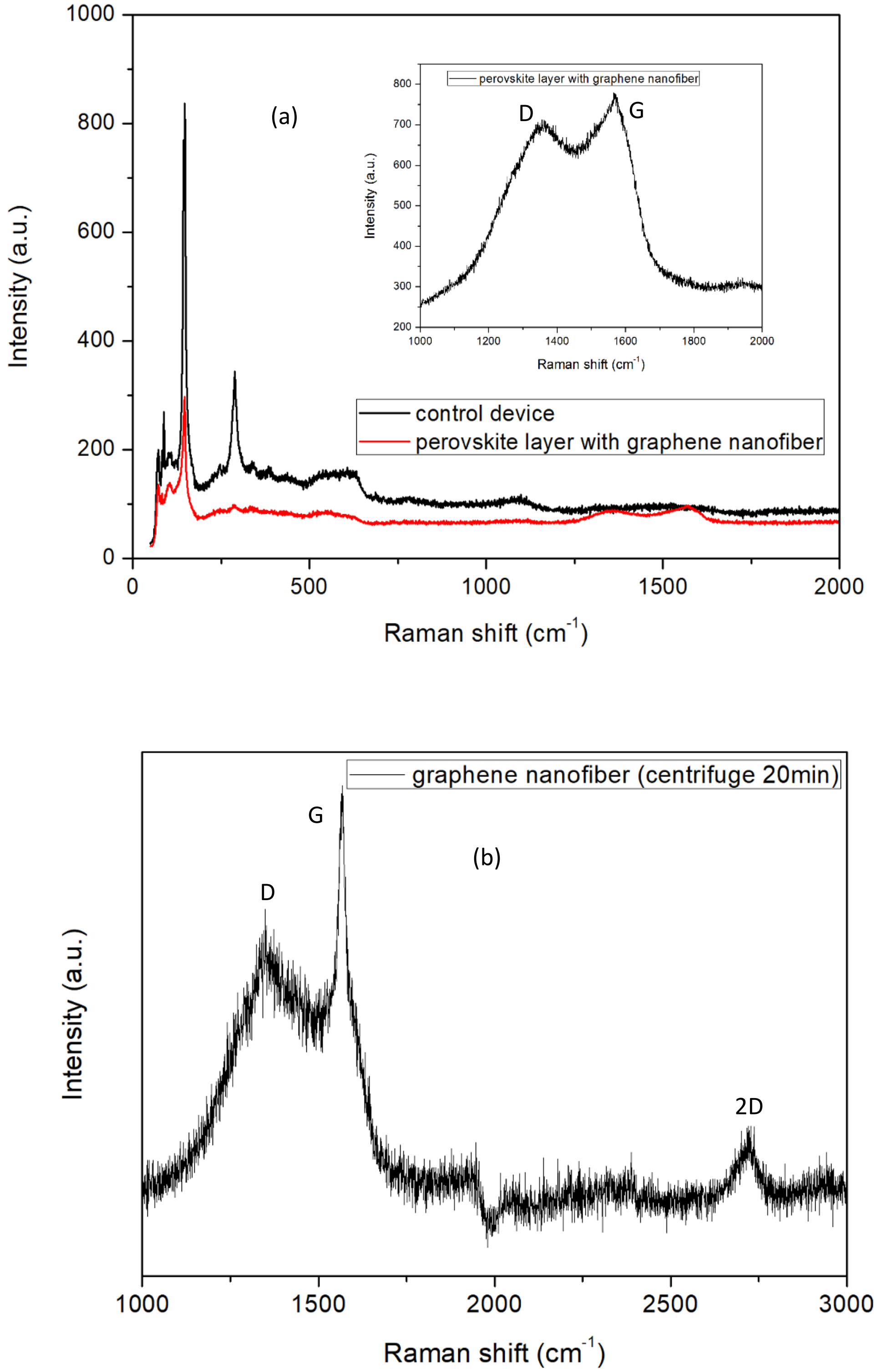

Figure 4.8. Raman spectrum of (a) perovskite layers; (b) graphene nanofibers (centrifuge time is 20 min).

4.3.2 Photovoltaic performance

The current density–voltage (J–V) curves for PSC devices with graphene nanofibers produced with different centrifugation times are shown in Figure 4.9. The addition of graphene nanofibers in the perovskite layer is shown to improve the performance of the device when compared with the control device without graphene nanofibers in the perovskite layer. The curves also reveal that the different centrifugation times for the graphene suspension can affect the performance of the device. The optimal conditions corresponded to the case with a centrifugation time of 20 min, for which the maximum efficiency of 19.83% was attained with a J_{sc} of 24.38 $mAcm^{-2}$, V_{oc} of 1.08 V, and FF of 76% (Figure 4.9). The parameters corresponding to the best performance for all conditions are listed in Table 4.1 and the parameters corresponding to the average performance are listed in Table 4.2. Comparing the data in Table 4.1, the device performance parameters under the optimal conditions of introducing graphene nanofibers (with a centrifugation time of 20 min) into the perovskite layer are all higher than that for the control device. Both the J_{sc} and FF values were improved dramatically. In consequence, the final PCE was increased to 113% that of the control case without graphene. The much larger grain size in the perovskite layer and improved crystallinity of the perovskite layer with graphene nanofibers leads to much higher FF and J_{sc} values. Moreover, introducing graphene nanofibers into the perovskite layer can improve the charge carrier transport properties, which can further increase both J_{sc} and V_{oc} values. The J_{sc} obtained from EQE is shown in Table 4.1. The slight difference between the Jsc acquired by the density−voltage (i.e. J−V curves) and the J_{sc} obtained by EQE test may be due to the error in the calibration of the equipment for the EQE test. The values of series resistance (R_s) and shunt resistance (R_{SH}) are also given in Table 4.1. R_s can be estimated by the inverse of the slope near the open-circuit potential and the R_{SH} can be estimated by the inverse slope near the short-circuit current. The device with graphene nanofibers (centrifuge time 20 min) in the perovskite layer has the lowest R_s, which means conductivity of every layer of the device is high, whereas this device has the highest R_{SH}, which indicates that the power loss in the solar cell through an alternate current path is very small, resulting in high FF. From the J–V curves in reverse and forward sweeps for the perovskite layers with and without graphene nanofibers (Figure 4.10), it can be seen that the introduction of graphene nanofibers into the perovskite layer also facilitates reduction of the device hysteresis. The UV/Vis absorbance spectroscopy and external quantum efficiency (EQE) results are shown in Figures 4.11 and Figure 4.12. Introducing graphene nanofibers into the perovskite layer is shown to enhance light absorption, especially for wavelengths less than 550 nm. The use of graphene nanofibers in the perovskite layer further improves the EQE performance, especially at wavelengths less than 750 nm. This is consistent with the increased absorbance (as shown in Figure 5.11) in that improved crystallinity can better harvest light.

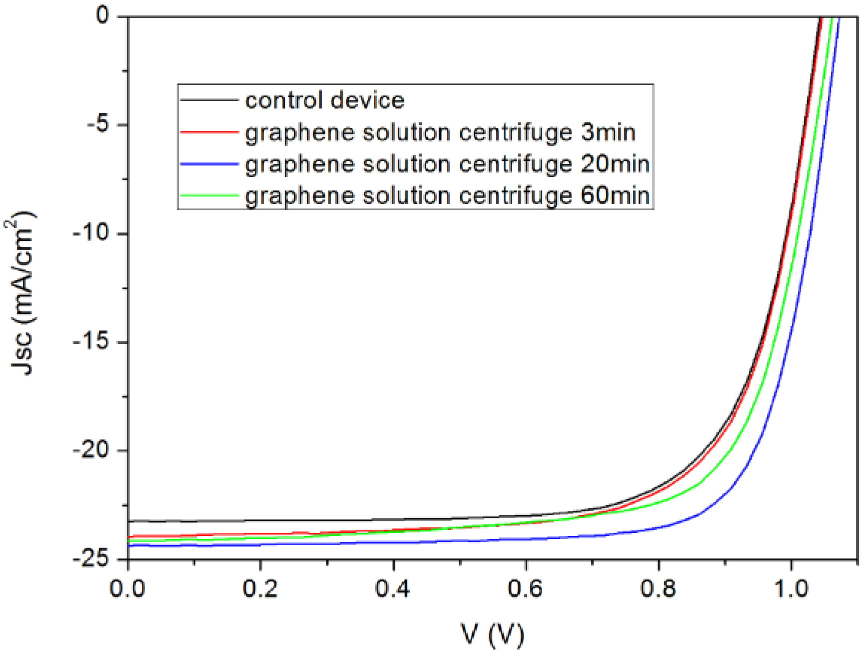

Figure 4.9. J–V curves measured under 100 mW·cm^{-2} AM1.5G illumination.

Table 4.1. Best performance of the Perovskite Solar Cells under AM 1.5 G illumination

	V_{oc} (V)	J_{sc} (mA/cm^2)	FF (%)	PCE (%)	Jsc/mA•cm^{-2} obtained by EQE	Rs (Ω • cm^2)	RSH (Ω·cm^2)
Control	1.05	23.27	72	17.51	22.2	0.33	1858.1
Graphene suspension centrifuged 3 min	1.05	23.95	70	17.70	22.5	0.30	1993.8
Graphene suspension centrifuged 20 min	1.08	24.38	76	19.83	23.5	0.22	3628.8
Graphene suspension centrifuged 60 min	1.05	24.13	73	18.50	23	0.33	1502.3

Table 4.2. Average performance of the Perovskite Solar Cells

	V_{oc} (V)	J_{sc} (mA/cm^2)	FF(%)	PCE (%)
Control	1.04±0.02	23.00±0.22	68±1	16.90±0.20
Graphene suspension centrifuged 3 min	1.04±0.02	23.50±0.30	66±2	17.00±0.31
Graphene suspension centrifuged 20 min	1.06±0.02	24.00±0.23	72±2	18.90±0.21
Graphene suspension centrifuged 60 min	1.04±0.02	23.50±0.38	70±1	17.70±0.30

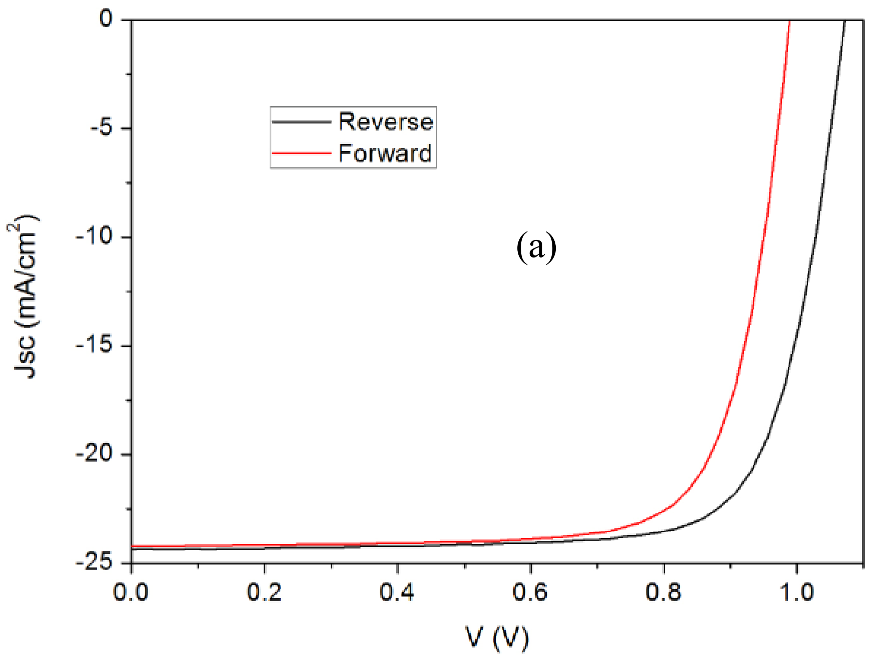

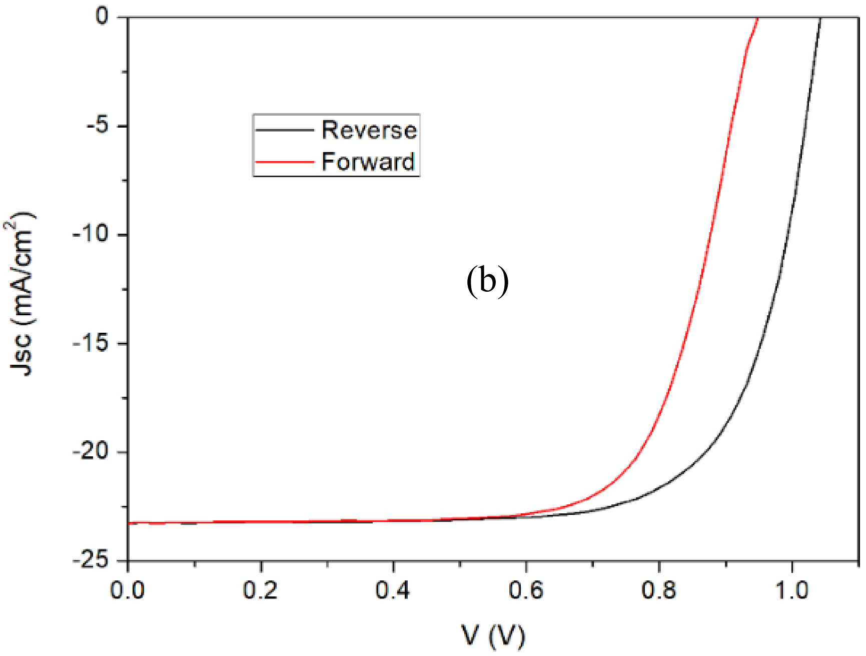

Figure 4.10. J-V curves in reverse and forward sweep (a) perovskite with graphene nanofibers (centrifuge time 20 min); (b) control device.

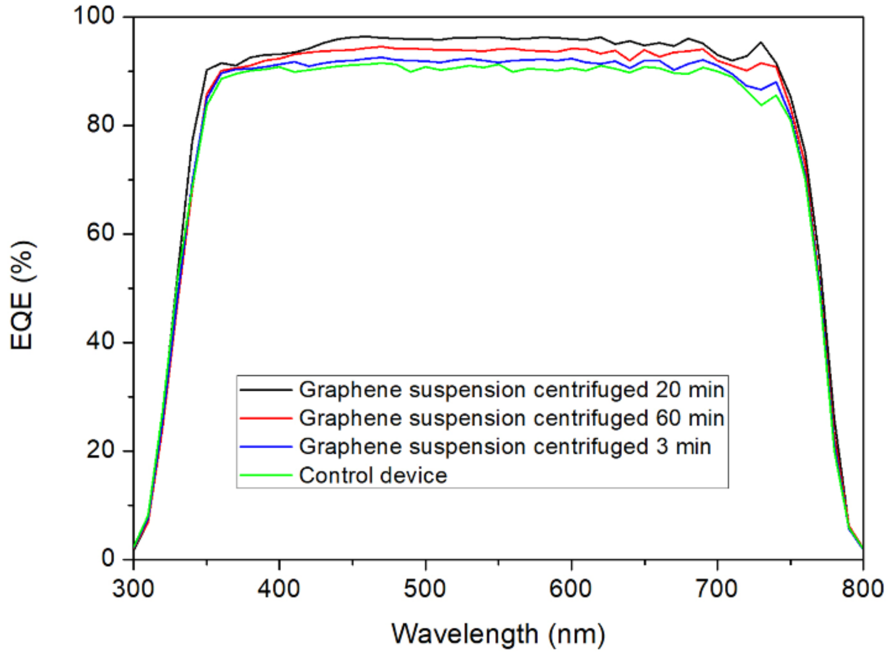

Figure 4.11. External quantum efficiency.

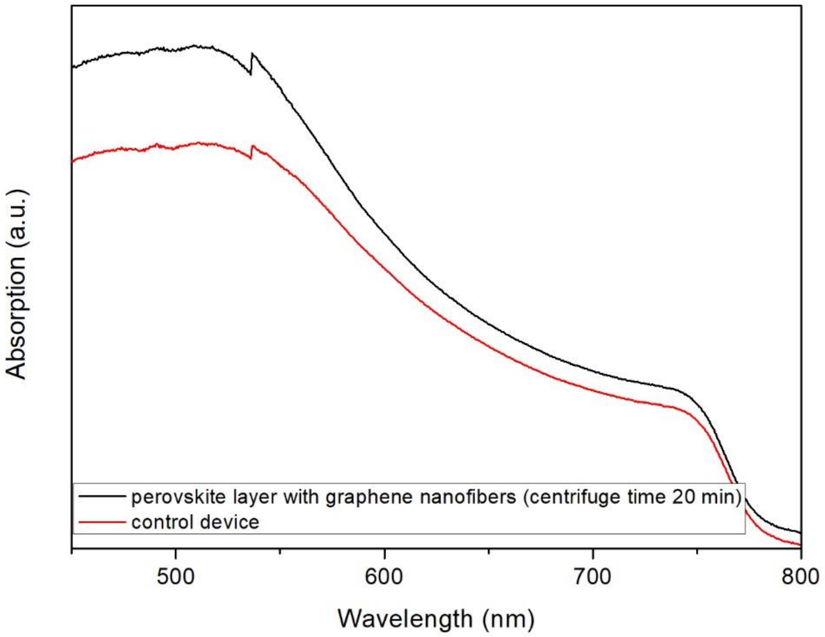

Figure 4.12. UV−vis Absorbance Spectra.

Charge-transport times in the solar cells were investigated by IMPS. Figure 4.13 shows the typical Nyquist plots of IMPS response curves of the solar cells for the perovskite layers with graphene nanofibers produced under different centrifugation times. We have calculated the charge-transport times for the devices under different centrifugation times (Table 4.3). Figure 4.14 shows a correlation of the transport time with the PCE for devices under different conditions. The charge-transport time and PCE are very well correlated. When charge-transport time decreases, PCE increases, and vice versa. The best PCE with the lowest charge-transport time implies the fastest charge mobility.

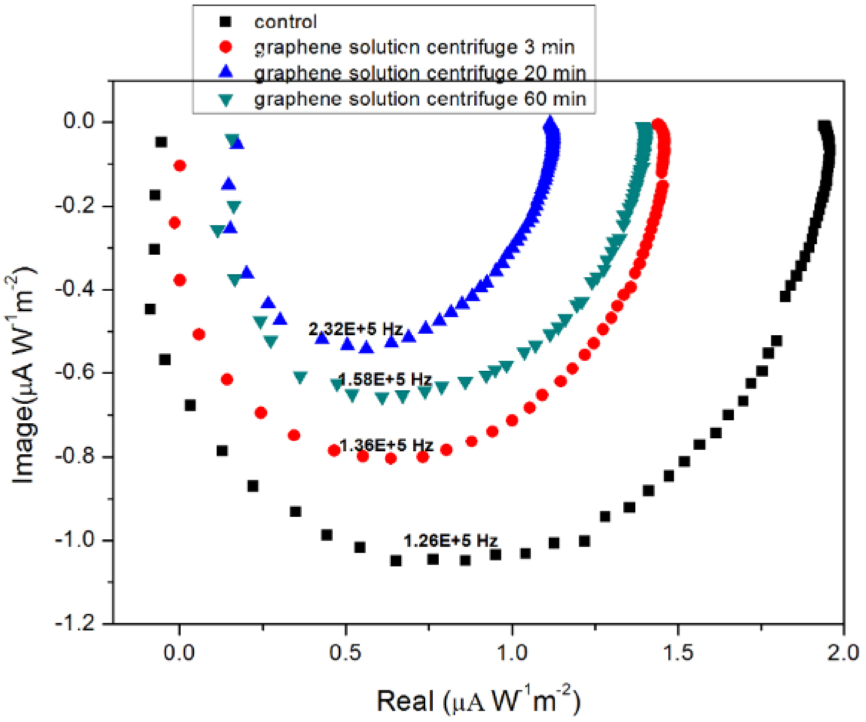

Figure 4.13. Typical IMPS response of the devices under different conditions.

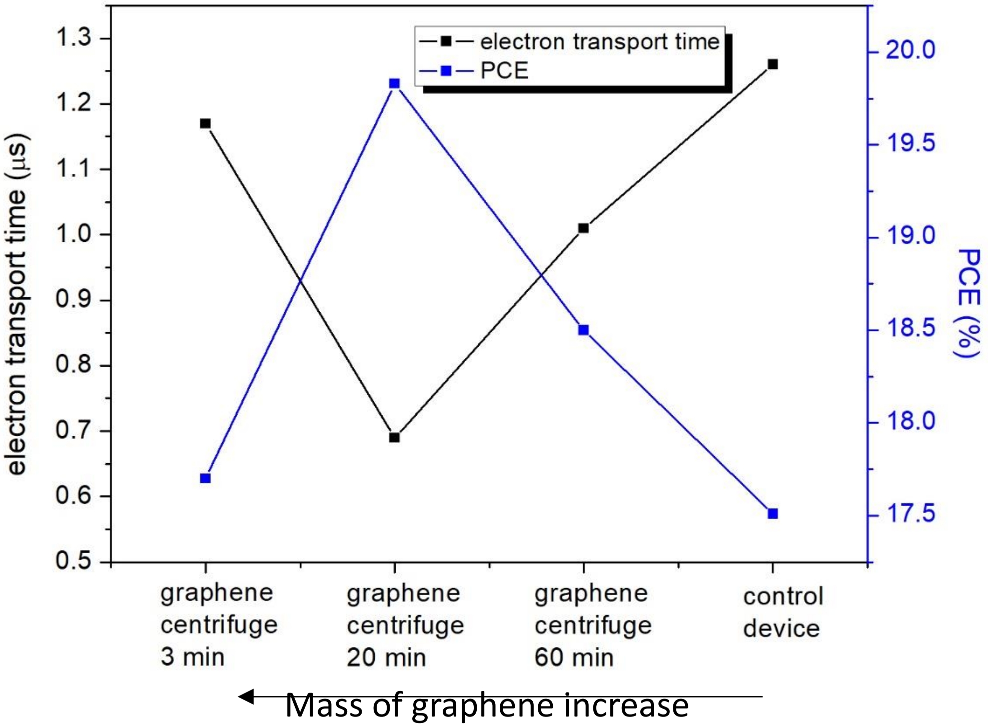

Figure 4.14. Comparison chart of the transport time and PCE for the devices under different conditions.

Table 4.3. The electron transport time with respect to the PCE of the devices

	charge transport time (μs)	PCE (%)
Control	1.26	17.51
Graphene suspension centrifuged 3 min	1.17	17.70
Graphene suspension centrifuged 20 min	0.69	19.83
Graphene suspension centrifuged 60 min	1.01	18.50

As shown in Figure 4.15, the graphene nanofibers provide a dedicated path or highway for photogenerated charges to be transported efficiently across the perovskite layer without being lost. For example, such charges can be lost by recombination at the crystal–crystal interface or defects and traps in the crystals. From the steady-state PL (Figure 4.16), we can see that the electrons are transferred more effectively in the perovskite layer with graphene nanofibers than in that without graphene nanofibers. As a consequence, the recombination rate can be reduced in the perovskite–graphene nanofibers layer, which means the number of electron–hole pairs is reduced in the perovskite–graphene nanofibers layer and thus the PL intensity is also reduced.

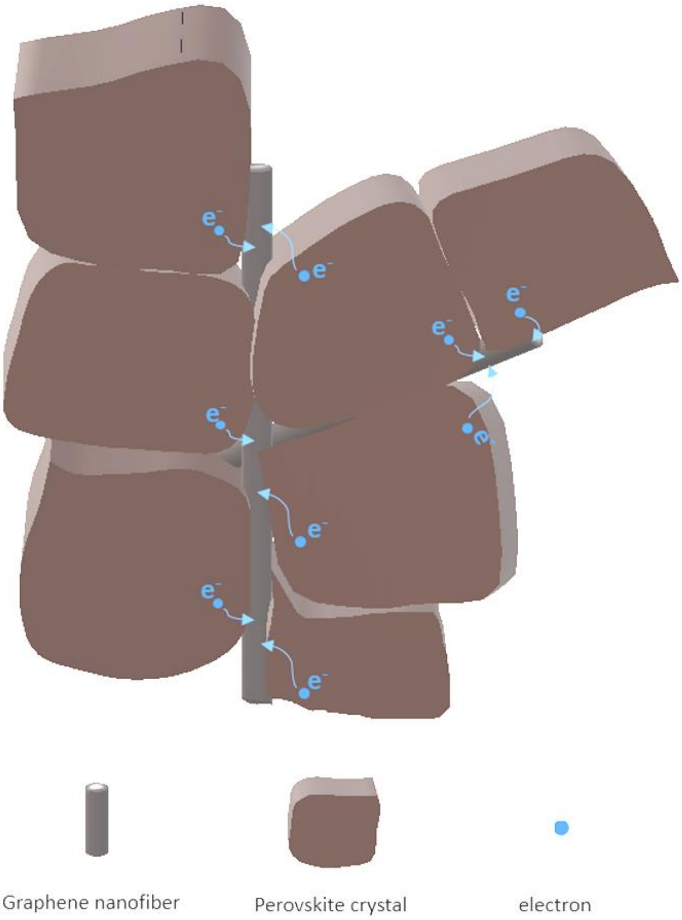

Figure 4.15. The Schematic of the role of graphene nanofibers for the electron transport**.**

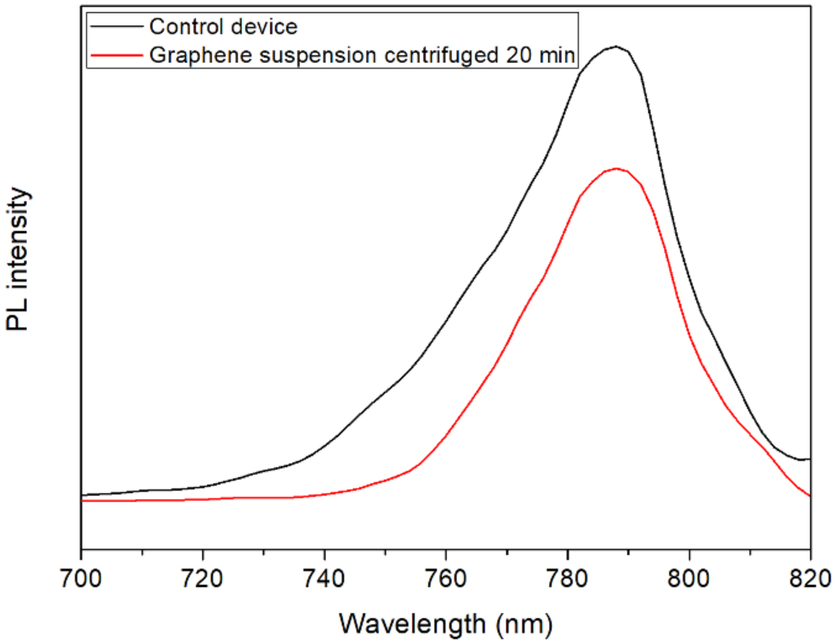

Figure 4.16. Steady-state PL of perovskite films under different conditions.

Figure 4.17 shows the TRPL signal and the fits by using a biexponential function. The decays can be well-fitted indeed. When the perovskite layer was fabricated with embedded graphene nanofibers, the PL decay was over four times lower than that of the control device (perovskite layer without graphene nanofibers). The longer lifetime of the perovskite layer with graphene nanofibers is also due to the improved photoelectronic properties, which can demonstrate the lower trap-state density in the perovskite layer with graphene nanofibers than in that without graphene nanofibers. The summary of PL decay parameters corresponding to the fitting equation is shown in Table 4.4.

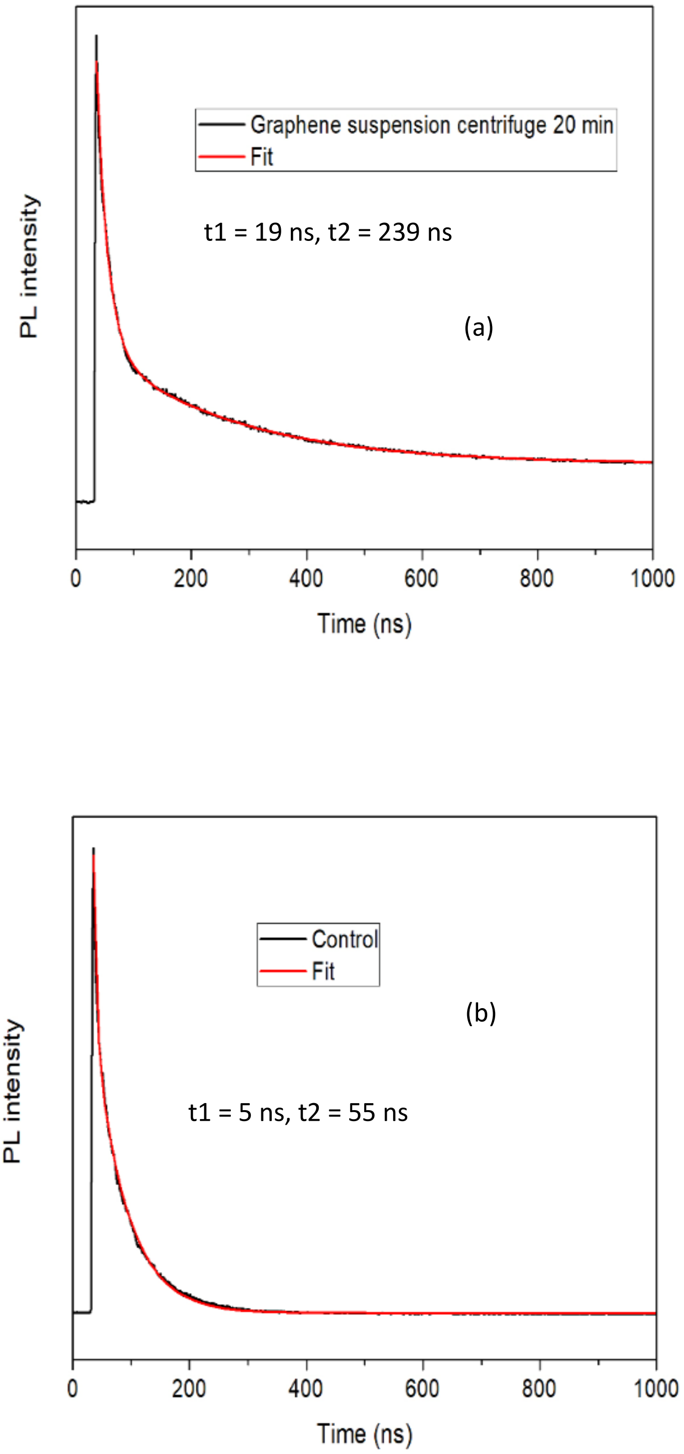

Figure 4.17. The TRPL of the perovskite film under different conditions.

Table 4.4. Summary of PL decay parameters corresponding to a biexponential fitting of the TRPL decay curves for the devices under different conditions

Equation: $y = y_0 + A_1 e^{-(x-x0)/t1} + A_2 e^{-(x-x0)/t2}$				
	A_1	t1	A_2	t2
Control	6048	5	6802	55
Graphene suspension centrifuged 20 min	13567	19	2945	239

4.3.3 Stability test

The devices fabricated by different methods were placed under a relative humidity (RH) of 85% and room temperature but without voltage load or constant illumination for a period. The time for the stability test is not irradiation time in the entire period but at three different times, initially, in middle and final time. So the time scale refers to the storage time and not irradiation time. The performance of the devices with graphene nanofibers in the perovskite layer decreased by 6% after 150 h and by 10.5% after 300 h, whereas that of the devices without graphene nanofibers decreased by 10% and 18%, respectively, over the same periods.

The change in performance over time at 85% RH is shown in Figure 4.18. From the slopes of the two curves representing the change in PCE over time (Figure 4.18 (a) and inset), we can see that the devices with graphene nanofibers in the perovskite layers have lower slopes during the test period than that without graphene nanofibers, which means the addition of graphene nanofibers in the perovskite layer can help to improve the stability of the device. The changes in V_{oc}, J_{sc}, and FF of the devices over time are shown in Figure 4.18 (b)–(d), from which we can see that decreases in FF and J_{sc} are the main reasons for the decrease in PCE. The above results suggest that the presence of graphene nanofibers in the perovskite layer can help to increase the grain size and reduce the grain boundaries. The take-up of moisture occurs preferentially at grain boundaries and, as a result, the films with more grain boundaries demonstrated poorer moisture stability, which was also observed in terms of device stability [33, 34].

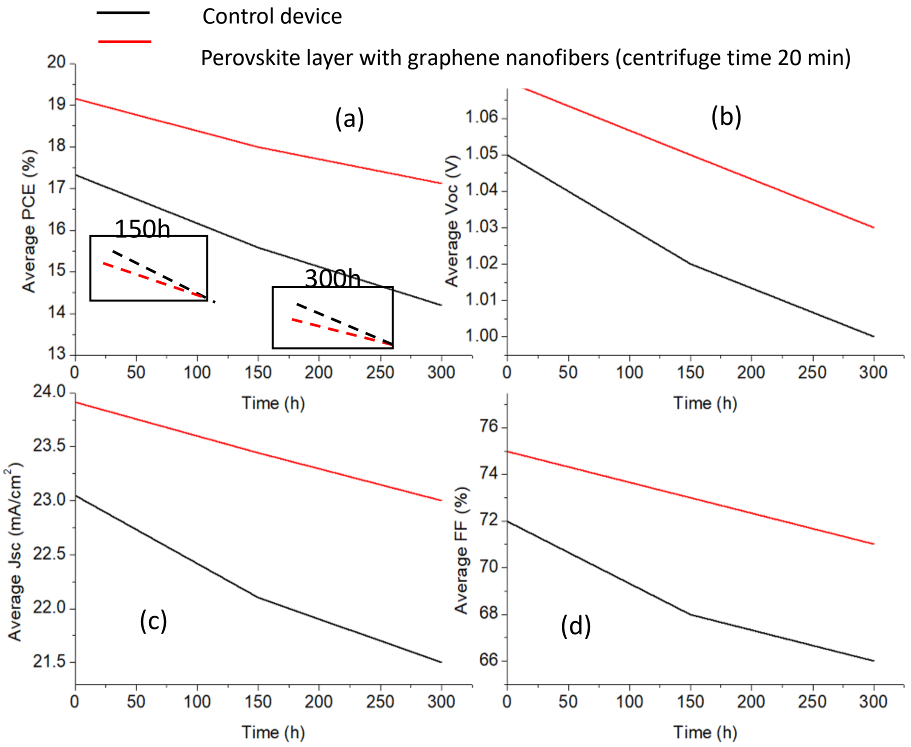

Figure 4.18. Performance stability of the devices under 85% relative humidity at room temperature: (a) PCE (inset shows comparison of the slopes for the devices with graphene nanofibers and without graphene nanofibers); (b) V_{oc}; (c) J_{sc}; (d) FF.

4.4 Conclusions

In conclusion, we have successfully incorporated graphene nanofibers in the perovskite layer of the perovskite solar cell. The quality of the graphene nanofibers was optimized by controlling the centrifugation time at high centrifugal acceleration on the precursor suspension for electrospinning nanofibers. We found that the optimal conditions corresponded to a precursor suspension that had been centrifuged for 20 min prior to electrospinning into graphene nanofibers, which were subsequently added to the perovskite layer. Under the optimized conditions, the device PCE increased from 17.51% without graphene nanofibers to 19.83% with graphene nanofibers. Firstly, the introduction of graphene nanofibers led to rapid nucleation and reformation of smaller crystals into much larger crystals of over 2 μm. These large crystals have fewer grain boundaries and better crystallinity, which results in much higher FF and J_{sc} values. Secondly, the much higher J_{sc} and V_{oc} values can be attributed to the improvement in charge-transport properties on incorporating graphene nanofibers into the perovskite layer. The electron transport time for the graphene nanofiber containing PSC was nearly half of that of the PSC device without graphene nanofibers. The stability of the device was also improved.

References

1. Zhou, H., Chen, Q., et al. *Fabrication and Properties of Titanium Based Flexible Organic Perovskite Solar Cells.* Science, 2014. **345**: p. 542.
2. Wu, Z. W., Bai, S., et al. *Efficient planar heterojunction perovskite solar cells employing graphene oxide as hole conductor.* Nanoscale, 2014. **6**: p. 10505.
3. Malinkiewicz, O., Yella, A., et al. *Perovskite solar cells employing organic charge-transport layers.* Nat. Photonics, 2014. **8**: p. 128.
4. Arora, N., Dar, M. I., et al. *Perovskite solar cells with CuSCN hole extraction layers yield stabilized efficiencies greater than 20%.* Science, 2017. **358**: p. 768.
5. Heo, J. H., Shin, D. H., et al. *Super-flexible bis(trifluoromethanesulfonyl)-amide doped graphene transparent conductive electrodes for photo-stable perovskite solar cells.* J. Mater. Chem. A, 2018. **6**: p. 8251.
6. Kakavelakis, G., Maksudov, T., et al. *Efficient and Highly Air Stable Planar Inverted Perovskite Solar Cells with Reduced Graphene Oxide Doped PCBM Electron Transporting Layer.* Adv. Energy Mater. 2017. **7**: p. 1602120.
7. Zhou, Z., Li, X., et al. *Stable Inverted Planar Perovskite Solar Cells with Low‐Temperature‐Processed Hole‐Transport Bilayer.* Adv. Energy Mater. 2017. **7**: p. 1700763.
8. Petridis, K., Kakavelakis, G., et al. *Graphene‐Based Inverted Planar Perovskite Solar Cells: Advancements, Fundamental Challenges, and Prospects.* Chem. Asian J. 2018. **13**: p. 240.
9. Stranks, S. D., Eperon, G. E., et al. *Electron-Hole Diffusion Lengths Exceeding 1 Micrometer in an Organometal Trihalide Perovskite Absorber.* Science, 2013. **342**: p. 341.

10. Eperon, G. E., Burlakov, V. M., et al. *Morphological Control for High Performance, Solution‐Processed Planar Heterojunction Perovskite Solar Cells.* Adv. Funct. Mater. 2014. **24**: p. 151.

11. Wang, Z. K., Li, M., et al. *Improved Hole Interfacial Layer for Planar Perovskite Solar Cells with Efficiency Exceeding 15%.* ACS Appl. Mater. Interfaces, 2015. **7**: p. 9645.

12. Palma, A. L., Cina, L., et al. *Reduced graphene oxide as efficient and stable hole transporting material in mesoscopic perovskite solar cells.* Nano Energy, 2016. **22**: p. 349.

13. Qian, M., Li, M., et al. *Planar perovskite solar cells with 15.75% power conversion efficiency by cathode and anode interfacial modification.* J. Mater. Chem. A, 2015. **3**: p. 13533.

14. Petridis, C., Kakavelakis, G., et al. *Renaissance of graphene-related materials in photovoltaics due to the emergence of metal halide perovskite solar cells.* Energy Environ. Sci. 2018. **11**: p. 1030.

15. Han, G. S., Song, Y. H., et al. *Reduced Graphene Oxide/Mesoporous TiO2 Nanocomposite Based Perovskite Solar Cells.* ACS Appl. Mater. Interfaces, 2015. **7**: p. 23521.

16. Cho, K. T., Grancini, G., et al. *Beneficial Role of Reduced Graphene Oxide for Electron Extraction in Highly Efficient Perovskite Solar Cells.* ChemSusChem, 2016. **9**: p. 3040.

17. Feng, S. L., Yang, Y. G., et al. *High-Performance Perovskite Solar Cells Engineered by an Ammonia Modified Graphene Oxide Interfacial Layer.* ACS Appl. Mater. Interfaces, 2016. **8**: p. 14503.

18. Chung, C. C., Narra, S., *Inverted planar solar cells based on perovskite/graphene oxide hybrid composites.* J. Mater. Chem. A, 2017. **5**: p. 13957.

19. Jokar, E., Huang, Z. Y., et al. *Anomalous Charge‐Extraction Behavior for Graphene‐Oxide (GO) and Reduced Graphene‐Oxide (rGO) Films as Efficient p‐Contact Layers for High‐Performance Perovskite Solar Cells.* Adv. Energy Mater. 2018. **8**: p. 1701640.

20. Kakavelakis, G., Paradisanos, I., et al. *Extending the Continuous Operating Lifetime of Perovskite Solar Cells with a Molybdenum Disulfide Hole Extraction Interlayer.* Adv. Energy Mater. 2018. **8**: p. 1702287.

21. Zhu, Z. L., Ma, J. N., et al. *Efficiency Enhancement of Perovskite Solar Cells through Fast Electron Extraction: The Role of Graphene Quantum Dots.* J. Am. Chem. Soc. 2014. **136**: p. 3760.

22. Fang, X., Ding, J., et al. *Graphene quantum dot incorporated perovskite films: passivating grain boundaries and facilitating electron extraction.* Phys. Chem. Chem. Phys. 2017. **19**: p. 6057.

23. Abrusci, A., Stranks, S. D., et al. *High-Performance Perovskite-Polymer Hybrid Solar Cells via Electronic Coupling with Fullerene Monolayers.* Nano Lett. 2013. **13**: p. 3124.

24. Zhang, L., Liu, T., et al. *The effect of carbon counter electrodes on fully printable mesoscopic perovskite solar cells.* J. Mater. Chem. A, 2015. **3**: p 9165.

25. Yan, K., Wei, Z., et al. *High‐Performance Graphene‐Based Hole Conductor‐Free Perovskite Solar Cells: Schottky Junction Enhanced Hole Extraction and Electron Blocking.* Small, 2015. **11**: p. 2269.

26. Hadadian, M., Correa-Baena, J. P., et al. *Enhancing Efficiency of Perovskite Solar Cells via N‐doped Graphene: Crystal Modification and Surface Passivation.* Adv. Mater. 2016. **28**: p. 8681.

27. Bi, D. Q., Tress, W., et al. Efficient luminescent solar cells based on tailored mixed-cation perovskites. Sci. Adv. 2016. **2**: p. e1501170.

28. He, M., Chen, Y. N., et al. *Chemical decoration of CH3NH3PbI3 perovskites with*

graphene oxides for photodetector applications. Chem. Commun. 2015. **51**: p. 9659.

29. Li, G., Zhang, T., Zhao, Y. *Hydrochloric acid accelerated formation of planar CH3NH3PbI3 perovskite with high humidity tolerance.* J. Mater. Chem. A, 2015. **3**: p. 19674.
30. Lee, J. W., Kim, H. S., Park, N. G. *Lewis Acid–Base Adduct Approach for High Efficiency Perovskite Solar Cells.* Acc. Chem. Res. 2016. **49**: p. 311.
31. Liang, P. W., Liao, C. Y., et al. *Additive Enhanced Crystallization of Solution‐Processed Perovskite for Highly Efficient Planar‐Heterojunction Solar Cells.* Adv. Mater. 2014. **26**: p. 3748.
32. Botsaris, G. D. in Industrial Crystallization (Ed.: J. W. Mullin), Springer, Boston, USA, 1976, p. 3 –22.
33. Wang, Q., Chen, B., et al. *Scaling behavior of moisture-induced grain degradation in polycrystalline hybrid perovskite thin films.* Energy Environ. Sci. 2017. **10**: p. 516.
34. Chiang, C. H., Wu, C. G. *Film Grain‐Size Related Long‐Term Stability of Inverted Perovskite Solar Cells.* ChemSusChem, 2016. **9**: p. 2666.

Chapter 5

Improving crystallization and charge transfer by using a structured nanofiber scaffold for perovskite solar cell

5.1 Introduction

As known, TiO_2 has been widely used in PSCs, in the typical mesoscopic devices TiO_2 nanoparticles are usually used as the scaffold layer between the TiO_2 compact (or transport) layer and the perovskite layer. The porous n-type TiO_2 films not only transport photoexcited electrons from the perovskite absorbing layer but they also facilitate the perovskite crystal transformation when the perovskite layer is fabricated by the sequential deposition process [1]. However, using TiO_2 nanoparticles as scaffold in PSCs frequently lead to inefficient electron transport in the nanocrystalline films as electrons have to hop from one nanoparticle to the next, and the particle-particle interfaces frequently act as traps and recombination sites for the electrons. Further, the geometry has undesirable voids from incomplete filling by the organic HTMs in the mesopores of the films [2].

Another serious deficiency is that the perovskite crystals formed by either the planar device or the mesoporous device (TiO_2 nanoparticles) are generally non-uniform in size with numerous crystal-crystal interfaces that serve as recombination sites. This has been an unresolved issue. There is a need to develop an effective method to "engineer" crystals that are large and uniform size having high crystallinity that improved light harvesting.

Instead of nanoparticles, one-dimensional (1D) nanostructures/nanofiber network have also been used [2, 3]. Moreover, the 1D nanostructures provide a direct path for transport of photo-generated electrons. This solution provides both improved charge transport and reduced electron-hole recombination [3, 4]. Recently, there were various studies related to using TiO_2 nanowires [5, 6], nanorods [3, 7-9], nanotubes [10, 11], and nanocones [12] as the scaffolds for PSCs. While these are known, what is yet addressed is developing an effective approach to grow large and uniform crystals for use in PSC device!

Here, we have developed an effective method to engineer large, uniform perovskite crystals by using in a uniform, structured thin TiO_2 nanofiber scaffold layer. Further, we ensure large quantity of photogenerated charges can be conducted efficiently by embedding graphene in these nanofibers to greatly enhance their charge conductivity. The application for perovskite solar cell and functional working mechanism of this novel nanofiber scaffold layer will be investigated in the present study. Deploying nanofibers as PSC scaffold has not been studied extensively to our knowledge. Dharani et al. [4] has used TiO_2 nanofibers scaffold to fabricate the PSC device but with a disappointing power conversion efficiency of only 9.8%. This is because their scaffold layer is too thick, as a result there are too many intersections among the nanofibers which may result in numerous small crystals growing from these junctions and non-uniform crystal layer. Subsequently, there has been virtually nil study along this direction due to the early disappointing results.

1D nanofibers can be fabricated by using electrospinning which is a relatively simple and low-cost technique. The research of dye-sensitized solar cells (DSSC) showed that the long and interconnected nanofibers is a good substitute for the mesoporous nanoparticles [13-15]. In our previous study [16], we mixed pure graphene nanofibers with MAI, and the mixture was added to the precoated PbI_2 layer. The graphene nanofiber surface provided surface for seeding of crystals. The crystals grew on the periphery of the nanofibers. The crystal size was not controlled. Further, the graphene nanofibers in the perovskite layer can be randomly distributed, resulting in clusters of crystals in region where nanofibers were located, especially at the junction of fibers. The crystallization process in the perovskite layer is somewhat unregulated.

As a departure from the previous approach of growing crystals on graphene nanofiber periphery that result in uncontrolled crystal size; here, we develop structure nanofibers scaffold layer that facilitate the formation of large and uniform crystals and smooth layer perovskite layer. Unlike previous approach [16], these crystals do not contact any graphene surface for seeding/nucleation. One of the interesting issues is to establish the feasibility of this approach. To summarize, there are a total of four issues that will be addressed in this study. The first issue is to develop structured nanofiber scaffold layer. The second issue is to grow large and uniform crystals over the structured nanofibers scaffold layer. The third issue is to be able to quantify the enhanced crystallinity and light absorption properties of the resultant perovskite crystals. The fourth issue is to improve the conductivity of the semiconductor nanofiber scaffold so that the large amount of photogenerated electrons can be transported effectively to the electrode.

It is known that graphene-derived nanomaterials facilitate high conductivity and serve as excellent interfacial electrical contact. As such, they are good candidates for deploying in PSC for optimizing the efficiency of the cells. So far, the graphene-derived nanomaterials have been used in various interfaces, such as rGO being used in compact TiO_2 layer, rGO in mesoporous TiO_2 nanoparticle layer or in HTL [17-20]. However, there is virtually little to nil study about the application of TiO2 nanofibers with embedded graphene for the PSCs to improve the nanofiber charge conductivity. What is the genuine function of this new configuration for the PSC? Do the nanofibers embedded with highly conductive graphene provide more efficient electron/charge transport, thereby reducing recombination? What is the optimal graphene size and amount in the nanofibers to improve the performance of the PSC device in terms of PCE, FF, and J_{sc}? These interesting issues will be addressed in this investigation.

In this chapter, an optimal-thickness TiO_2 nanofibers scaffold layer with large, uniform pores is used for growing crystals. In the nanofiber scaffold, adjacent nanofibers are oriented parallel to each other by use of two closely spaced disks as the target for the electrospun nanofibers during electrospinning. The pore/opening geometry in the nanofiber mat is not perfectly rectangular, but approximately polygon-shape, and of uniform size. An important parameter is the electrospinning time in affecting the size, uniformity of the pores and the number of the intersections of the nanofibers. Short electrospinning time produces ultra-thin scaffold which is ineffective with irregular pore, while too long electrospinning time produces a thick scaffold with small, non-uniform size pores and too many nanofibers intersections that restrict crystal size which is the shortcoming of the earlier work [4] resulting in relatively lower efficiency (less than 10%) for the PSC. The present approach guarantees large, uniform crystals to be formed. Therefore, an optimal scaffold thickness is required which requires to be determined from the experiments.

One further enhancement on the TiO_2 nanofibers mat is to embed graphene in a roll-up form in the nanofibers. This is because when 2D graphene sheets are used instead, electrons/charges can migrate to the edge of the graphene sheet and recombine with the holes. However, when the graphene sheets are rolled up, this eliminates the free edges and electrons are forced to travel along the axis of the roll-up graphene sheet. Given the graphene roll is inside the TiO_2 nanofibers, the charges are transported along the TiO_2 nanofibers in the graphene core.

There are two major benefits with this new configuration. First, the intersections of the nanofibers provide sites for nucleation of perovskite crystals and the thin structured nanofibers may control the growth of the perovskite crystals, these can help to form uniform, large perovskite crystals with reduced interface. This produces crystals with excellent crystallinity and can harvest more light. Further, the reduced crystal-crystal interface and the minimization of unreacted PbI_2 both reduce recombination sites resulting in much higher FF. Second, the TiO_2 nanofibers with embedded graphene can improve the charge transport property resulting in increased V_{oc} and J_{sc}. With this approach, the resulting device exhibits the best PCE of 19.30%

under AM1.5G standard solar simulation as compared to the reference PSC cell with PCE of 17.46%. This is an 11% performance improvement above and beyond the reference PSC device without the scaffold.

5.2 Experimental Details

5.2.1 Synthesis of TiO_2 nanofibers and TiO_2 nanofibers with embedded graphene

Using the methods which are shown in Chapter 2 to prepare the graphene precursor solution and fabricate the nanofibers.

The methods of preparation of substrate and ETL, synthesis of $PbI_2(DMSO)_x$ Complex, fabrication of perovskite layer and HTL preparation are same as that in Chapter 3. In this study, gold was used for the thermal evaporation.

5.3 Results and Discussion

5.3.1 Morphology and crystallization of perovskite layer

Figure 5.1 (a), (b) show the idealized model of the structured scaffold layer, from simple to more complex geometry, that can help to grow large perovskite crystals and with good crystal uniformity. Consider Figure 5.1 (a), the vertical nanofiber “a” provides nucleation site for the perovskite crystals, and a crystal grows with front advancing left and right of the nanofiber a. Likewise for the adjacent nanofiber “b”, a crystal also grows advancing left and right of that fiber. At the mid-plane between nanofibers “a” and “b”, it serves as the edge of the two crystals. In Figure 5.1b, nanofibers “A”-“D” and nanofibers “a”-“d” represent, respectively, the horizontally and vertically oriented TiO_2 nanofibers in an idealized “square grid” arrangement. Crystals nucleate and grow from segment between Node 4 and Node 8 of nanofiber “B” upward and downward, respectively in Figure 5.1 (b); and from nanofiber segment between Node 2 and Node 6 of nanofiber "C" horizontally left and right, respectively. The net effect is that by symmetry of the geometry, the crystal growth is extended radially outward from Node 0. Similarly, from any intersection of nanofibers other than Node 0, crystal grows from the intersectin of nanofibers and the geometric center of the pores/openings become the vertices of the boundary for the crystals. For example, the vertices for Crystal 1 are Nodes 1, 2, …, 7, 8 as shown in Figure 5.1 (b). Similarly, we have Crystal 2, Crystal 3 (not shown), etc.

The yellow dot lines in the Figure 5.1 (b) show the boundaries of the perovskite crystals formed using this model. We try to produce evenly-spaced, parallel nanofibers in both horizontal and vertical directions, so that the opening between the fibers is square or rectangular. In real situation, the openings are more polygon-shaped. Despite this, large uniform crystals can still form at the nanofiber intersections with vertices located at the center of the openings. As can be seen, the structured nanofibers scaffold is important to regulate large, uniform crystals to be formed in the perovskite layer.

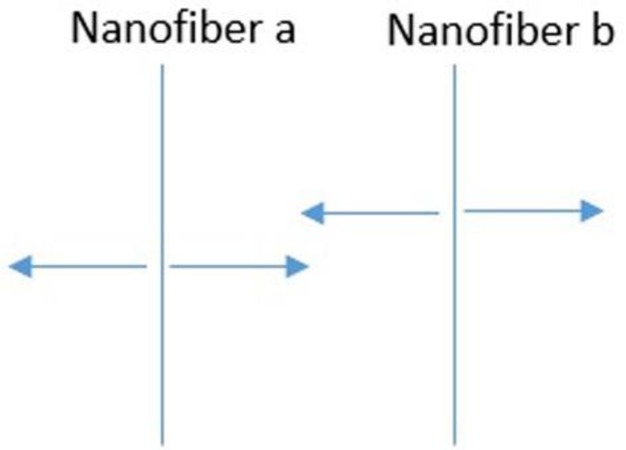

(a)

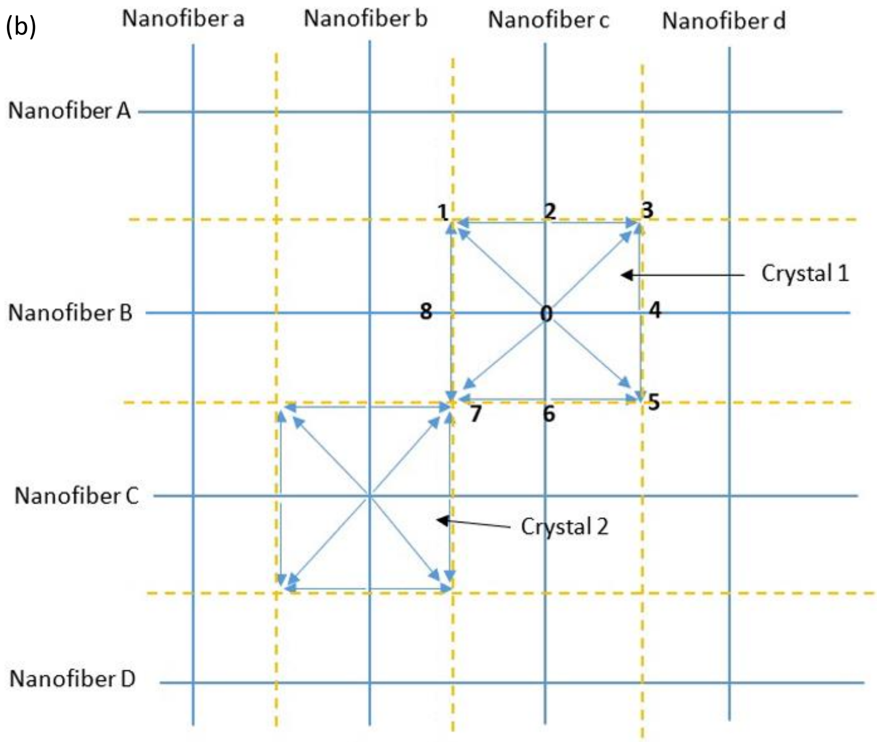

Figure 5.1 The idealized model of the formation of perovskite crystals on the structured TiO_2 nanofibers scaffold layer.

Raman spectra measurement was used to estimate the existence of graphene in the TiO_2 nanofibers. Figure 5.2 shows the Raman spectra of the TG nanofiber. The insert diagram in the figure reveals that there are two peaks approximately 1352 and 1573 cm^{-1} in the TiO_2/embedded graphene nanofibers spectrum, corresponding, respectively, to the D peak associated with edge defects and the G peak associated with the highly ordered graphite. The 2D peak is located at approximately 2717 cm^{-1}. The morphology and thickness of the graphene sheet can be reflected by the intensity and shape of this peak. The high-quality graphene embedded in the nanofibers can be revealed by the symmetrical profile of the peak with respect to the center axis drawn through the peak.

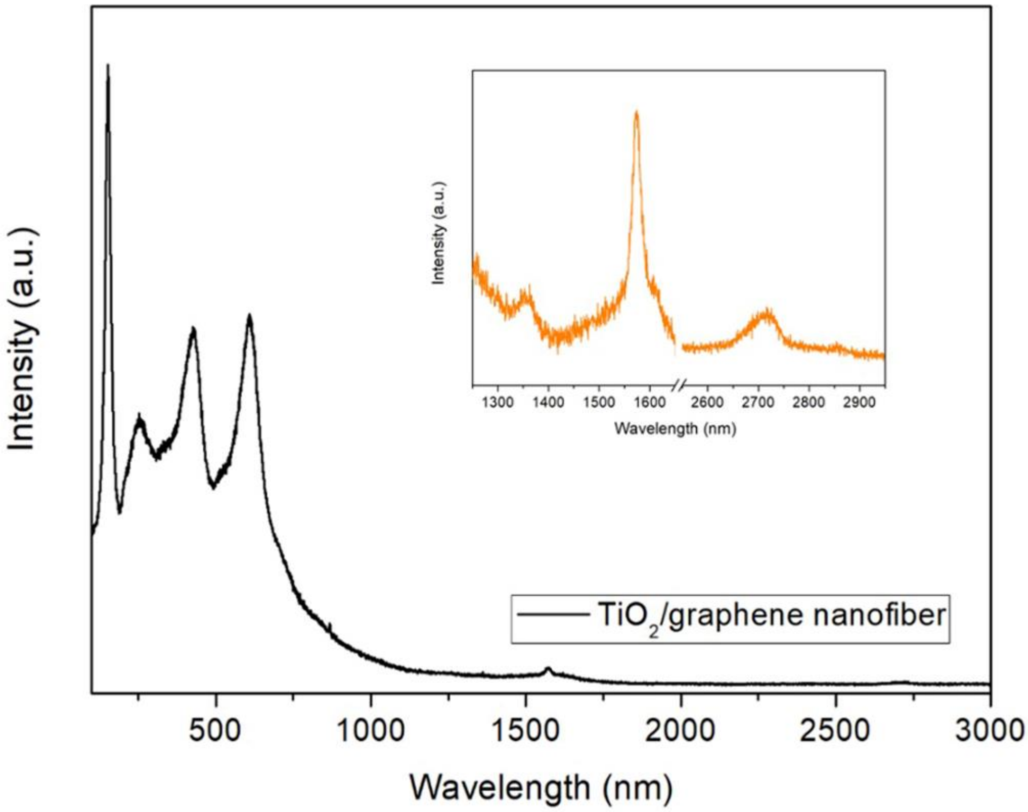

Figure 5.2. Raman spectra of TG nanofibers.

Figure 5.3 (a) shows the SEM images of a thin structured nanofibers scaffold layer that was formed on the TiO_2 compact layer that was coated on the FTO glass. The average diameter of the nanofibers is about 80 nm as determined from Figure 5.3 (a). Too long electrospinning time produces a thick electrospun scaffold with too many nanofibers intersections and non-uniform pores, while too short electrospinning time produces irregular pores. By controlling the appropriate electrospinning time, the scaffold layer thickness can be optimized to produce evenly spaced nanofiber intersections with large uniform pores between nanofibers. Our larger pore size facilitates penetration of the perovskite precursor solution deep into the pores, thereby enabling better contact and adhesion between the perovskite crystals and the TiO_2 dense layer [21]. The large pores also benefit good contact, and therefore complete reaction, between the PbI_2 (inorganics) introduced first in the pores and the MAI (organics) introduced subsequently into the pores to react with the PbI_2. Consequently, the unreacted PbI_2 is being reduced, as will be seen later. Based on the aforementioned model, the “white dots” shown in Figure 5.3 (b) locate the center of the pores between nanofibers, which are also the vertices of the boundary for the crystal. By connecting the vertices wrapping around the nanofiber intersection, we can define the geometry of the model crystal. Two such crystals are shown in Figure 5.3 (b). Figure 5.3 (c) illustrates all the model crystals that are defined by boundaries drawn between predetermined vertices (located at center of the pores/openings) with crystal centered at the nanofiber intersections. For sufficient large crystals, two or more crystals can be formed or split up from one large, single crystal. Figure 5.3 (d) shows the actual real crystals that were obtained. As seen in Figure 5.3 (d), the crystals are quite large and uniform. To determine the effective size of the crystal, an imaginary rectangle with length a and width b is being fitted to the polygon-shaped crystals, so that they have the same area as the imaginary rectangle. The equivalent size is defined as the geometric mean of these two dimensions $\sqrt{ab}$. This approach is used to determine the size distribution of the model crystals in Figure 5.3 (c) as well as the size distribution of actual crystals shown in Figure 5.3 (d). The comparison between these two distributions are depicted in Figure 5.3 (e). The size of the actual crystals is concentrated in the range 0.9-1.4 micrometers, which compares well with the size of the model crystals that are concentrated in the range 1.0-1.7 micrometers. This demonstrates that uniform crystals of the prescribed size to be formed for the perovskite harvesting layer can be engineered using an optimized nanofiber scaffold approach and can be reasonably modelled. Further, the optimized nanofiber scaffold approach also reduces the formation of smaller crystals that increase the interface and recombination sites.

In contrast without the scaffold, as shown in Figure 5.3 (f) the perovskite layer is not as uniform and smooth as that shown in Figure 5.3 (d), and there are much more small spiculate stuff. The absence of the spiculate using the present approach is attributed to the uniform spaced scaffold providing seeding/nucleation and crystallization of the perovskite crystals facilitating the complete reaction of PbI_2 with MAI to $CH_3NH_3PbI_3$.

The amount and quality of the graphene in the TiO_2 nanofibers is well controlled by the centrifugation time on the precursor suspension with graphene for electrospinning. when the centrifugation time on graphene precursor suspension is too short, say 3 min, there are too many large graphene sheets remaining in the supernatant and these cannot be incorporated/embedded inside the nanofibers. As a result, exposed graphene flakes can be seen in Figure 5.3 (g), which indicates excessive graphene in the TiO_2 nanofibers.

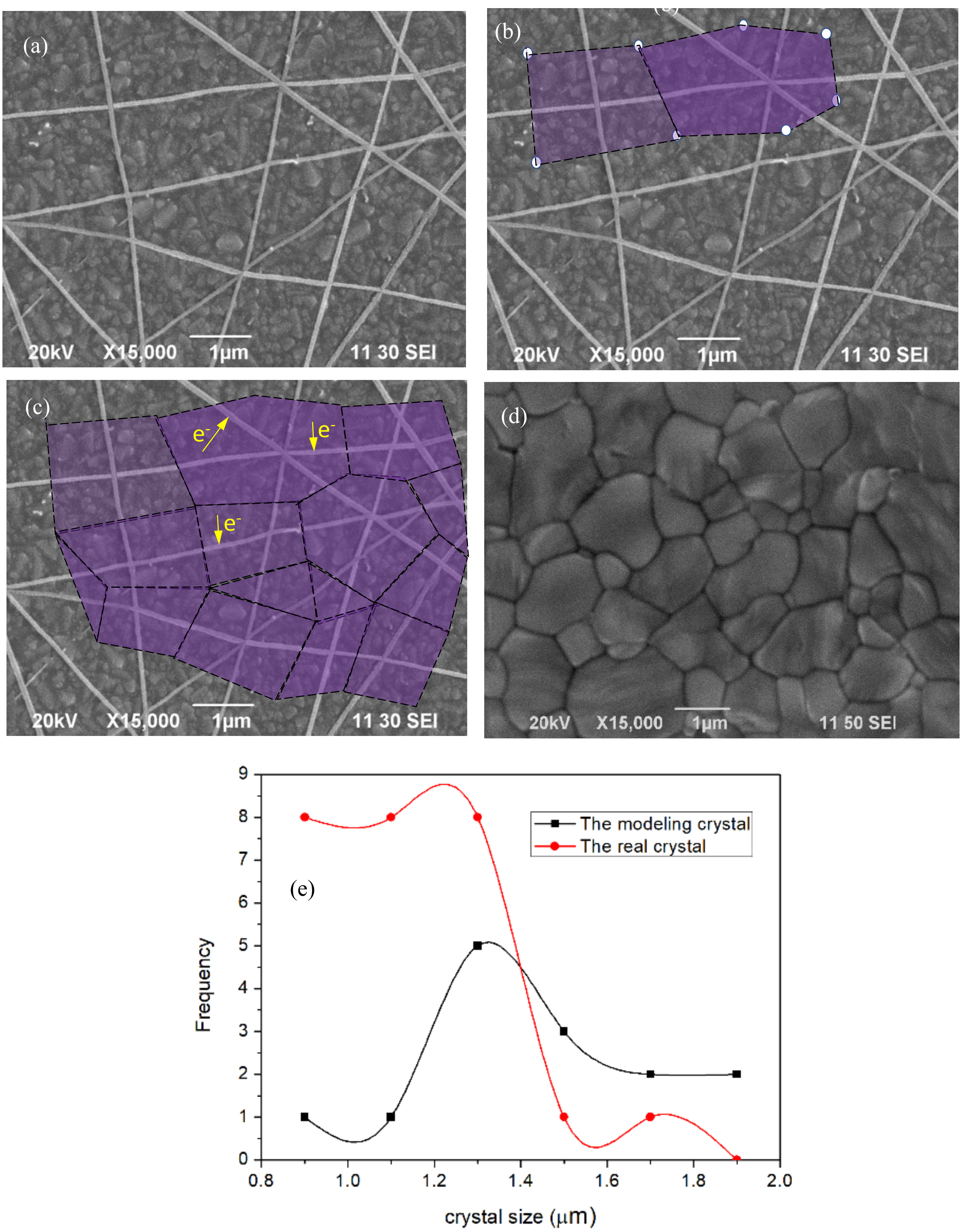
(a)
20kV X15,000 1μm 11 30 SEI
(b)
20kV X15,000 1μm 11 30 SEI
(c)
e-
e-
e-
20kV X15,000 1μm 11 30 SEI
(d)
20kV X15,000 1μm 11 50 SEI
(e)
The modeling crystal
The real crystal
Frequency
0
1
2
3
4
5
6
7
8
9
crystal size (μm)
0.8
1.0
1.2
1.4
1.6
1.8
2.0

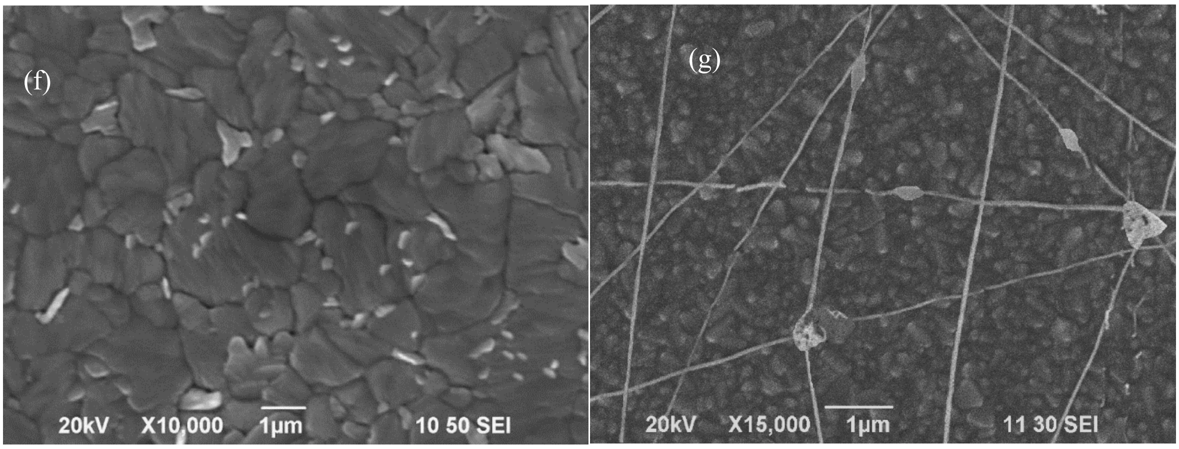

Figure 5.3 (a) SEM image of the TG nanofibers (graphene precursor solution centrifuged 5 min). (b) Define vertice of polygon at center of opening between nanofibers. (c) Crystals boundary based on vertices of the openings with crystal wrapping about crisscross nanofibers. (d) SEM image of perovskite layer with TG nanofiber scaffold. (e) Comparing the size of actual perovskite crystals and the modelling crystals. (f) SEM image of perovskite layer without TG nanofiber scaffold. (g) TG nanofibers (graphene precursor solution centrifuged 3 min).

On the other hand, the small spiculate stuff without the scaffold approach might have been the PbI_2 that has yet been left without reacting with MAI to form $CH_3NH_3PbI_3$ [1]. This unreacted PbI_2 in the conventional approach (without scaffold) leads to electron-hole recombination at these sites, which can be seen in the XRD patterns of the perovskite layers in Figure 5.4. From Figure 5.4, indeed we can see that for the sample without TG nanofiber scaffold, the XRD pattern of the perovskite layer show weak peaks of the PbI_2 which indicates that not all the PbI_2 has been chemically reacted to form $CH_3NH_3PbI_3$. In contrast, the sample with TG nanofibers scaffold do not have such peaks confirming full transformation of PbI_2 to $CH_3NH_3PbI_3$. Comparing the areas of the main peak (110) of $CH_3NH_3PbI_3$ in Figure 5.4 for the devices with/without TG nanofibers scaffold, we can see that the area for the perovskite with TG nanofibers scaffold (1251.7) is at least 5 times larger than that without scaffold (232.7) which implies the perovskite layer formed by the TG nanofibers scaffold has much higher crystallinity, which agrees with the nice morphology of the perovskite crystals obtained by the scaffold approach.

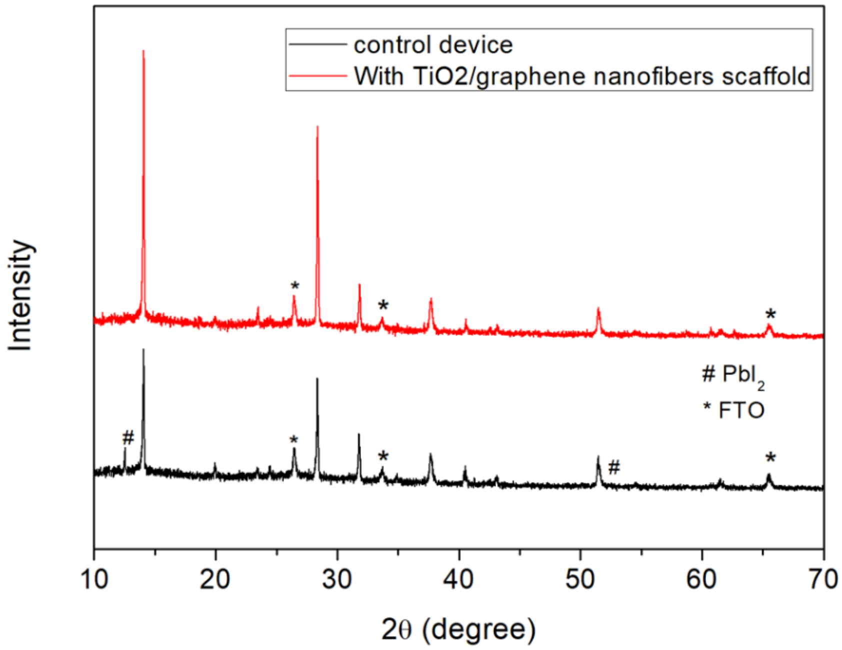

Figure 5.4. XRD patterns of the perovskite layers with and without TiO_2/graphene nanofibers scaffold

Further, the more uniform perovskite layer with large crystals helps to harvest more light across the entire light spectrum from 350 to 800 nm. This is further confirmed by the UV−vis absorbance spectra as shown in Figure 5.5. On contrary, too thick a nanofiber scaffold creates too many nanofiber intersections due to random laying of the non-woven nanofibers stacking on top of each other, resulting in small and non-uniform sized crystals, which have low crystallinity and low light harvest property. This also explains the poor performance reported with earlier work [4] In addition, in earlier work [4] there was no embedded carbon or graphene in the nanofibers to improve charge conductivity as discussed later.

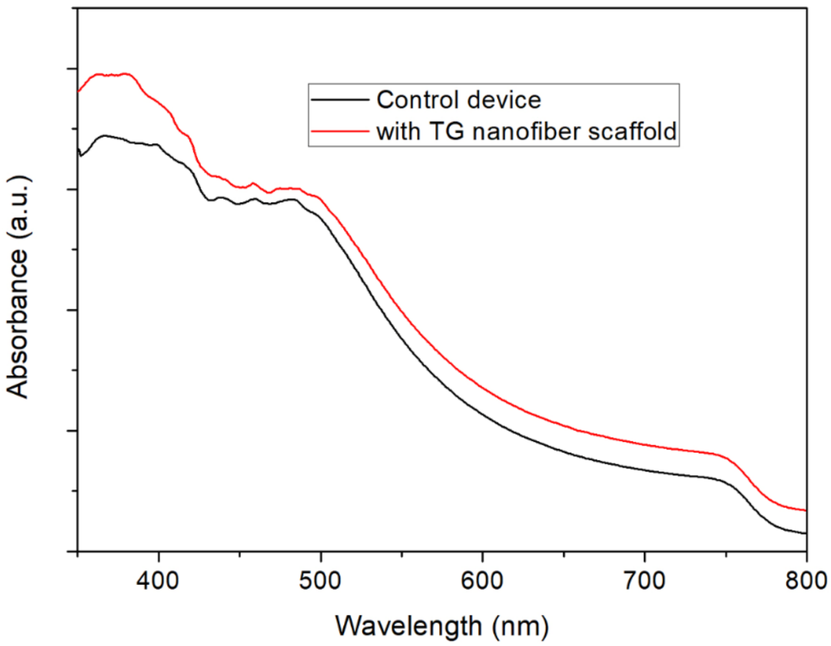

Figure 5.5. UV−vis Absorbance Spectra.

5.3.2 Photovoltaic performance

The best performance based on current density−voltage (i.e. J−V curves) of the devices for PSC devices, respectively, with the planar structure without scaffold (control), TiO_2 nanofiber scaffold, and TG nanofibers scaffold produced using different centrifugation times controlling the graphene in the scaffold nanofibers is shown in Figure 6.6. As can be seen, when only TiO_2 nanofibers scaffold was used, performance of the device was improved as compared with the device without scaffold (control). This is due to the fact that the structured TiO_2 nanofibers mesoporous layer can help to form more uniform and smoother perovskite layer with large crystals as described by Figure 5.3 (b) and (c). Furthermore, the TiO_2 nanofibers scaffold can also provide a direct path for the electrons to be transported. This can be seen in Figure 5.3 (c) as well as the transport property improvement as demonstrated in the IMPS test results to follow. More importantly, large, uniform crystals form in the nanofiber scaffold that reduces recombination from excessive interfaces due to small and non-uniform sized crystals. However, the transport of charges along TiO_2 semiconductor nanofibers is not as efficient as with nanofibers that are highly conductive, e.g. carbon nanofibers. This shortcoming can be compensated by use of graphene embedded in the TG nanofibers scaffold. This can be seen by the J_{sc} in Figure 5.6 for the 3-min and 5-min TG nanofiber curve both of which are greater than those with the control and the TiO_2 nanofiber scaffold. The TiO_2 nanofiber scaffold provide large, uniform crystals with high crystallinity which is excellent for light harvest while the graphene embedded in the nanofibers assist in the charge transport boosting the short circuit current. Therefore, it is expected that the PSC with the TiO_2 nanofiber scaffold with embedded graphene out-performs that with the TiO_2 nanofiber scaffold without embedded graphene due to improve charge transport. While the PSC with the TiO_2 nanofiber scaffold without embedded graphene out-performs the planar PSC device without the scaffold due to larger and more uniform crystals of the former that harvest more light and reduce recombination with less crystal boundaries and unreacted PbI_2.

When the centrifugation time was decreased from 20 to 5 min, the graphene in the supernatant was higher, implying the concentration of graphene in the formed nanofibers were higher as well. This leads to better performance of the PSC device. Therefore, at relative low graphene concentration, increasing the amount of graphene in the scaffold layer improved the charge collection efficiency. However, when the centrifugation time on graphene suspension further decreased from 5 to 3 min, resulting in even higher concentration of graphene in the nanofibers, the efficiency of the device ultimately decreased. This is because excessive graphene in the TiO_2 nanofibers acted as recombination sites for the electrons, which ultimately reduced the FF. The content of graphene in the TiO_2 nanofibers under different centrifugation time was estimated by using thermogravimetric analysis (TGA). The only volatile species in the nanofibers was graphene in the measurement. Figure 6.7 shows the TGA results of the TG nanofibers with different centrifuge time on the graphene precursor suspension. The TGA showed a single-step decomposition of the nanofibers. The decomposition of all the samples was completed at the same temperature of 1000℃. The mass-loss of the samples under the centrifugation time 20 min, 5 min and 3 min was 19.77%, 8.46% and 3.10% respectively.

From Figure 5.6, it is evident that the most optimal condition corresponds to the case with centrifugation time of 5 min with 8.46% graphene in the TiO_2 nanofibers, for which the maximum PCE reached 19.30% with J_{sc} of 24.06 $mA \cdot cm^{-2}$, V_{oc} of 1.08 V, and FF of 75%. The parameters corresponding to the best performance for all the conditions are summarized in Table 5.1, while the parameters corresponding to the average performance are tabulated in Table 5.2. Comparing the data in Table 5.1, the device performance parameters, V_{oc}, J_{sc}, FF, and PCE at the optimal condition with TG nanofibers scaffold (i.e. produced with centrifugation time of 5 min) are all higher than that for the control device. Specifically, both J_{sc} and FF have been improved dramatically due to 1D charge transport using graphene and the large crystals minimizing interfaces with consequence of reducing recombination. As a whole, the final PCE has been raised by 11% as compared to that of the control device without TG nanofiber scaffold. It is evident that the more uniform and smoother perovskite layer leads to much higher FF. Meanwhile, the increased J_{sc} and V_{oc} are primarily due to the embedded graphene in the TiO_2 nanofibers scaffold, which enhances the charge carrier transport property. Figure 5.8 (a), (b) show the J-V curves in reverse and forward sweeps for the perovskite layers with and without TG nanofibers, respectively. It can be seen that the use of TG nanofibers scaffold for the device further facilitates reduction in the hysteresis, which is advantageous. The external quantum efficiency (EQE) results are shown in Figure 5.9. The use of TG nanofibers scaffold for the devices can also improve the performance of EQE, especially at wavelengths less than 750 nm. This is consistent with the increased absorbance as shown in Figure 5.5.

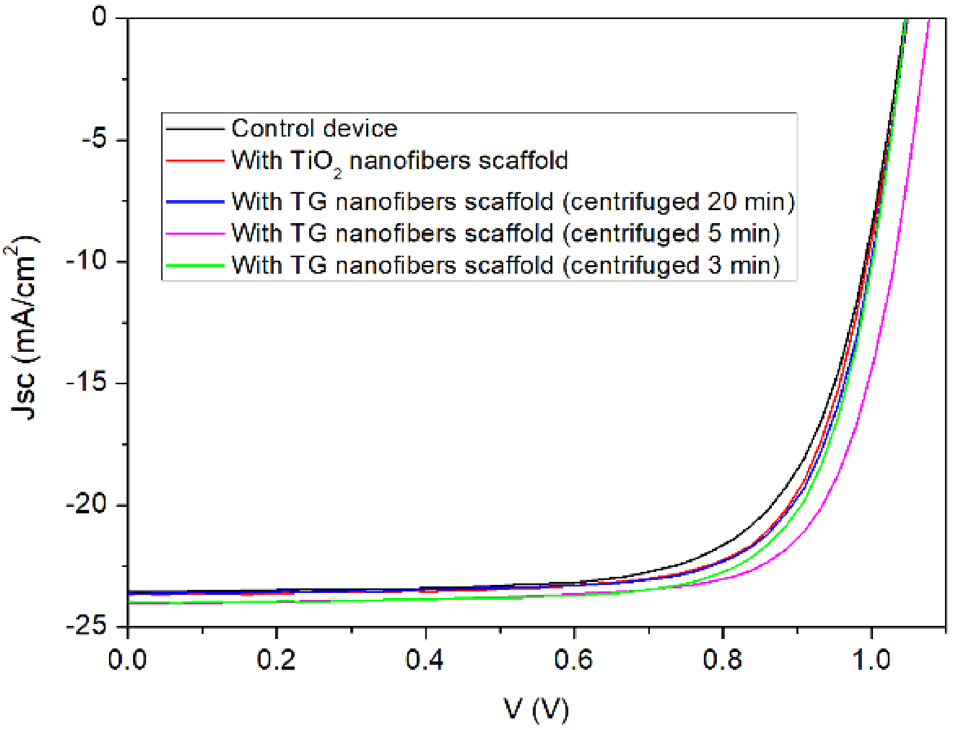

Figure 5.6 J–V curves measured under 100 mW·cm^{-2} AM1.5G illumination.

Table 5.1 Best performance of the Perovskite Solar Cells under AM 1.5 G illumination

	V_{oc} (V)	J_{sc} (mA/cm^2)	FF(%)	PCE (%)
Control	1.05	23.54	71	17.46
TiO2 nanofibers scaffold	1.05	23.66	73	18.12
TG nanofibers scaffold (centrifuged 20 min)	1.05	23.62	73	18.22
TG nanofibers scaffold (centrifuged 5 min)	1.08	24.06	75	19.30
TG nanofibers scaffold (centrifuged 3 min)	1.05	23.96	74	18.60

Table 5.2. Average performance of the Perovskite Solar Cells

	V_{oc} (V)	J_{sc} (mA/cm^2)	FF(%)	PCE (%)
Control	1.00±0.02	23.10±0.31	69±3	17.00±0.25
Graphene suspension centrifuged 20 min	1.03±0.02	23.20±0.25	69±2	17.30±0.31
Graphene suspension centrifuged 5 min	1.06±0.02	23.73±0.22	71±2	18.50±0.23
Graphene suspension centrifuged 3 min	1.02±0.02	23.32±0.26	70±1	17.80±0.30

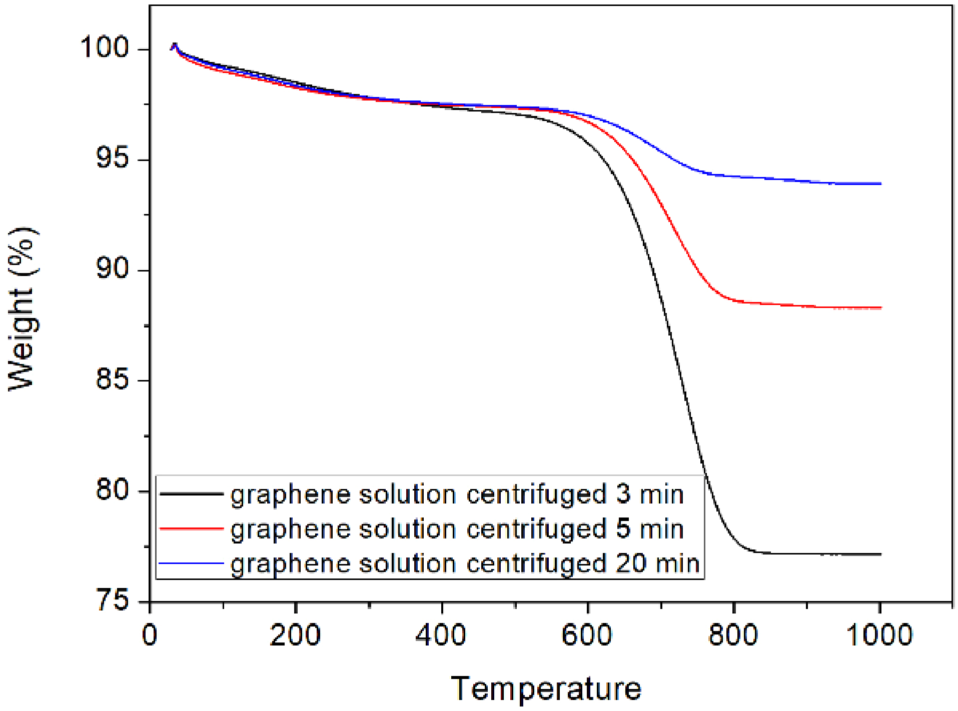

Figure 5.7 TGA of the TG nanofibers with different graphene suspension centrifugation time.

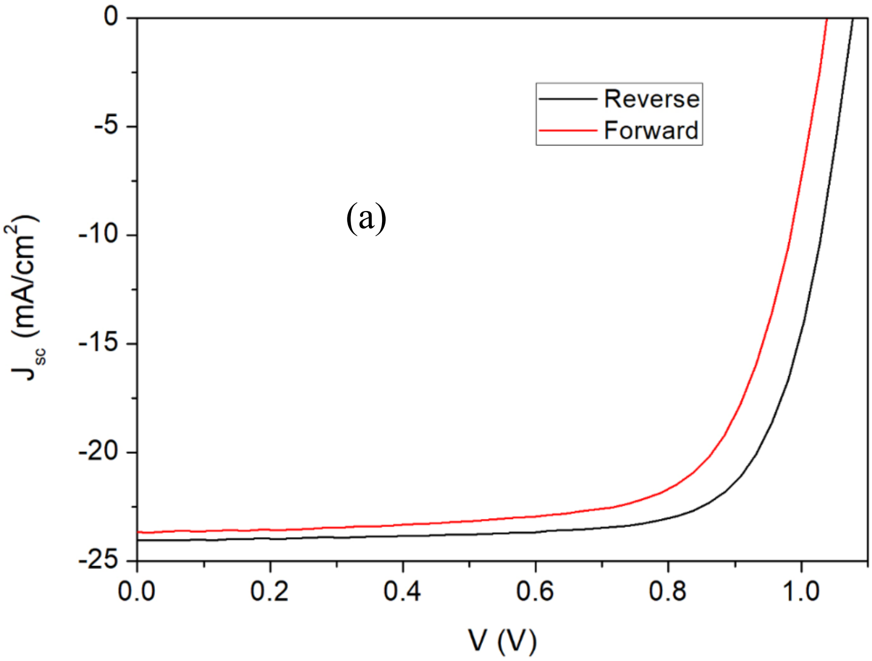

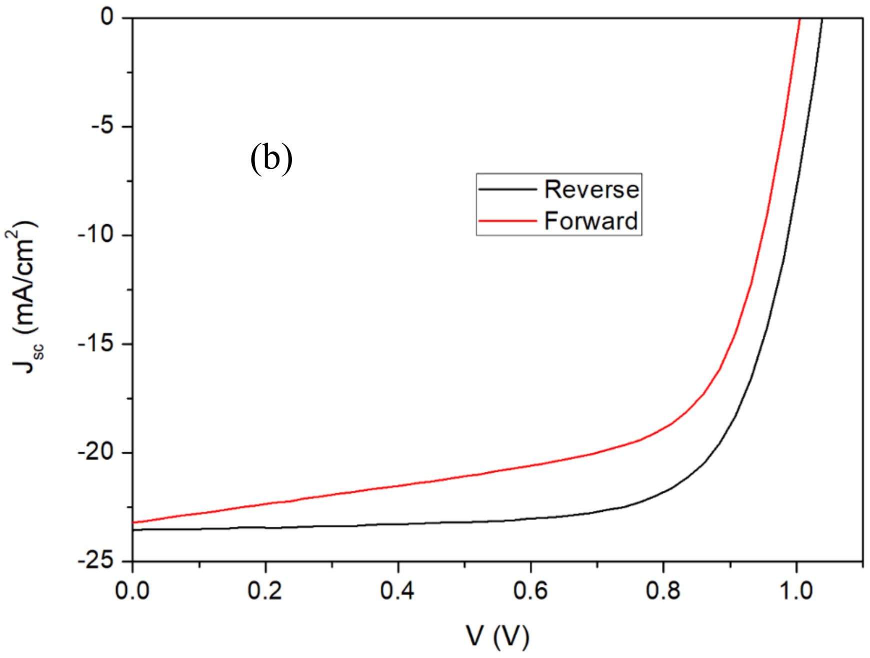

Figure 5.8. J-V curves in reverse and forward sweep (a) sample with TiO_2/graphene nanofibers (centrifuge time 5 min) scaffold; (b) control device.

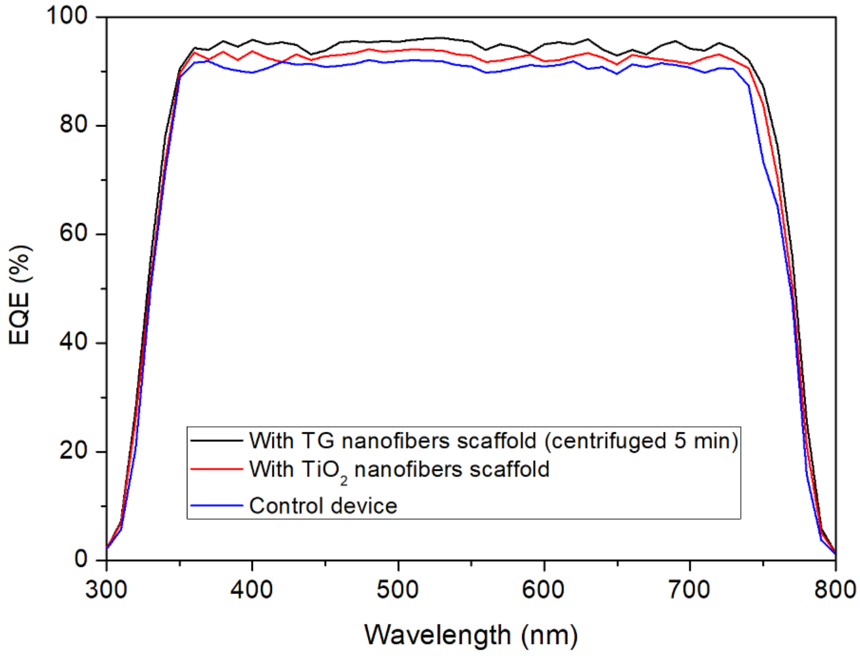

Figure 5.9. External quantum efficiency.

The charge transport time in the solar cells was further investigated IMPS. Figure

5.10 shows the typical Nyquist plots of IMPS response curves of the solar cells for the devices with TiO_2 nanofibers scaffold and with TG nanofibers scaffold produced under different centrifugation times. The charge transport time of the devices under different centrifugation times have been calculated and the results are tabulated in Table 5.3. Figure 5.11 shows the comparison chart of the transport time and PCE for the devices under different configuration times. Indeed, the charge transport time and PCE are very well correlated. When the charge transport time decreases, PCE increases; and vice versa. The best PCE (19.3%) with the lowest charge transport time (0.8 μs) implies the fastest charge mobility. Based on the foregoing discussion, the nanofibers scaffold provides a dedicated path for photo-generated charges to be transported efficiently from perovskite layer to ETL without getting lost and the charge transport time is reduced as compared to the control without the scaffold. Further, when graphene is inserted in the TiO_2 nanofibers to form TG scaffold, the performance is even more superior. Due to the higher conductivity of the TG nanofibers scaffold when compared with only TiO_2 nanofibers scaffold, the TG nanofibers scaffold can further improve the charge transport property for the devices. As a result, the transport time for the TG scaffold is nearly half (=0.8/1.5=0.53) of that of the control device without the nanofiber scaffold and the graphene in the nanofibers.

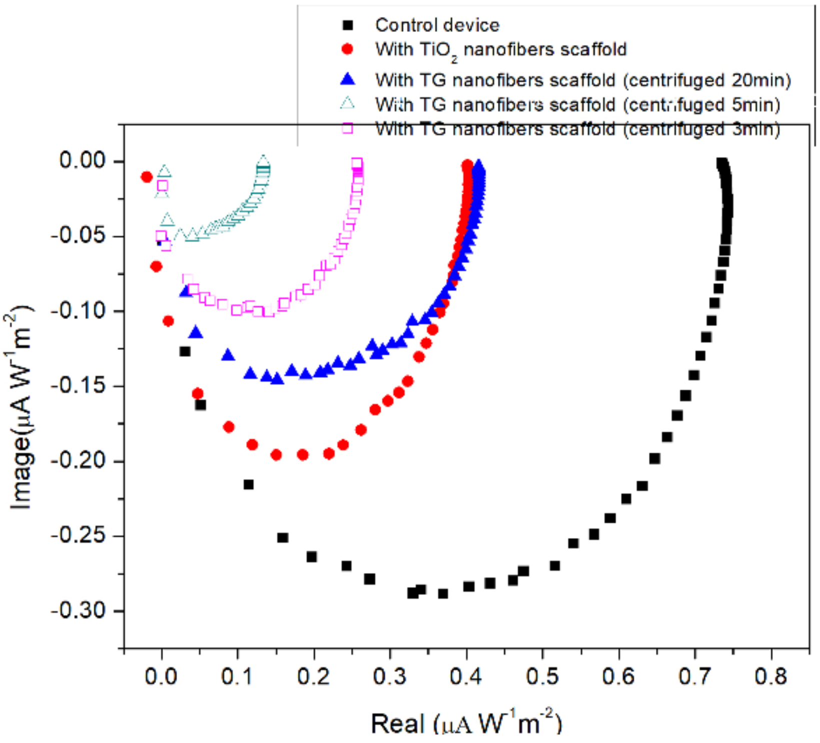

Figure 5.10 Typical IMPS response of the devices under different conditions.

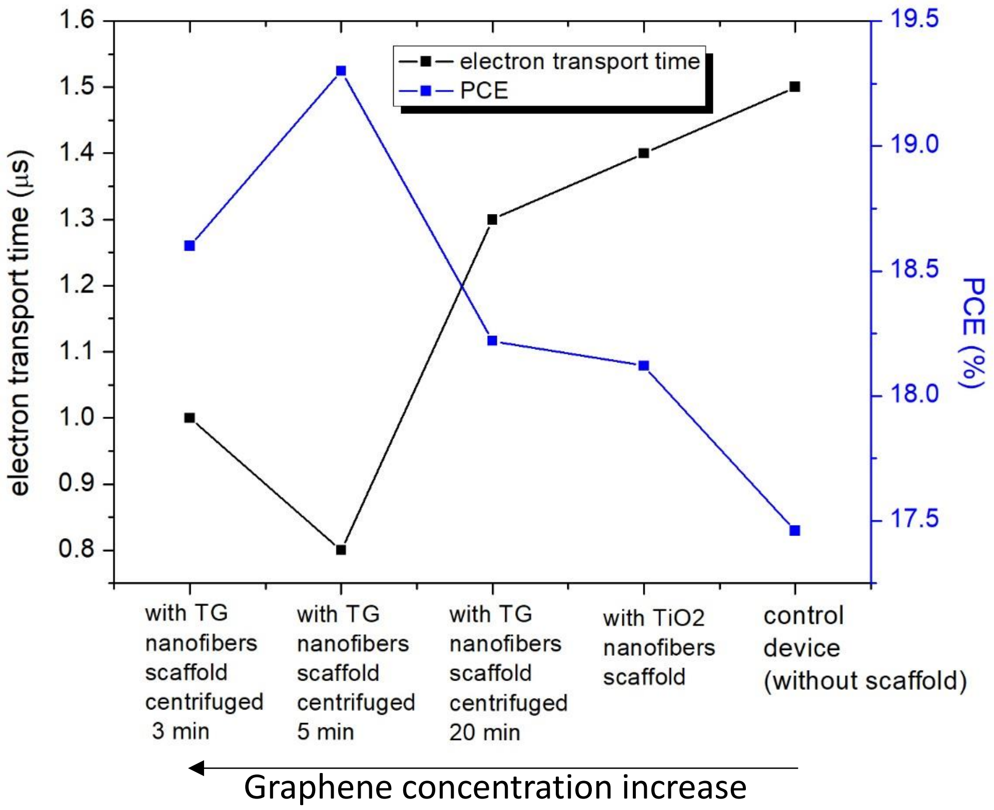

Figure 5.11 Comparison chart of the transport time and PCE for the devices under different conditions.

Table 5.3 The electron transport time with respect to the PCE of the devices.

	charge transport time (μs)	PCE (%)
Control	1.50	17.46
With TiO2 nanofibers scaffold	1.40	18.12
With TG nanofibers scaffold (centrifuged 20 min)	1.30	18.22
With TG nanofibers scaffold (centrifuged 5 min)	0.80	19.30
With TG nanofibers scaffold (centrifuged 3 min)	1.00	18.60

The steady-state PL is shown in Figure 5.12, it is evident that the TiO_2 nanofibers scaffold can facilitate the transport of the electrons from perovskite layer to ETL. When the TiO_2 nanofibers embedded with graphene is adopted as the mesoporous layer, the electrons are transferred even more efficiently. As a consequence, the interfacial recombination rate is much lower for the devices with TG nanofibers scaffold when compared with the other two configurations (i.e. planar device without scaffold and with TiO_2 scaffold alone without graphene), thus the PL intensity is also the lowest under this condition. Figure 5.13 shows the TRPL signal and curve fits are made by using a bi-exponential function. The decay behaviors can be well-modelled. For the devices with the nanofibers scaffold, the PL decay is lower as compared to that without nanofiber scaffold due to less recombination sites with the large uniform crystals having less boundaries/interfaces. For the case with TiO_2 nanofiber scaffold embedded with graphene, the PL decay is further retarded. The longer lifetime of the device with TG nanofibers scaffold is attributed to the improved photoelectronic transport properties.

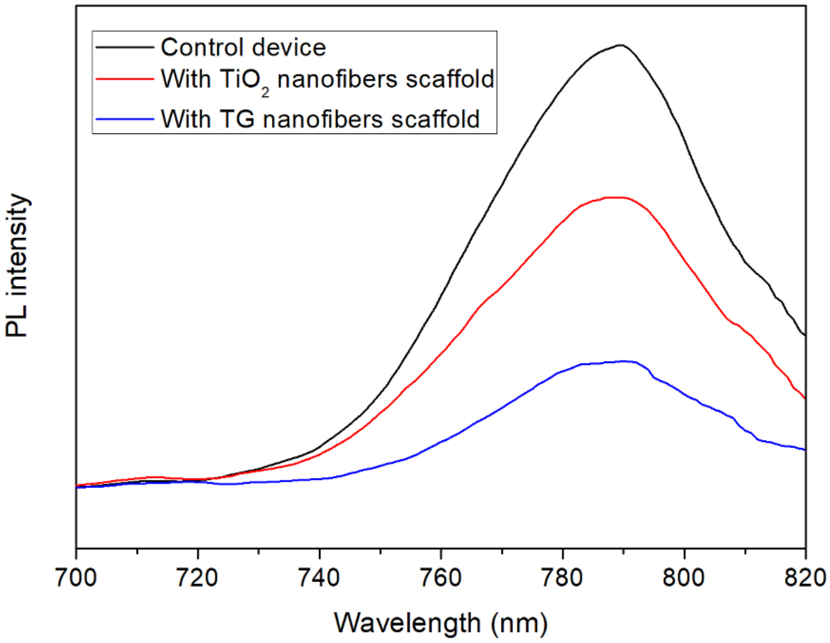

Figure 5.12. Steady-state PL spectra of perovskite films under different conditions.

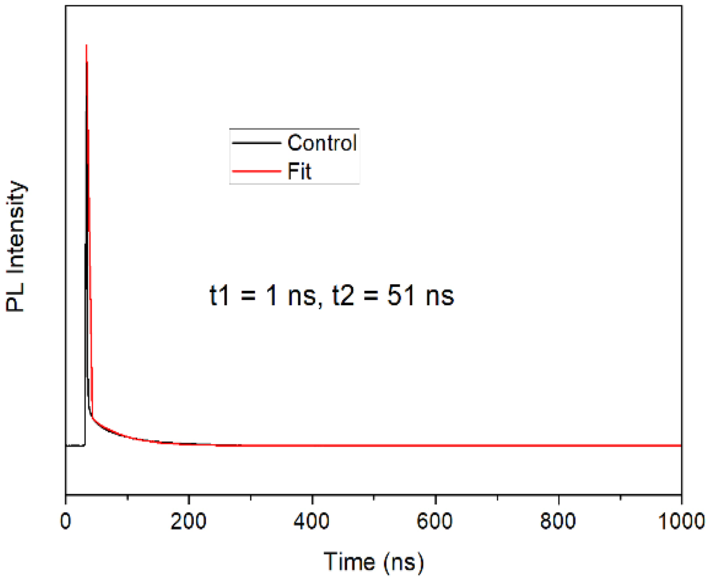

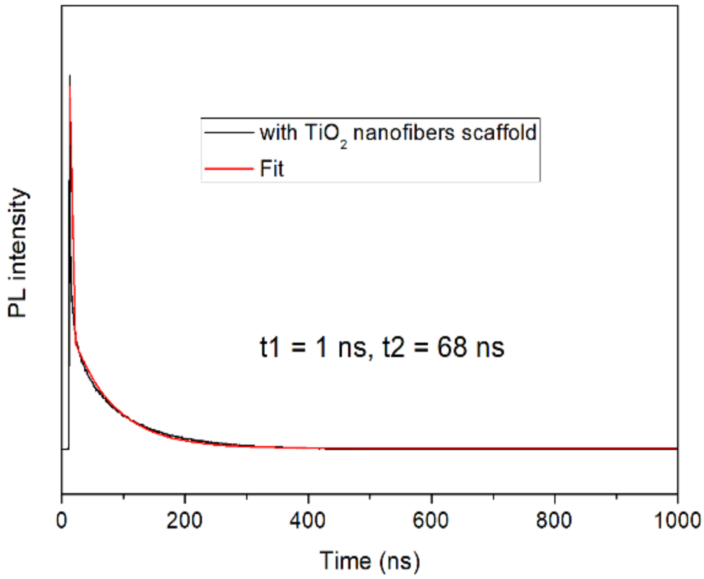

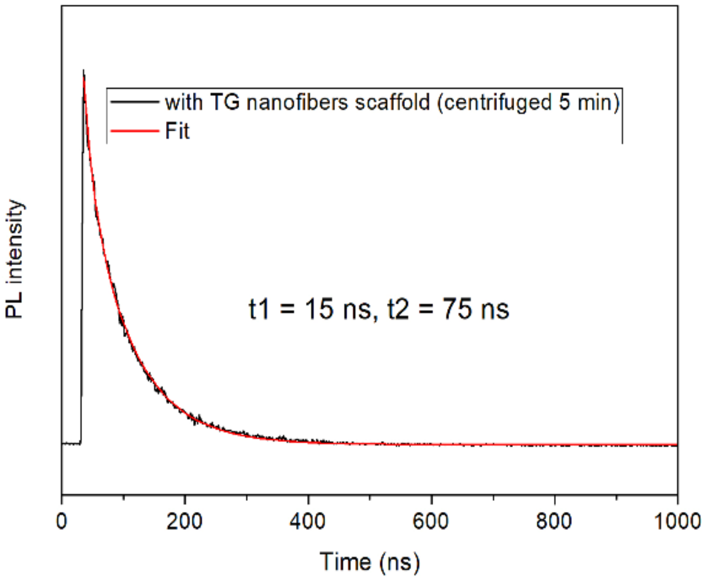

Figure 5.13. The time-resolved photoluminescence of the devices under different conditions (t1 and t2 are the lifetimes associated to the fast and slow recombination, respectively).

5.3.3 Stability test

The stability of the devices fabricated under different conditions has been investigated in this study. The devices were placed under the relative humidity of 85 RH% and room temperature, but without voltage load and constant illumination for a period. The time for the stability test is not irradiation time in the entire period but at three different times, initially, in middle and final time. So the time scale refers to the storage time and not irradiation time. The performance of the devices with TG nanofibers scaffold decreased by 6.5% after 150 h, and by 11% after 300 h; whereas, the devices without scaffold decreases by 10% and 18%, respectively, for the same period. Figure 5.14 shows the trend of the performance changed with the time at 85 RH%. The insert pictures in Figure 5.14 (a) are the slopes of the two curves. It can be seen that the devices with TG nanofibers scaffold have smaller slopes during the test period when compared with that devices without scaffold, which means the application of TG nanofibers scaffold can improve the stability of the device. The other photovoltaic parameters of the devices are shown in Figure 5.14 (b)-(c). Based on all the comparison, the use of TG nanofibers scaffold can improve the stability of the devices. This may be due to the fact that TiO_2 nanofiber scaffold can help to reduce the generation of O^{2-} because of electron injection by TiO_2 [22]. Our previous discussion shows the presence of residual PbI_2 in the perovskite layer for the case without TG nanofibers scaffold, this may also has the negative influence on the device stability which has been estimated by Gujar et al [23].

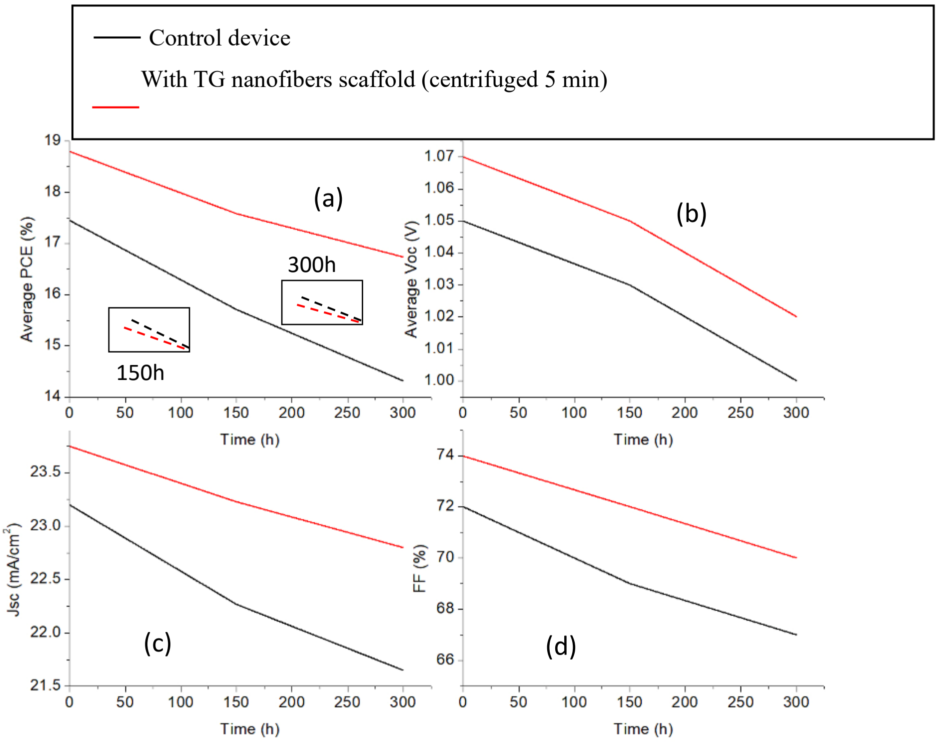

Figure 5.14 Stability on performance of the devices under 85% humidity and at room temperature (The insert pictures in (a) are the comparison of the slopes for the devices with TG nanofibers scaffold (red line) and without scaffold (black line), respectively).

5.4 Conclusions

In conclusion, we have successfully engineered large, uniform perovskite crystals by crystallizing in well-defined structured pores from pre-fabricated thin TiO_2 nanofiber scaffold. The TiO_2 nanofibers in the scaffold are further embedded with graphene for use in the perovskite solar cell to improve charge conductivity. The concentration of the graphene in nanofibers has been optimized by controlling the centrifugation time at high centrifugal acceleration on the precursor suspension containing graphene. The most optimal condition corresponds to the graphene precursor suspension that has been centrifuged for 5 min, which subsequently is used for preparing the TiO_2/embedded graphene precursor solution for electrospinning. Under this optimal condition, the device PCE increased from 17.46% without the scaffold to 19.30% with TG nanofibers scaffold, representing a 11% increase. First, due to the structured nanofibers scaffold, a more uniform and smoother perovskite layer with large grain sizes can be formed, which has excellent crystallinity and light harvesting characteristics. In addition, the unreacted PbI_2, which provides the recombination sites, is reduced. This leads to higher FF and better light harvesting. Second, the much higher J_{sc} and V_{oc} can be attributed to the improved charge transport property by using graphene embedded in the TiO_2 nanofibers scaffold for the devices. The electron transport time for the device with TG nanofibers scaffold is nearly half of that of the devices without the scaffold layer. In summary, an effective method to engineer large, uniform perovskite crystals by crystallizing in pre-fabricated TiO_2 nanofibers and ensuring high conductivity of these nanofibers by embedding graphene has been presented for the first time. The application for perovskite solar cell and functional working mechanism of this novel nanofiber scaffold layer have also been investigated in detail in this study.

References

1. Shi, S., Li, Y., Li, X., Wang, H. *Advancements in all-solid-state hybrid solar cells based on organometal halide perovskites.* Mater. Horiz. 2015. **2**: p. 378.

2. Ye, M., Liu, X. Q., Iocozzia, J., Liu, X. Y., Lin, Z. Q. *Nanomaterials for Sustainable Energy*. Springer, Switzerland, 2016.

3. Kim, H. S., Lee, J. W., Yantara, N., Boix, P. P., Kulkarni, S. A., Mhaisalkar, S., Graetzel, M., Park, N. G. *High Efficiency Solid-State Sensitized Solar Cell-Based on Submicrometer Rutile TiO2 Nanorod and CH3NH3PbI3 Perovskite Sensitizer.* Nano Lett. 2013. **13**: p. 2412.

4. Dharani, S., Mulmudi, H. K., Yantara, N., Pham Thi Thu, T., Park, N. G., Graetzel, M., Mhaisalkar, S., Mathews, N., Boix, P. P. *High efficiency electrospun TiO2 nanofiber based hybrid organic-inorganic perovskite solar cell.* Nanoscale, 2014. **6**: p. 1675.

5. Jiang, Q., Sheng, X., Li, Y., Feng, X., Xu, T. *Rutile TiO2 nanowire-based perovskite solar cells.* Chem. Commun. 2014. **50**: p. 14720.

6. Qiu, J., Qiu, Y., Yan, K., Zhong, M., Mu, C., Yan, H., Yang, S. *All-solid-state hybrid solar cells based on a new organometal halide perovskite sensitizer and one-dimensional TiO2 nanowire arrays.* Nanoscale, 2013. **5**: p. 3245.

7. Zhong, D., Cai, B., et al. *An acid-free medium growth of rutile TiO2 nanorods arrays and their application in perovskite solar cells.* J. Mater. Chem. C, 2015. **3**: p. 729.

8. Fakharuddin, A., Di Giacomo, F., Ahmed, I., Wali, Q., Brown, T. M., Jose, R. *Role of morphology and crystallinity of nanorod and planar electron transport layers on the performance and long term durability of perovskite solar cells.* J. Power Sour, 2015. **283**: p. 61.

9. Mali, S. S., Shim, C. S., Park, H. K., Heo, J., Patil, P. S., Hong, C. K. *Ultrathin*

atomic layer deposited TiO2 for surface passivation of hydrothermally grown 1D TiO2 nanorod arrays for efficient solid-state perovskite solar cells. Chem. Mater. 2015. **27**. P. 1541.

10. Gao, X., Li, J., Baker, J., Hou, Y., Guan, D., Chen, J., Yuan, C. *Enhanced photovoltaic performance of perovskite CH3NH3PbI3 solar cells with freestanding TiO2 nanotube array films.* Chem. Commun. 2014, **50**: p. 6368.
11. Wang, X., Li, Z., Xu, W., Kulkarni, S. A., Batabyal, S. K., Zhang, S., Cao, A., Wong, L. H. *TiO2 nanotube arrays based flexible perovskite solar cells with transparent carbon nanotube electrode.* Nano Energy, 2015. **11**, 728.
12. Zhong, D., Cai, B., Wang, X., Yang, Z., Xing, Y., Miao, S., Zhang, W. H., Li, C. *Synthesis of oriented TiO2 nanocones with fast charge transfer for perovskite solar cells.* Nano Energy, 2015. **11**: p. 409.
13. Sabba, D., Mathews, N., Chua, J., Pramana, S. S., Mulmudi, H. K., Wang, Q., Mhaisalkar, S. G. *High-surface-area, interconnected, nanofibrillar TiO2 structures as photoanodes in dye-sensitized solar cells.* Scr. Mater. 2013. **68**: p. 487.
14. Hwang, D., Jo, S. M., Kim, D. Y., Armel, V., MacFarlane, D. R., Jang, S. Y. *High-Efficiency, Solid-State, Dye-Sensitized Solar Cells Using Hierarchically Structured TiO2 Nanofibers.* ACS Appl. Mater. Interfaces, 2011. **3**: p. 1521.
15. Ahn, S. H., Kim, D. J., Chi, W. S., Kim, J. H. *One‐Dimensional Hierarchical Nanostructures of TiO2 Nanosheets on SnO2 Nanotubes for High Efficiency Solid‐State Dye‐Sensitized Solar Cells.* Adv. Mater. 2013. **25**: p. 4893.
16. Li, Y., Leung, W. W. F. *Introduction of Graphene Nanofibers into the Perovskite Layer of Perovskite Solar Cells.* ChemSusChem, 2018. **11**: p. 1.
17. Han, G. S., Song, Y. H., Jin, Y. U., Lee, J. W., Park, N. G., Kang, B. K., Lee, J. K., Cho, I. S., Yoon, D. H., Jung, H. S. *Reduced Graphene Oxide/Mesoporous TiO2 Nanocomposite Based Perovskite Solar Cells.* ACS Appl. Mater. Interfaces, 2015.

7: p. 23521.

18. Cho, K. T., Grancini, G., Lee, Y. H., Konios, D., Paek, S. H., Kymakis, E., Nazeeruddin, M. K. *Beneficial Role of Reduced Graphene Oxide for Electron Extraction in Highly Efficient Perovskite Solar Cells.* ChemSusChem, 2016. **9**: p. 3040.

19. Feng, S. L., Yang, Y. G., Li, M., Wang, J. M., Cheng, Z. D., Li, J. H., Ji, G. W., Yin, G. Z., Song, F., Wang, Z. K., Li, J. Y., Gao, X. Y. *High-Performance Perovskite Solar Cells Engineered by an Ammonia Modified Graphene Oxide Interfacial Layer.* ACS Appl. Mater. Interfaces, 2016. **8**: p. 14503.

20. Yan, K., Wei, Z., Li, J., Chen, H., Yi, Y., Zheng, X., Long, X., Wang, Z., Wang, J., Xu, J., Yang, S. *High‐Performance Graphene‐Based Hole Conductor‐Free Perovskite Solar Cells: Schottky Junction Enhanced Hole Extraction and Electron Blocking.* Small, 2015. **11**: p. 2269.

21. Huang, A., Zhu, J. T., et al. *Mesostructured perovskite solar cells based on highly ordered TiO\r 2\r network scaffold via anodization of Ti thin film*. Nanotechnology, 2017, **28**: p. 055403.

22. Zhao, X., Park, N. G. *Stability Issues on Perovskite Solar Cells.* Photonics, 2015. **2**: p. 1139.

23. Gujar, T. P., Unger, T., et al. *The role of PbI2 in CH3NH3PbI3 perovskite stability, solar cell parameters and device degradation.* Phys. Chem. Chem. Phys. 2018. **20**: p. 605.

Chapter 6

Reducing Interfacial resistance of charge transport for perovskite solar cell

6.1 Introduction

Enhancing the electron transport property is an important factor for improving the efficiency of the perovskite solar cells. As known the charge carrier transport efficiency is sensitive to both the morphology and the electronic structures of the various interfaces in PSCs [1]. It is essential to reduce the interfacial resistance at the interface, and this is demonstrated herein for the interface between the compact charge transport layer and perovskite layer. This can facilitate the transport of charge carriers across the interface which can become the choke point of the circuit [2-6].

Han et al. used reduced graphene oxide (rGO) / mesoporous (mp)-TiO_2 nanocomposite based mesostructured perovskite solar cells to show that by improving electron transport property at the compact layer/perovskite layer interface, an optimal PCE of 14.5% can be reached [7]. Zhu et al. inserted an ultrathin graphene quantum dots (GQDs) layer between perovskite and the compact TiO_2 layer. The best PCE reached was 10.15% [8]. Could there be any other more conductive materials or other morphological forms of carbon that can provide more efficient transport across such interface? This is the basis of our present study.

As we have seen, the 1D nanostructures, such as nanofibers, can provide a direct path for transport of photo-generated electrons. This solution provides both improved charge transport and reduced electron-hole recombination [9, 10]. Moreover, as known pristine graphene has higher conductivity and less defects. In this study we used an ultrathin layer of pristine graphene nanofibers as the interlayer between ETL and perovskite layer. The pristine graphene nanofibers can by-pass interfacial resistance, thereby facilitating electron transport across the interface of the two layers. In other words, the graphene nanofibers interlayer serves as a bridge across the interface. As a result, J_{sc} can been increased when the graphene nanofibers interlayer has been applied. With this approach, the resulting device exhibits the best PCE of 18.62% under AM1.5G standard solar simulation as compared to the reference PSC cell (without graphene nanofibers interlayer) with PCE of 17.46%. This is a 6.64% performance improvement.

6.2 Experimental Details

6.2.1 Synthesis of pristine graphene nanofibers

Using the methods which are shown in Chapter 2 we have prepared the graphene precursor solution and fabricated the nanofibers.

The methods of preparation of substrate and ETL, synthesis of $PbI_2(DMSO)_x$ Complex, fabrication of perovskite layer and HTL preparation are the same as that in Chapter 3.

6.3 Results and Discussion

6.3.1 Morphology and crystallization of graphene nanofibers

Figure 6.1 shows the SEM image of an ultrathin layer of graphene nanofibers on the TiO_2 dense layer under the best condition (graphene precursor solution centrifuged 60 min). When the centrifuge time is too long, the majority of graphene sheets have been centrifuged out and this cannot have a significant effect on the charge transport across the compact layer-perovskite layer interface. However, when the centrifuge time is too short, there are too many large graphene sheets remaining in the supernatant and these cannot be entirely incorporated/embedded inside the nanofibers. As a result, exposed graphene flakes may act as the recombination sites for the charge carriers.

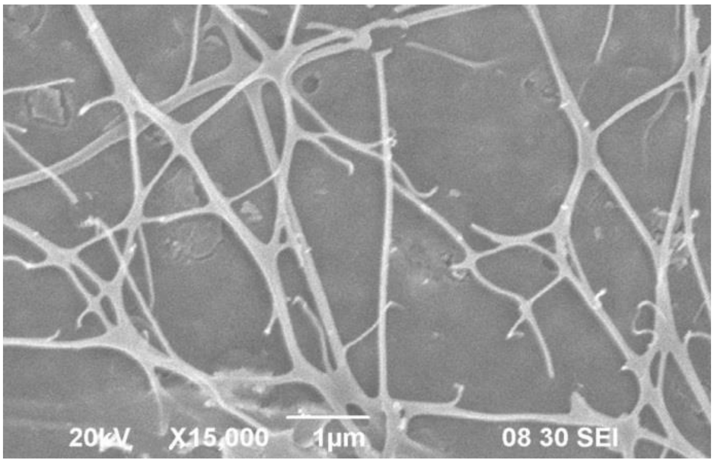

Figure 6.1. SEM image of the graphene nanofibers (centrifuged 60 min) on the TiO_2 dense layer.

We have used the Raman spectrum measurement to demonstrate the exitance of graphene in the nanofibers. Figure 6.2 shows the Raman spectrum of the graphene nanofibers (centrifuged 60 min). There are two peaks approximately 1355 and 1576 cm^{-1} in the graphene nanofibers spectrum, corresponding, respectively, to the D peak associated with edge defects and the G peak associated with the highly ordered graphite. The 2D peak is located at approximately 2725 cm^{-1}. The morphology and thickness of the graphene sheet can be reflected by the intensity and shape of this peak. The high-quality graphene embedded in the nanofibers can be revealed by the symmetrical profile of the peak with respect to the center axis drawn through the peak.

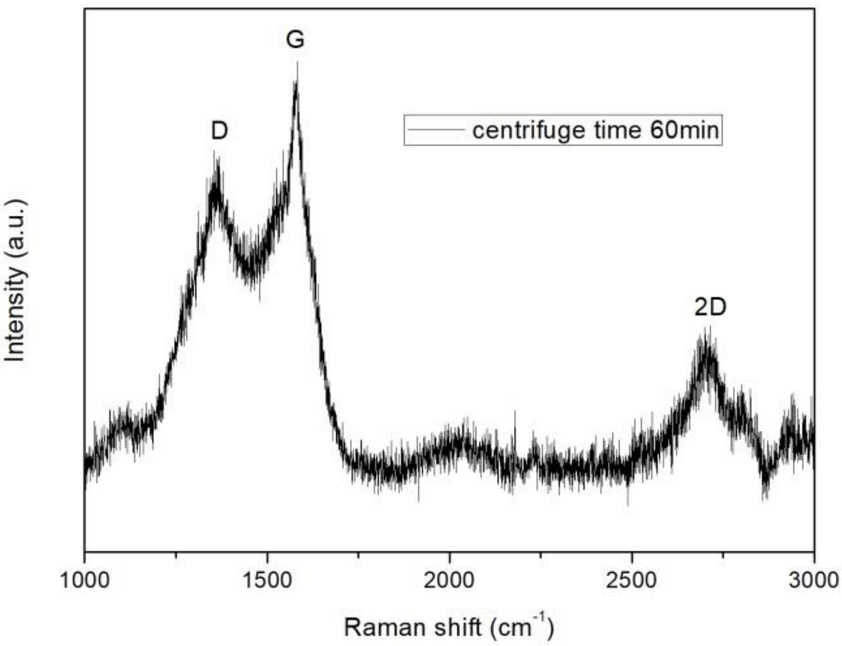

Figure 6.2 Raman spectra of graphene nanofibers.

6.3.2 Photovoltaic performance

The best performance based on current density−voltage (i.e. J−V curves) of the devices for PSC devices, respectively, with and without graphene nanofibers interlayer produced using different centrifugation times is shown in Figure 6.3. We can see that when graphene nanofibers interlayer was used, performance of the device was improved as compared to the device without the interlayer. This is due to the fact that the graphene nanofibers interlayer can improve the charge transport property which can be demonstrated in the IMPS test. The amount and quality of the graphene nanofibers affect the device performance. This is well controlled by the centrifugation time on the precursor solution, with suspended graphene, used for electrospinning. From Figure 6.3, it is evident that the most optimal condition corresponds to the case with centrifugation time of 60 min, for which the maximum PCE reached 18.62% with J_{sc} of 24.35 mA·cm^{-2}, V_{oc} of 1.08 V, and FF of 71%. The parameters corresponding to the best performance for all the conditions are summarized in Table

6.1, while the parameters corresponding to the average performance are tabulated in Table 6.2. Comparing the data in Table 6.1, the device performance parameters, V_{oc}, J_{sc}, FF, and PCE at the optimal condition with graphene nanofibers interlayer (i.e. produced with centrifugation time of 60 min) are all higher than that without the interlayer. Specifically, both J_{sc} and V_{oc} have been improved dramatically due to graphene nanofibers interlayer to facilitate the charge transport across the compact-perovskite layer interface. As a whole, the final PCE has been raised by 5.2% as compared to that of the control device without graphene nanofiber interlayer. The EQE results are shown in Figure 6.4. It is clear that the use of graphene nanofibers interlayer for the PSC devices improve the performance of EQE, at wavelengths between 330 nm and 750 nm.

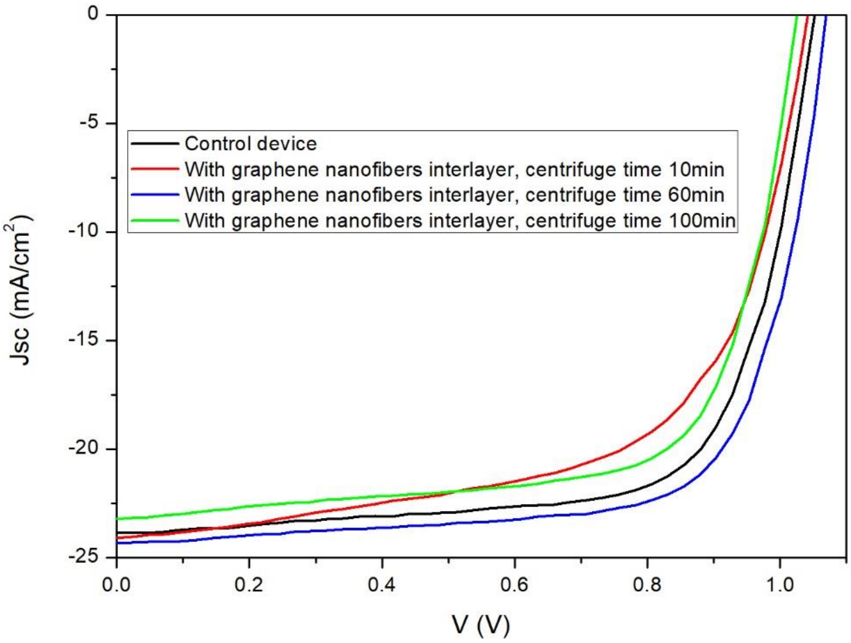

Figure 6.3. J−V curves measured under 100 mW·cm^{-2} AM1.5G illumination.

Table 6.1. Best performance of the Perovskite Solar Cells under AM 1.5 G illumination

	V_{oc} (V)	J_{sc} (mA/cm^2)	FF	PCE (%)
Control device	1.05	23.88	0.71	17.70
Graphene suspension centrifuged 10 min	1.05	24.09	0.61	15.49
Graphene suspension centrifuged 60 min	1.08	24.35	0.71	18.62
Graphene suspension centrifuged 100 min	1.03	23.24	0.70	16.60

Table 6.2. Average performance of the Perovskite Solar Cells

	V_{oc} (V)	J_{sc} (mA/cm^2)	FF(%)	PCE (%)
Control	1.03±0.02	23.20±0.33	69±2	17.20±0.30
Graphene suspension centrifuged 10 min	1.03±0.02	23.62±0.26	59±2	15.00±0.29
Graphene suspension centrifuged 5 min	1.06±0.02	23.93±0.21	69±2	18.02±0.22
Graphene suspension centrifuged 3 min	1.02±0.02	22.96±0.25	68±1	16.12±0.28

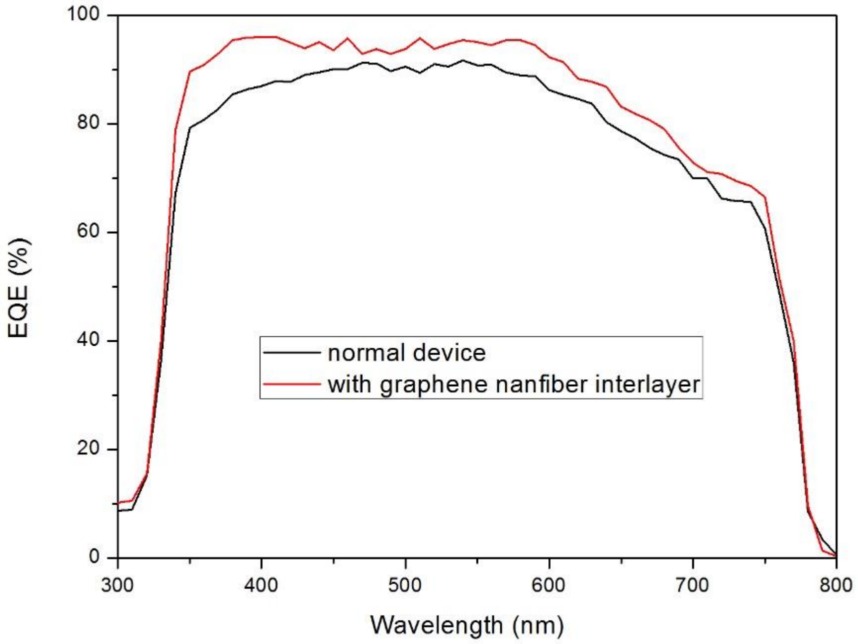

Figure 6.4. External quantum efficiency.

The charge transport time in the solar cells was further investigated by IMPS. The charge transport time of the devices under different centrifugation times have been calculated and the results are tabulated in Table 6.3. Figure 6.5 shows the comparison chart of the transport time and PCE for the devices under different configuration times. Indeed, the charge transport time and PCE are very well correlated. When the charge transport time decreases, PCE increases; and vice versa. The best PCE (18.62%) with the lowest charge transport time (0.8 μs) implies the fastest charge mobility. Based on the foregoing discussion, the nanofibers interlayer provides a dedicated path for photo-generated charges to be transported efficiently from perovskite layer to ETL without getting lost by traps at the interface between the two layers and the charge transport time is reduced as compared to the control without the interlayer. As a result, the transport time for the device with graphene nanofibers interlayer has been shortened by 21% (=1-0.8/1.01) when compared with that of the control device without the graphene nanofiber interlayer.

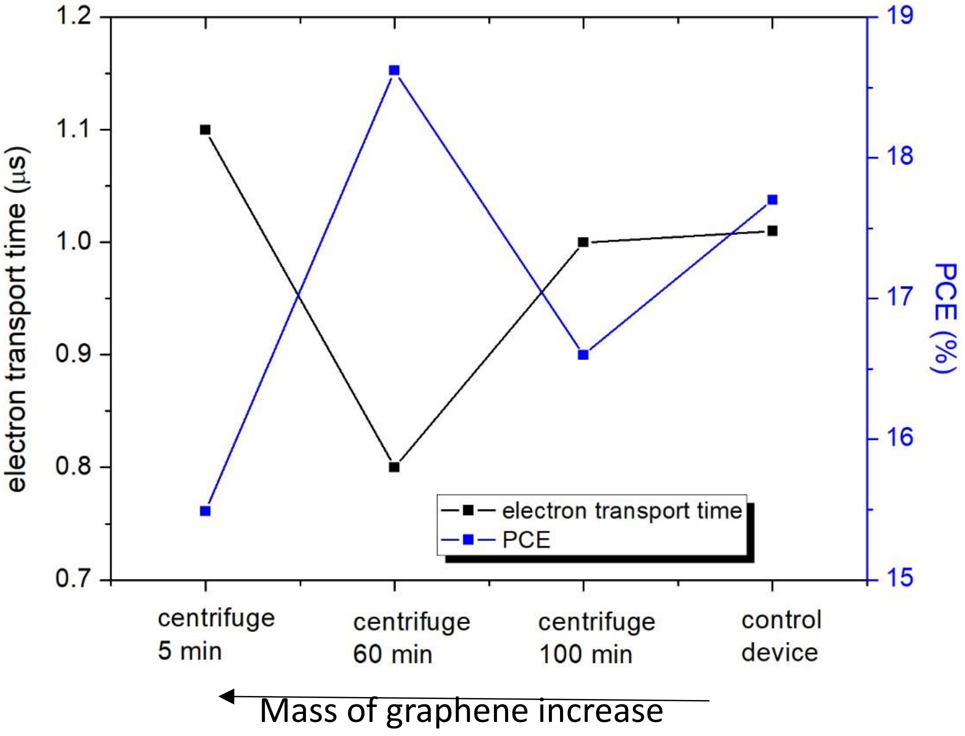

Figure 6.5. Comparison chart of the transport time and PCE for the devices under different conditions

Table 6.3 The electron transport time with respect to the PCE of the devices.

	Carrier transport time (μs)	PCE(%)
Graphene solution centrifuge 100min	1	16.60
Graphene solution centrifuge 60min	0.8	18.62
Graphene solution centrifuge 5min	1.1	15.49
Control device	1.01	17.70

6.4 Conclusions

Applying an ultrathin graphene nanofiber interlayer in between the compact and perovskite layers can facilitate the reduction of interfacial resistance and improve charge transport property of the PSC as a whole. Through control the centrifugation time of the graphene precursor solution can control the quality of the graphene nanofibers which can affect the performance of the devices. This reflects that the size and amount of graphene for the interface is important and given we do not know this apriori without carrying out testing to determine the optimal. After optimization, indeed the optimized PSC showed a higher PCE of 18.62% when compared with 17.7% of control device.

References

1. Feng, S. L., Yang, Y. G., et al. *High-Performance Perovskite Solar Cells Engineered by an Ammonia Modified Graphene Oxide Interfacial Layer*. ACS Appl. Mater. Interfaces, 2016. **8**: p. 14503.

2. Zhou, H. Chen, Q. Li, G. Luo, S. Song, T.-B. Duan, H.-S. Hong, Z. You, J. Liu, Y. Yang, Y. *Interface Engineering of Highly Efficient Perovskite Solar Cells.* Science, 2014. **345**: p. 542.

3. Eperon, G. E., Burlakov, V. M., Docampo, P., Goriely, A., Snaith, H. J. *Morphological Control for High Performance, Solution-Processed Planar Heterojunction Perovskite Solar Cells.* Adv. Funct. Mater. 2014. **24**: p. 151.

4. Wang, Z. K., Li, M., Yuan, D. X., Shi, X. B., Ma, H.; Liao, L. S. *Improved Hole Interfacial Layer for Planar Perovskite Solar Cells with Efficiency Exceeding 15%.* ACS Appl. Mater. Interfaces, 2015. **7**: p. 9645.

5. Min, J., Zhang, Z. G., Hou, Y., Quiroz, C. O. R., Przybilla, T., Bronnbauer, C., Guo, F., Forberich, K., Azimi, H., Ameri, T., Spiecker, E., Li, Y. F., Brabec, C. J. *Interface Engineering of Perovskite Hybrid Solar cells with Solution-Processed Perylene-diimide Heterojunctions Toward High Performance.* Chem. Mater. 2015. **27**: p. 227.

6. Qian, M., Li, M., Shi, X., Ma, H., Wang, Z. K., Liao, L. *Planar Perovskite Solar Cells with 15.75% Power Conversion Efficiency by Cathode and Anode Interfacial Modification.* J. Mater. Chem. A, 2015. **3**: p. 13533.

7. Han, G. S., Song, Y. H., et al. *Reduced Graphene Oxide/Mesoporous TiO2 Nanocomposite Based Perovskite Solar Cells.* ACS Appl. Mater. Interfaces, 2015. **7**: p. 23521.

8. Zhu, Z. L., Ma, J. N., et al. *Efficiency Enhancement of Perovskite Solar Cells through Fast Electron Extraction: The Role of Graphene Quantum Dots.* J. Am.

Chem. Soc. 2014. **136**: p. 3760.

9. Kim, H. S., Lee, J. W., et al. *High Efficiency Solid-State Sensitized Solar Cell-Based on Submicrometer Rutile TiO2 Nanorod and CH3NH3PbI3 Perovskite Sensitizer.* Nano Lett. 2013. **13**: p. 2412.

10. Dharani, S., Mulmudi, H. K., et al. *High efficiency electrospun TiO2 nanofiber based hybrid organic–inorganic perovskite solar cell.* Nanoscale, 2014. **6**: p. 1675.

Chapter 7

Conclusions and Future Outlook

7.1 Conclusions

The organic−inorganic lead halide perovskite solar cells have experienced a dramatic improvement in PCE in recent years. It is clear that film morphology (such as film coverage and grain size) and film quality of perovskite layer are important factors affecting the performance of PSC. In addition, enhancing the electron transport property is also a vital factor for improving the efficiency of the perovskite solar cells. In this thesis, a series of optimized and controllable fabrication techniques for obtaining high-performance devices were systematically studied.

First, an efficient, low-cost method to fabricate a uniform and dense perovskite layer with large crystal size has been demonstrated by applying DMSO via an intercalation process to increase the crystal size and introducing HCl as an additive to slow-down the crystal growth rate to get more uniform crystals. Concurrently, the crystallinity of the perovskite layer and the charge transport property of the device can be also enhanced. A high efficiency of 17.8% has been achieved by the device with both the DMSO and HCl synergistic treatment. Furthermore, 11% and 17% improvements have been realized with combined DMSO and HCl treatments when compared with the devices with application of only DMSO and only HCl, respectively. Also, the stability of the device from high humidity, high solar irradiation, and high temperature due to HCl treatment has been improved compared with just DMSO treatment.

Second, a method for incorporating graphene nanofibers in the perovskite layer of the perovskite solar cell has been successfully demonstrated. The quality of the graphene nanofibers was optimized by controlling the centrifugation time at high centrifugal acceleration on the precursor suspension for electrospinning nanofibers. We found that the optimal conditions corresponded to a precursor suspension that had been centrifuged for 20 min prior to electrospinning into graphene nanofibers, which were subsequently added to the perovskite layer. Under the optimized conditions, the device PCE increased from 17.51% without graphene nanofibers in the perovskite layer to 19.83% with graphene nanofibers in the perovskite layer. Firstly, the introduction of graphene nanofibers led to rapid nucleation and reformation of smaller crystals into much larger crystals of over 2 μm. These large crystals have fewer grain boundaries and better crystallinity, which results in much higher FF and J_{sc} values. Secondly, the much higher J_{sc} and V_{oc} values can be attributed to the improvement in charge-transport properties on incorporating graphene nanofibers into the perovskite layer. The electron transport time for the graphene nanofiber containing PSC was nearly half of that of the PSC device without graphene nanofibers. The stability of the device was also improved.

Third, an approach for engineering large, uniform perovskite crystals by crystallizing in well-defined structured pores from pre-fabricated thin TiO_2 nanofiber scaffold has been presented. The TiO_2 nanofibers in the scaffold are further embedded with graphene for use in the perovskite solar cell to improve charge conductivity. The concentration of the graphene in nanofibers has been optimized by controlling the centrifugation time at high centrifugal acceleration on the precursor suspension containing graphene. The most optimal condition corresponds to the graphene precursor suspension that has been centrifuged for 5 min, which subsequently is used for preparing the TiO_2/embedded graphene precursor solution for electrospinning. Under this optimal condition, the device PCE increased from 17.46% without the scaffold to 19.30% with TG nanofibers scaffold, representing a 11% increase. First, due to the structured nanofibers scaffold, a more uniform and smoother perovskite layer with large grain sizes can be formed, which has excellent crystallinity and light harvesting characteristics. In addition, the unreacted PbI_2, which provides the recombination sites, is reduced. This leads to higher FF and better light harvesting.

Second, the much higher J_{sc} and V_{oc} can be attributed to the improved charge transport property by using graphene embedded in the TiO_2 nanofibers scaffold for the devices. The electron transport time for the device with TG nanofibers scaffold is nearly half of that of the devices without the scaffold layer. The stability of the devices with TG nanofibers scaffold has also been improved.

Fourth, we have demonstrated an ultrathin graphene nanofiber interlayer between the perovskite and the dense layers can reduce the interfacial resistance and improve charge transport property of the PSC. By controlling the centrifugation time of the graphene precursor solution we can control the quality of the graphene nanofibers which can affect the performance of the devices. The optimized PSC showed a higher PCE of 18.62% when compared to the control device with only 17.7%.

7.2 Future Outlook

Different approaches have been studied individually to improve the performance of the devices in different chapters. In future we need to study whether combine these methods can further improve the performance for the devices. We think this can help to improve the performance, but how this can affect the morphology of the perovskite layer and the charge transport property need to be further studied.

In this thesis we used TiO_2 as the ETL. As known, Tin dioxide (SnO_2) is a promising alternative to TiO_2 due to its wider band gap, higher electron mobility (which is two orders of magnitude higher than that of TiO_2 [1]), and low conduction band efective mass [2]. As discussed before, a major loss in PCE of PSCs is caused by a rapid degradation in the performance of TiO_2-based devices which is due to the exposure to UV light [3]. SnO_2 has a wider band-gap which absorbs less UV light and is thus more robust under sunlight than TiO_2 [4]. In future study, one can attempt to fabricate SnO_2 nanofibers as the scaffold layer to see whether this can have a better performance than use of TiO_2. Further, one can also try to embed graphene into the scaffold layer to optimize the performance.

Second, in the literature RGO, GO or CNT have been added into the HTL or as a interlayer between the perovskite layer and HTL [5-7] to improve the hole extraction, reduce the recombination rate of the device, and improve the stability of the device. As we have discussed before, RGO, GO or CNT have lower conductivity and more defects than pristine graphene. In the next step, one can also attempt to use graphene nanofibers to combine into the HTL or as the interlayer. The results can be compared with those obtained using RGO, GO or CNT to determine possible improvement in the performance of the PSC.

As known, under excessive exposure lead can damage the nervous system and cause brain disorder and even death. Therefore, it is essential to explore other nontoxic metal to replace lead to fabricate lead-free or less-lead PSC. There are various works that have shown promises in the lead-free PSCs [8-10]. In future study, one can try to use similar approaches as mentioned before to improve crystals size by conditioning, graphene NF introduced in perovskite layer and preformed porous structure of scaffold in molding crystals of uniform size. This should improve light harvest reducing unreacted inorganics. Additionally, graphene nanofibers or TiO_2 nanofibers embedded with graphene core can be used in new lead-free, or less-lead, perovskite to improve charge transport.

In summary, there is still lots of room for improving the efficiency and stability for the PSC. For future work, one can combine the techniques as developed in our study in combination with more effective new techniques to optimize the PSC device performance.

7.3 References

1. Wali, Q., Fakharuddin, A., Jose, R. *Tin oxide as a photoanode for dye-sensitised solar cells: Current progress and future challenges.* J. Power Sources, 2015. **293**: p. 1039.

2. Wali, Q., Fakharuddin, A., et al. *Multiporous nanofibers of SnO2 by electrospinning for high efficiency dye-sensitized solar cells.* Journal of Materials Chemistry A, 2014. **2**: p. 17427.

3. Leijtens, T., Eperon, G. E., et al. *Overcoming ultraviolet light instability of sensitized TiO2 with meso-superstructured organometal tri-halide perovskite solar cells.* Nat. Commun. 2013. **4**: p. 2885.

4. Tiwana, P., Docampo, P., et al. *Electron mobility and injection dynamics in mesoporous ZnO, SnO_2, and TiO_2 films used in dye-sensitized solar cells.* ACS Nano, 2011. **5**: p. 5158.

5. Cao, J., Liu, Y. M., et al. *Well-Defined Thiolated Nanographene as Hole-Transporting Material for Efficient and Stable Perovskite Solar Cells.* J. Am. Chem. Soc. 2015. **137**: p. 10914.

6. Li, W., Dong, H., et al. *Graphene oxide as dual functional interface modifier for improving wettability and retarding recombination in hybrid perovskite solar cells.* J. Mater. Chem. A, 2014. **2**: p. 20105.

7. Luo, Q., Zhang Y., et al. *Iodide-reduced graphene oxide with dopant-free spiro-OMeTAD for ambient stable and high-efficiency perovskite solar cells.* J. Mater. Chem. A, 2015. **3**: p. 15996.

8. Xiao, Z., Meng, W., et al. *Searching for promising new perovskite-based photovoltaic absorbers: the importance of electronic dimensionality. Mater.* Horiz. 2017. **4**: p. 206.

9. Zhao, Z., Gu, F., et al. *Mixed‐Organic‐Cation Tin Iodide for Lead‐Free*

Perovskite Solar Cells with an Efficiency of 8.12%. Adv. Sci. 2017. **4**: p. 1700204.

10. Boopathi, K. M., Karuppuswamy, P., et al. *Solution-processable antimony-based light-absorbing materials beyond lead halide perovskites.* J. Mater. Chem. A. 2017. **5**: p. 20843.